

# On a quest to discover where stellar-mass Black Holes merge

- Testing the AGN binary formation channel with spatial  
correlation analyses -

Proefschrift

Niccolò Veronesi

geboren te Bentivoglio, BO, Italy  
in 1995

Promotores:

Prof. dr. E. M. Rossi

Prof.dr. K. H. Kuijken

Promotiecommissie:

ISBN:

Cover:

Printed by:

"de' remi facemmo ali al folle volo"  
– *Comedia*, Dante Alighieri (1321)

# CONTENTS

<b>1</b>	<b>Introduction</b>	<b>1</b>
1.1	Black Holes: from mathematical concepts to astrophysical objects	1
1.2	Not only light: Binary Black Holes and Gravitational Waves . . . . .	3
1.3	Formation of Binary Black Holes: isolated binaries and dynamically active environments . . . . .	7
1.4	AGN discs as promising potential hosts of stellar-mass Binary Black Hole mergers . . . . .	10
1.4.1	Disc captures . . . . .	12
1.4.2	Migration . . . . .	12
1.4.3	Characteristic observable signatures of BBHs merging in AGN discs . . . . .	14
1.4.3.1	Non-null eccentricity in the LVK band . . . . .	14
1.4.3.2	Anti-correlation between mass ratio and effective spin parameter . . . . .	15
1.5	The potential and the challenges of detecting EM counterparts of GW events . . . . .	16
1.5.1	Spatial correlation analyses with all-sky AGN catalogues . . . . .	18
1.5.1.1	Milliquas . . . . .	19
1.5.1.2	Quaia . . . . .	19
1.5.2	Spatial correlation analyses with unusual AGN flaring activities . . . . .	21
1.6	In this thesis . . . . .	23
1.7	Future outlook . . . . .	25
<b>2</b>	<b>Detectability of a spatial correlation between stellar-mass black hole mergers and Active Galactic Nuclei in the Local Universe</b>	<b>29</b>
2.1	Introduction . . . . .	30
2.2	Method . . . . .	32
2.2.1	Simulation of GW detections . . . . .	33
2.2.1.1	Source population . . . . .	33
2.2.1.2	The network of detectors . . . . .	33
2.2.1.3	Evaluation of 90% CL localization volumes . . . . .	34
2.2.2	Minimum number of GW detections to test the AGN origin	36
2.3	Results . . . . .	38
2.3.1	Minimum number of GW detections with fixed $n_{\text{AGN}}$ . . . . .	38

2.3.2	Significance of the no-connection hypothesis rejection as a function of $n_{\text{AGN}}$ and $f_{\text{agn}}$ . . . . .	38
2.4	Discussion and conclusion . . . . .	40
<b>3</b>	<b>The most luminous AGN do not produce the majority of the detected stellar-mass black hole binary mergers in the local Universe</b>	<b>45</b>
3.1	Introduction . . . . .	45
3.2	Datasets . . . . .	48
3.2.1	AGN catalogues . . . . .	48
3.2.2	Detected Gravitational Wave events . . . . .	52
3.2.3	AGN mock catalogue . . . . .	55
3.2.4	Simulated Gravitational Wave sky maps . . . . .	55
3.3	Method . . . . .	57
3.3.1	Likelihood function . . . . .	57
3.3.2	Test on mock data . . . . .	59
3.3.3	Application to real data . . . . .	60
3.4	Results . . . . .	62
3.5	Discussion and conclusion . . . . .	65
<b>4</b>	<b>AGN flares as counterparts to the mergers detected by LIGO and Virgo: a novel spatial correlation analysis</b>	<b>71</b>
4.1	Introduction . . . . .	72
4.2	Datasets . . . . .	74
4.2.1	AGN flares . . . . .	74
4.2.2	GW events . . . . .	75
4.2.3	Matching events . . . . .	78
4.3	Method . . . . .	79
4.4	Results . . . . .	82
4.4.1	Posterior distributions . . . . .	83
4.4.2	Background Monte Carlo realisations . . . . .	84
4.4.3	Binary Mass distributions . . . . .	86
4.5	Discussion and conclusion . . . . .	88
<b>5</b>	<b>Constraints on the AGN channel for the formation of stellar- mass Binary Black Holes up to <math>z=1.5</math> using the Quaia catalogue</b>	<b>95</b>
5.1	Introduction . . . . .	96
5.2	Datasets . . . . .	99
5.2.1	GW events . . . . .	99

5.2.2	Quaia AGN catalogue . . . . .	100
5.2.3	Completeness estimation . . . . .	103
5.2.3.1	Evaluation of bolometric luminosity from $\text{mag}_{\text{GRP, VEG}}$ . . . . .	103
5.2.3.2	Comparison with the bolometric luminosity estimates of Wu & Shen (2022) . . . . .	104
5.2.3.3	Comparison with the AGN luminosity function of Kulkarni et al. (2019) . . . . .	106
5.3	Method . . . . .	108
5.4	Results . . . . .	111
5.5	Discussion and conclusion . . . . .	114
<b>Nederlandse samenvatting</b>		<b>129</b>
<b>Summary</b>		<b>131</b>
<b>Publications</b>		<b>133</b>
<b>Curriculum Vitae</b>		<b>135</b>
<b>Acknowledgements</b>		<b>137</b>



# 1 | INTRODUCTION

Since humanity has become able to directly detect Gravitational Waves, it has unlocked the possibility of understanding the Cosmos in a different, more complete way. Some of the events that generate these propagating perturbations of the structure of the Universe itself are in general not expected to directly emit any light, and are therefore invisible to every telescope or radio-interferometer. One example of this are stellar-mass Black Hole Binary mergers. More than one hundred of such events have been directly detected in the last ten years. However, their physical origin remains elusive. Multiple scenarios have been proposed for the formation of these binary systems, but which one of those is the dominant one, if a dominant one exists at all, is still debated. In this chapter I review the main astrophysical aspects of Black Hole Binaries, highlighting the potential that the direct detection of their mergers has to push forward our understanding regarding the evolutionary stages of stars, the central regions of galaxies, and the expansion of the Universe. I discuss the open questions regarding these binary systems, the challenges in their detection, and the possible ways we have to understand their origin.

## 1.1 Black Holes: from mathematical concepts to astrophysical objects

There are not many objects in the Universe that are able to inspire the curiosity of astronomers and the general public like Black Holes (BHs). From the mathematical point of view, these compact objects are solutions of Einstein's field equations of General Relativity ([Einstein 1915](#)). These equations link the distribution of mass and energy of an object to the shape of the spacetime curvature it generates, hence to the nature of the gravitational interaction between such an object and the rest of the Universe. In particular, a BH is defined as a region of spacetime causally separated from the rest of the Universe. Physical objects can enter this region, but is then impossible for them to influence anything that is outside of it. The surface that delimits the boundary of a BH is called Event Horizon.

The fact that BHs represent exact solutions of Einstein's field equations was first demonstrated in the case of a spherically symmetric static source ([Schwarzschild 1916](#)), then in the case of a rotating axially symmetric one,

either electrically uncharged (Kerr 1963), or charged (Newman et al. 1965). However, it is only since the second half of the 1960s that BHs have been considered as astrophysical objects, and not just as mathematical concepts. The real existence of these extremely compact objects was suggested by the first observations of Quasistellar radio sources (Quasars), which emitted an amount of energy thought to be explainable only by the collapse of an object with a mass of the order of millions of Solar Masses ( $M_\odot$ ) (Robinson et al. 1965). The theoretical confirmation of the fact that BHs could be astrophysical objects actually existing in the Universe came from results such as the one presented in Penrose (1965), where it was demonstrated that the gravitational collapse of a massive astrophysical object can indeed lead to the formation of a point-like singularity enclosed in an Event Horizon.

The first astrophysical object ever to be widely accepted to be a BH has been the galactic X-ray source Cygnus X-1, first observed in 1965 (Bowyer et al. 1965), and later confirmed to be a BH accreting mass from a blue supergiant star (Shipman 1975). The accretion process involves the conversion of the gravitational potential energy of material infalling onto a BH into thermal energy and luminosity, energy emitted in the form of ElectroMagnetic (EM) waves. In the last 50 years, millions of accreting BHs have been detected. These objects can be divided into two main categories: stellar-mass BHs, and Super-Massive BHs (SMBHs). Stellar-mass BHs detected through EM waves have masses between approximately  $3M_\odot$  and  $20M_\odot$ , and are the remnants of SuperNovae (SNe) events that marked the end of the core-burning phase of massive stars. The other category of detected BHs is characterised by masses between  $10^6M_\odot$  and  $10^9M_\odot$ . These SMBHs can be found at the centre of galaxies and are the ones that power Active Galactic Nuclei (AGN). An AGN is a system formed by a central SMBH located at the centre of a gaseous disc, the material of which falls onto the compact object, causing the emission of a large amount of energy spread over a wide portion of the EM spectrum, from radio waves to gamma rays. The luminosity of an AGN usually out-shines the starlight emitted by the entirety of its host galaxy.

Measuring light coming from accretion is not the only way to use EM radiation to detect a BH. The position and the mass of compact objects can be calculated via the observations of microlensing events, when the path of the light coming from an object is perturbed by the passing of a BH between such object and the observer (Paczynski 1986, 1996). Another indirect way to infer the properties of a BH is by resolving the orbits of objects such as stars that are bound to it. This method has been used in the past to estimate the position and the mass of the SMBH that resides at the centre of the Milky Way (Schödel

et al. 2002; Ghez et al. 2008) and of three stellar-mass BHs in its halo (El-Badry et al. 2023a,b; Gaia Collaboration et al. 2024).

## 1.2 Not only light: Binary Black Holes and Gravitational Waves

One of the biggest conceptual differences between Einstein’s General Relativity and Isaac Newton’s theory of gravitation (Newton 1687) is that, according to the former, the gravitational interaction between two objects travels at the same finite speed at which EM radiation travels in vacuum. In particular, when the mass distribution acting as source of spacetime curvature has a time-varying quadrupolar moment, it emits Gravitational Waves (GWs), which move from their source at the speed of light. A common way of conceptually and mathematically visualizing GWs is as travelling ripples, perturbations in the curvature of spacetime, the amplitude and the frequency of which depend on the characteristics of their originator.

Among the events that can emit detectable GWs there are the inspirals and mergers of binaries of compact objects. These waves can be detected by measuring the periodic variation of the proper distance between objects their passage cause. The relative amplitude of such variations is typically of the order of less than  $10^{-20}$ , and it decreases linearly as a function of the distance from the source. However, the direct measurement of GWs coming from the merging binaries formed by stellar-mass BHs and/or Neutron Stars (NSs) has become a reality thanks to the laser interferometers of the LIGO-Virgo-KAGRA (LVK) collaboration (Acernese et al. 2015; LIGO Scientific Collaboration et al. 2015; Kagra Collaboration et al. 2019).

Almost ten year have passed since the first direct detection of GWs (Abbott et al. 2016), and since then three observing runs have been completed, while the fourth one is expected to last until June 9th, 2025. During the first three observing runs (O1, O2, and O3) a total of 90 mergers have been detected, most of them being of Binary Black Holes (BBHs) (Abbott et al. 2023a, 2024). Figure 1.1 gives a visual representation of all these detected mergers in chronological order from left to right. On the vertical axis is the mass of the merging objects and of the remnant. Light blue dots represent BHs, orange ones represent NSs, and objects of which the nature is uncertain are represented by half blue-half orange dots.

Merging BBHs are in general not expected to produce any EM radiation.

## 1.2. NOT ONLY LIGHT: BINARY BLACK HOLES AND GRAVITATIONAL WAVES

---

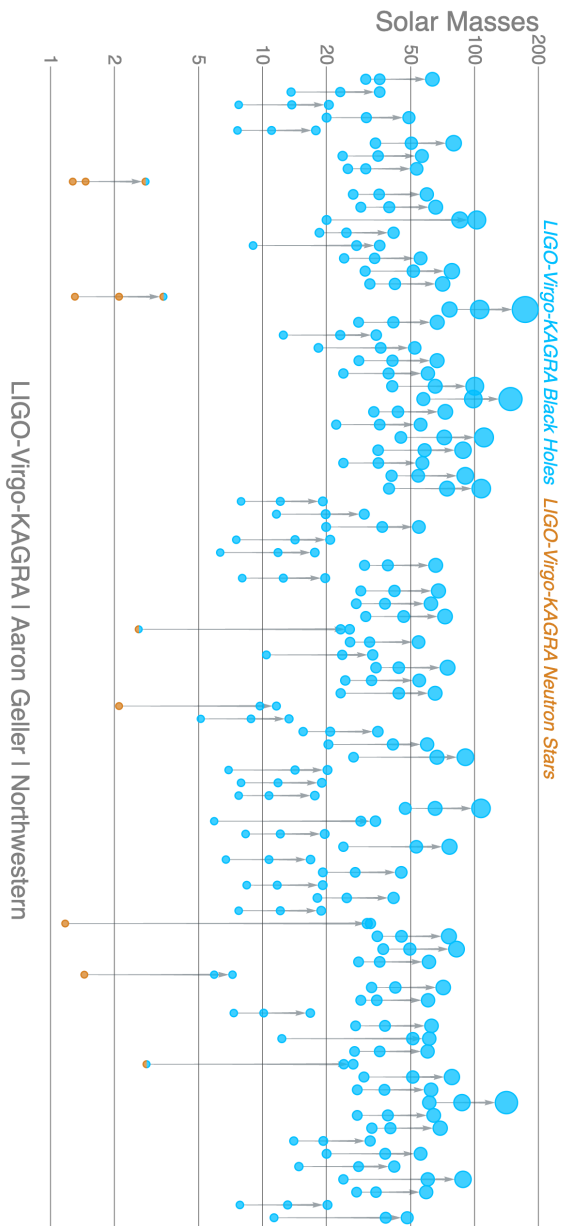


**Figure 1.1:** Visual representation of the 90 binary mergers detected by the interferometers of the LVK collaboration during their first three observing runs. The vertical axis indicates the rest-frame masses. In each group of three dots connected by an arrow, the bottom two represent the merging objects, while the top one represents the remnant. The mergers are chronologically ordered, from left to right. Light blue (orange) dots represent BHs (NSs). Objects the nature of which is uncertain are represented by symbols of both colors.

Detecting the GWs they emit is therefore the only way to learn about them. The intrinsic properties of each binary that are possible to constrain with GW detections include the masses of the two components, and both the amplitude and the direction of their spins. By combining the information coming from all the single detections it is possible to draw conclusion regarding the underlying astrophysical population of compact objects.

Figure 1.2, taken from [The LIGO Scientific Collaboration et al. \(2021\)](#), shows the astrophysical mass spectrum for stellar-mass BHs inferred from the detections of the LVK collaboration. The differential merger rate is plotted as a function of the mass of the heavier component of the merging binaries  $m_1$ . While the black solid and dashed lines show the results obtained from all the events up to the first half of O3, the blue solid line and the light blue shaded region show the median and the 90 per cent credible interval of the posterior distribution inferred from all the events detected during the first three observing runs. The analytical model used for the fit consists of a truncated power-law, with a tapering at low masses and a Gaussian component. The vertical gray band in Figure 1.2 shows the 90 per cent credible interval on the position of the mean of such Gaussian component.

One conclusion of population analyses on BBHs that remains robust with respect to the analytical model that is assumed during the fit, is the fact that the mass spectrum of stellar-mass BHs extends to masses above  $50M_{\odot}$  ([The LIGO Scientific Collaboration et al. 2021](#)). Objects with such masses were not present in the population inferred from observations of X-ray binaries, and their existence is not predicted by most of the models of stellar evolution ([Heger & Woosley 2002](#); [Belczynski et al. 2016](#)). The presence of a gap between  $50M_{\odot}$  and  $120M_{\odot}$  in the mass distribution of the remnant of SuperNovae (SNe) events is expected because of the phenomenon of Pair Instability SuperNovae (PISNe) ([Woosley 2019](#)). These events represent the end of the life cycle of stars with an initial mass greater than approximately  $150M_{\odot}$ , and consist of SNe where electron-positron pairs are created during the collapse of the stellar structure ([Heger et al. 2003](#)). The resulting runaway thermonuclear explosion is expected to leave no remnant ([Fraley 1967](#)).

Observational evidence obtained thanks to the direct detection of GWs, such as the lack of a gap in the BH mass spectrum between  $50M_{\odot}$  and  $120M_{\odot}$ , suggests the existence of BBH formation paths beyond the standard scenario of the evolution of an isolated binary stellar system. This remains valid even when taking into account that the position of the lower boundary of the so-called Pair Instability mass gap depends on the stellar model that is assumed, and on stellar properties such as the metallicity ([Farag et al. 2022](#)).

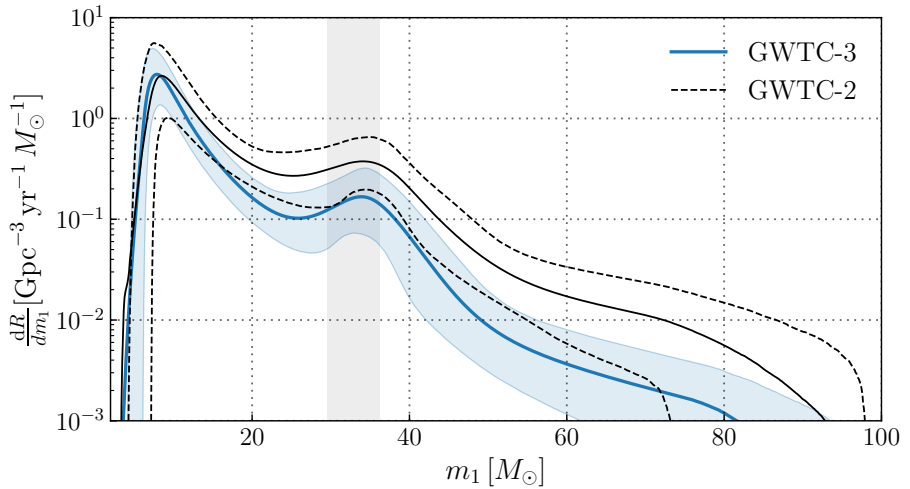


**Figure 1.2:** Differential merger rate as a function of the mass of the heavier component of BBHs. This astrophysical distribution of stellar-mass BH masses is the result of population analyses based on the GW detections performed by the LVK interferometers up to the first half of their third observing run (black solid and dashed lines), and including also the ones of the second half (blue line and shaded region). Solid lines indicate the median posterior distribution, and the shaded region and the dashed black lines indicate its 90 per cent credible interval. The models used for the fit is based on a truncated power law, with a tapering function at low masses, and a Gaussian component. The 90 per cent credible interval on the position of the mean of this Gaussian component is denoted by the vertical gray shaded region. The plot is taken from [The LIGO Scientific Collaboration et al. \(2021\)](#)

## 1.3 Formation of Binary Black Holes: isolated binaries and dynamically active environments

The physical origin of the binaries of which the mergers have been detected through GWs by the LVK collaboration remains elusive. In order for a binary of stellar-mass compact objects to emit energy in the form of GW radiation efficiently enough to be driven to merger within a Hubble time, its semi-major axis has to be of the order of  $10^{-1}$  Astronomical Units (Mapelli 2021). Different formation paths for BBH that tight have been proposed, and they can be divided into two main categories: formation through the evolution of an isolated binary system of massive stars, and formation in dynamically dense environments, where encounters between stellar-mass objects are frequent (see Mapelli 2021, for a review of the possible binary formation paths).

In the case of a massive isolated stellar binary system a tight binary of compact objects can form after a Common Envelope (CE) phase (Ivanova et al. 2020). This occurs when one of the two stars incorporates the remnant of the other one within its own envelope, when entering the giant phase. If the CE is efficiently expelled because of the friction caused by the orbital motion of the two cores, the remaining binary can be tight enough to merge within a Hubble time and to be detected by the interferometers of the LVK collaboration. A schematic representation of the formation of a merging BBH through the CE channel is shown in Figure 1.3.

Another way for an isolated stellar binary system to create a BBH capable of merging within a Hubble time is through chemically homogeneous evolution (de Mink & Mandel 2016; Mandel & de Mink 2016). If a massive star is rotating fast and has a low metallicity, it might not develop a gradient of chemical composition in its interior. These chemically homogeneous stars have smaller radii compared to the slow rotating ones with the same mass, and can therefore form very tight binaries of compact objects without ever entering the CE phase (Marchant et al. 2016).

Alongside the evolution of isolated massive stellar binary systems, BBHs tight enough to be able to merge within a Hubble time can also form in dynamically active environments. A host environment is here referred to as "dynamically active" or "dynamically dense" if it has a density of approximately a thousand or more stellar-mass objects per cubic parsec. In such conditions, single objects or binary systems are expected to have strong gravitational interactions, that can lead to the formation of hard binaries. A binary is referred to as "hard" if its binding energy is larger than the average kinetic energy of

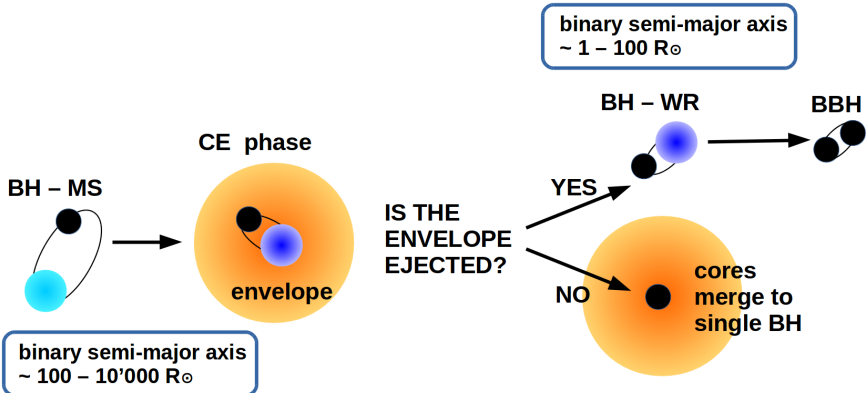


**Figure 1.3:** Representation of the formation of a merging BBH through the CE channel (taken from Mapelli (2021)). On the left it is shown a system formed by a star in the main sequence (light blue circle) and a BH, remnant of a SN event. When the star exits the main sequence and starts burning Helium in its core (blue circle), entering the giant phase, its envelope incorporates the BH. The binary system formed by the Helium-burning core and the BH gets tighter because of the drag exerted by the gas the envelope consists of. Part of the loss of orbital energy is turned into heat, which might cause the ejection of the envelope. If this happens, what is left is a tight binary formed by a BH and a naked stellar core, a Wolf-Rayet (WR) star. If the WR turns into a BH without disrupting the binary, the BBH that forms can be tight enough to emit detectable GWs efficiently and merge within a Hubble time. If the CE is not ejected, the Helium burning core and the BH merge inside of it, and no detectable GW is emitted.

the objects that are in its surroundings (Heggie 1973). Examples of dynamically dense environments are Globular Clusters (Gratton et al. 2019), Young Star Clusters (Lada & Lada 2003; Portegies Zwart et al. 2010), Nuclear Star Clusters (Ferrarese et al. 2006; Neumayer et al. 2020), and AGN accretion discs (McKernan et al. 2011; Stone et al. 2017).

In dense environments dynamical friction slows down objects on timescales inversely proportional to their mass (Chandrasekhar 1943). The more efficiently a massive object is slowed down the interaction with lighter ones surrounding it, the more quickly it sinks towards the gravitational centre of the host environment. This process leads to mass segregation, building up a population of heavy stellar-mass BHs and BBHs clustered in the inner regions of dense star clusters.

Beside dynamical friction, another class of gravitational interaction that is important to mention when talking about the formation of merging BBHs in dense environments is single-binary encounters. These processes involve a binary system of stellar-mass objects, and a single third object that can also be either a star or a compact object like a BH or a Neutron Star (NS). The encounter happens if the single object approaches the binary, reaching a distance from it comparable with its semi-major axis. The final product of this interaction is a binary which is in general harder than the original one, and that is formed by the two most massive objects that took part in the interaction. This is because if the intruder has a mass higher than at least one component of the original binary, than it has a probability close to one to take its place as part of the bound system, while the least massive object is ejected (Hills & Fullerton 1980). Hardening of binaries in these types of interactions takes place when part of the binary binding energy is transformed into kinetic energy of the ejected object.

Both dynamical friction and single-binary encounters happening in dynamically active environments are processes that can efficiently create binary systems composed by the heaviest objects that populate such environments (Ziosi et al. 2014). However, these processes cannot create binaries with BHs more massive than the ones that are already present in the initial population. They are therefore not sufficient to explain the observed evidences of merging BBHs with components that populate the Pair Instability gap in the stellar-mass BH spectrum.

One way of creating BHs with masses in the Pair Instability mass gap is through subsequent mergers, where at least one component of the merging binary is the remnant of a previous GW event. This hierarchical merger scenario is theoretically capable of creating objects with masses up to the Intermediate

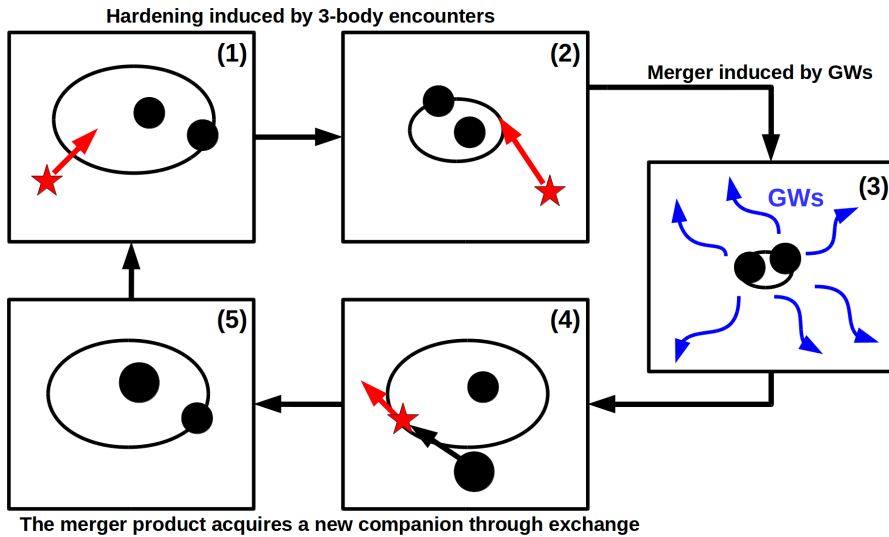
Mass BH (IMBH) regime (between  $10^3 M_\odot$  and  $10^6 M_\odot$ ) ([Antonini et al. 2019](#); [Mahapatra et al. 2024](#)). However, in order for a remnant to have a non negligible chance to take part to a higher-generation event, it must be retained in the same environment that hosted the first merger, which is a reservoir of compact objects that can potentially act as components for the second one. When two compact objects merge the remnant undergoes the action of a recoil kick to guarantee the conservation of the total linear momentum of the binary system ([Bonnor & Rotenberg 1961](#); [Bekenstein 1973](#)). Typical recoil kick velocities for the remnants of BBH mergers are of the order of  $10^2 \text{ km s}^{-1}$ , but can reach values of thousands of kilometers per second for specific combinations of masses and spins of the binary components ([Campanelli et al. 2007](#); [Gerosa & Berti 2019](#)). The hierarchical merger scenario, therefore, can only be efficient in very dense environments, whose escape velocity is large enough for most of the merger remnants to be retained. This is, for example, the case for Nuclear Star Clusters ([Antonini & Rasio 2016](#); [Mapelli et al. 2021](#)).

Figure 1.4 shows a schematic representation of the interactions that are expected to take place in dynamically dense environments, resulting in the emission of detectable GWs.

Being the places in which processes like dynamical friction, single-binary encounters, and hierarchical mergers happen, dynamically dense environments have the potential of being the hosts of a significant fraction of the GW events detected so far by the LVK collaboration. More specifically this so-called "dynamical formation path" for merging BBHs is expected to be the channel that the most massive merging binaries more likely have followed, especially the ones with at least one component that has a mass in the Pair Instability gap predicted by stellar evolution models.

## 1.4 AGN discs as promising potential hosts of stellar-mass Binary Black Hole mergers

The two main characteristics that make AGN accretion discs different with respect to the other dynamically dense environments like Globular Clusters, Young Star Clusters, and Nuclear Star Clusters are their non-spherical shape, and that they are made of gas which interacts with the compact objects contained in the disc itself, modifying their orbits in a non-negligible way.



**Figure 1.4:** Schematic representation of the main processes that can take place in dynamically dense environments, concerning BBHs that merge emitting detectable GWs (taken from [Mapelli \(2021\)](#)). (1) A single stellar-mass object (red star) encounters a BBH both the components of which are more massive than the stellar-mass object itself. (2) The single-binary encounter hardens the bound system, reducing the size of its semi-major axis. (3) If the binary is tight enough, it starts to emit GWs efficiently. Such emission continues until the binary merges. This merger can be detected by the LVK interferometers. (4) The massive BH which is the remnant of the GW event gets retained in the host environment and encounters a binary system. The least massive of the three objects (red star) gets ejected and an exchange episode happens, in which the massive remnant takes its place in the binary system. (5) A new binary is formed, which can be hardened by a new single-binary encounter, and potentially merge in a higher-generation GW event.

### 1.4.1 Disc captures

The moment in which a gaseous accretion disc forms around the SMBH which is at the centre of a galaxy marks the beginning of the AGN phase of such Nuclear Star Cluster. Stars and stellar-mass compact objects whose orbit around the central SMBH lies on the same plane of the newly-formed disc will start to interact dynamically with it. However, AGN accretion discs with a density larger than  $10^{-10} \text{ g cm}^{-3}$ , can capture objects that have a moderate ( $< 15^\circ$ ) initial orbital inclination with respect to the disc. These captures happen on timescales of the order of  $10^6 \text{ yr}$  (Fabj et al. 2020) and are possible because of the exchange of energy and angular momentum between the disc and the orbiter, which takes place every time the latter passes through the former (Ostriker 1983; Syer et al. 1991).

Disc captures have been found to be more efficient in the case of retrograde orbiters (i.e. stellar-mass objects with orbits the angular momentum of which has an inclination with respect to the one of the disc larger than  $90^\circ$ ) (Nasim et al. 2023). In the cases in which the disc capture mechanism turns out to be efficient, its final outcome is a increase in the density of stars and stellar-mass compact object in the accretion disc. In particular, this density is larger than the three-dimensional density the same objects would have in a spherical Nuclear Star Cluster without an AGN.

### 1.4.2 Migration

A compact object embedded in a gaseous disc interacts with it, suffering a net torque and exchanging energy and angular momentum (Armitage 2010; Paardekooper et al. 2010). This phenomenon takes place in systems of different scales, from protoplanetary discs to AGN accretion ones, and modifies the semi-major axis of the orbit of the interacting satellite around the central object, which consists of a protostar in the protoplanetary scenario or of a SMBH in the AGN one. This variation of semi-major axis is called Type I migration when the mass ratio between the satellite object and the central one is of the order of  $10^{-5}$  or smaller. This is the case of systems composed of a stellar-mass BH ( $10^0 - 10^2 M_\odot$ ) orbiting around a SMBH ( $10^6 - 10^9 M_\odot$ ) located at the centre of an AGN. In regime with a low turbulence level, Type I migration happens on a time-scale which is inversely proportional to the mass of the satellite objects, meaning that the heaviest stellar-mass BHs embedded in an AGN disc are the ones whose orbits change more rapidly due to the interaction with the gas (McKernan et al. 2011).

While in general the migration of a stellar-mass compact object is expected to proceed inwards (Goldreich & Tremaine 1979), under the assumption of an adiabatic midplane of the disc, it can proceed outwards for specific ranges of radial distance between the orbiter and the central object (Paardekooper & Mellema 2006). On the border between a region in which migration is expected to proceed inwards, and a region in which it is expected to proceed outwards, there can be distances from the central object in which the net torque exerted by the gas of the disc on the satellite object is null. These peculiar radial positions are called migration traps. The presence of these traps in which orbiting objects are expected to halt their migration was proposed for the protoplanetary disc scenario by Lyra et al. (2010), and in Bellovary et al. (2016) it was found that they can exist also in AGN discs. They estimated that more than one migration trap can form in an accretion disc, and that their distance from the SMBH is of the order of 20 to 300  $R_g$ , where  $R_g = 2GM/c^2$  is the gravitational radius of the central object, defined as a function of its mass ( $M$ ), the gravitational constant ( $G$ ), and the speed of light in the vacuum ( $c$ ). Moreover, they found the position of the migration traps to be independent from the mass of the orbiter. This means that a high number of stellar-mass objects will pile-up around a very specific radial distance from the central SMBH, facilitating the formation of binary systems.

The presence of migration traps in the framework of Type I migration is nonetheless not guaranteed in every AGN. In particular, in Grishin et al. (2024) it is argued that using prescriptions calibrated from 3D simulations (Jiménez & Masset 2017), Type I torque is always negative-definite in the AGN discs they modelled. However, they find that migration traps can form due to thermal torques in AGN less luminous than  $10^{44.5-45} \text{ erg s}^{-1}$ . These torques are caused by the thermal response of the gaseous disc to the accretion of the embedded stellar-mass BHs through their mini-discs.

Whether or not migration traps are developed in an AGN, inward radial motion of stellar-mass objects due to their interaction with the gaseous disc they are embedded in is expected to be able to cluster them in a small region. This can facilitate the gas-assisted binary genesis (Tagawa et al. 2020; DeLaurentiis et al. 2023b; Rowan et al. 2023) as well as the one from three-body encounters (Aarseth & Heggie 1976; Binney & Tremaine 2008) that are expected to take place inside AGN discs, therefore increasing the efficiency of the so-called "AGN channel" for the formation and evolution of the binaries whose mergers have been detected by the LVK collaboration. The main mechanisms discussed so far that act on the population of compact objects inside an AGN disc are visually summarised in Figure 1.5.

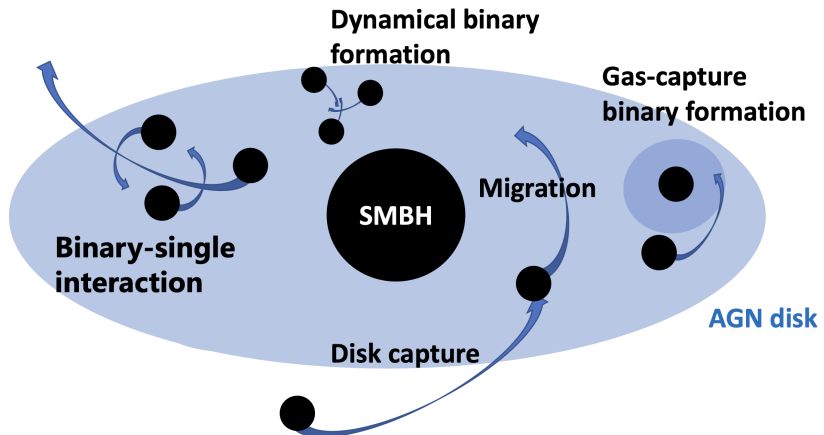


**Figure 1.5:** Visual representation of the main mechanisms that influence the population of compact objects inside and AGN disc, facilitating binary formation. Each of these processes has been presented in Section 1.4.1 or in Section 1.4.2. This Figure is adapted from Figure 3 of [Tagawa et al. \(2020\)](#).

### 1.4.3 Characteristic observable signatures of BBHs merging in AGN discs

Binary systems formed and driven to merger inside an environment such as an AGN are expected to exhibit peculiar detectable features in the GW signal they emit. These features are caused by the interaction between the compact objects and the gas the accretion disc consists of. Their identification and the characterisation of their physical cause is a very important tool for the estimation of the fractional contribution of AGN binary formation channel to the total BBH merger rate.

#### 1.4.3.1 Non-null eccentricity in the LVK band

When a binary is tight enough for the GW emission to be the dominant cause of the decrease in orbital energy, such emission is very efficient in driving the system towards a null value of eccentricity, circularising it ([Peters 1964](#)). For this reason, BBHs formed through the evolution of an isolated binary system are not expected to show any sign of eccentricity in their GW signal when

entering the LVK band, which extends approximately from  $10^1$  Hz to  $10^4$  Hz. However, hard binaries formed through repeated interactions like single-binary encounters, which are expected to happen in dynamically dense environments, can retain their eccentricity long enough to be detected (Samsing 2018; Calcino et al. 2023).

The fraction of BBHs capable of exhibiting a measurable eccentricity in the LVK band increases with respect to the general case of a dynamically dense scenario when an AGN disc-like host environment is considered. This is because in a pseudo-2D system it is likely that a single-binary encounter happens in the same plane of the orbit of the binary system, or on a plane with small inclination with respect to it (Samsing et al. 2022; Trani et al. 2024). In such a configuration, the probability of the merger happening during a single-binary encounter, and not after it, is higher with respect to the probability of the same thing happening in a spherically symmetric environment. Binaries that merge during the encounter enter the LVK band while still retaining at least part of the eccentricity they originally had, in the case of BBHs dynamically assembled via co-planar interactions is distributed as  $\mathcal{P}(e) \approx e/\sqrt{1-e^2}$  (Monaghan 1976; Stone & Leigh 2019).

The direct detection of a non-null eccentricity in a BBH merger is therefore to be considered as a smoking-gun signature of the dynamical origin of such a binary, with a non-negligible chance for the host environment to be an AGN disc. Signs of eccentricity have been spotted for specific detected events (Romero-Shaw et al. 2021), but the search of eccentric mergers is complicated by waveform systematics and by the fact that residual eccentricity contained in the GW signal can act like a systematic uncertainty, generating biases in other intrinsic binary parameters, like the spin directions of the two components (Fumagalli et al. 2024).

#### 1.4.3.2 Anti-correlation between mass ratio and effective spin parameter

The mass-weighted projection of the spins of the components of a BBH onto the orbital angular momentum is referred to as "effective inspiral spin parameter",  $\chi_{\text{eff}}$ . In the scenario in which a BBH is formed via repeated interactions in a generic dynamically dense environment, it is reasonable to assume that the directions of the spins of its components in the last phase of the inspiral and during the merger are randomly orientated with respect to each other. This is expected to be reflected in the  $\chi_{\text{eff}}$  distribution of the population of merging binaries coming from a dynamical formation scenario.

In [Callister et al. \(2021\)](#) it has been shown that at 98.7 per cent credibility it exists a relation between the value of  $\chi_{\text{eff}}$  for the detected binary mergers, and their value of the mass ratio  $q = m_2/m_1$ , where  $m_2$  and  $m_1$  are the mass of the lighter and of the heavier component, respectively. In particular, through a hierarchical Bayesian analysis on the 44 BBH merger detections listed in the second Gravitational Wave Transient Catalogue (GWTC-2), which contains the GW detections up until the first half of O3, they found that more unequal-mass binaries (low  $q$ ) are more likely to have a larger  $\chi_{\text{eff}}$ .

This anti-correlation, identified as a potential hint of binary formation in a disc-like structure, has been observed even in the third Gravitational Wave Transient Catalogue (GWTC-3), which contains also the events detected in the second half of O3 (see Figure 21 of [The LIGO Scientific Collaboration et al. 2021](#)). In particular, assuming that the heaviest stellar-mass BHs whose orbit in a Nuclear Star Cluster have a small inclination with respect to the accretion disc of the AGN present in it are more quickly captured by it with respect to the lightest ones ([Fabj et al. 2020](#)), they will spend enough time in such gaseous environment to spin-up into alignment with respect to the angular momentum of disc. These heavier spin-aligned BHs might eventually merge with lighter ones that are captured by the gaseous disc at later times. This phenomenological model, in a scenario in which a dense disc and turbulent migration are involved, is expected to produce mergers that exhibit the detected  $\chi_{\text{eff}} - q$  anti-correlation ([McKernan et al. 2022a](#)).

The same relation between effective inspiral spin parameter and mass ratio is to be expected if these systems are formed and evolve in an axisymmetric disk-like environment that allows for hierarchical mergers to happen, without the need of any assumption regarding different disc capture time-scales for compact objects of different masses ([Santini et al. 2023](#)).

## 1.5 The potential and the challenges of detecting EM counterparts of GW events

As mentioned at the beginning of Section 1.3, even after the direct detection through GWs of nearly 100 confirmed coalescence of binaries of compact objects, the fractional contribution to the total merger rate of the various binary formation paths is still unknown.

One possible way to answer this open question is to search in the GW signal of each individual event or in the properties of their overall population for

specific signatures that can be explained preferentially by one specific formation channel. Examples of such smoking-gun signatures for the AGN channel are the ones described in Section 1.4.3. Another viable approach is to directly identify in which galaxies or in which type of galaxies the merger events happened. If, for example, it is found that the fraction of BBH mergers that took place in a galaxy that hosts an AGN is significantly higher than the estimated ratio between the number of such hosts with respect to the total number of galaxies in the Universe, this would suggest that the existence of a dense gaseous accretion disc might indeed facilitate the formation of binaries of compact objects that merge in the LVK band.

Being able to directly link GW events to the hosts in which they take place is not only important to answer astrophysical questions regarding the dynamics of BBHs, the evolution of binaries of massive stars, and the characteristics of dense star clusters and of AGN discs, but it has the potential of being relevant also from the cosmological point of view. When the interferometers of the LVK collaboration detect a GW signal, they directly measure the luminosity distance between the source and the Earth. If a one-to-one association is possible between a detected BBH event and its host galaxy, it is then possible to constrain the relation between the luminosity distance measured from the GW signal and redshift directly measured from the EM radiation. Constraining such relation means constraining cosmological parameters such as the Hubble constant. This method of putting constraints on the parameters that govern the Universe on cosmological scale is referred to as "standard sirens method" (Schutz 1986) and it has already been applied in the case of the first detected merger of a Binary Neutron Star system, GW170817 (Abbott et al. 2017).

If a direct one-to-one association between the GW signal and EM one is not available, it is still possible to measure cosmological parameters using the redshift estimates of all the galaxies that are within the localisation uncertainty of the detected merger. This is the so-called "dark sirens method" (Gair et al. 2023), and it has already been applied to the data collected during the first three observing runs of the LVK collaboration (Alfradique et al. 2024).

The main limiting factor that hampers analyses involving the connection between GW events and their EM counterparts is the large uncertainty that is typically associated by GW detectors to the position of a merger of binaries of compact objects, in particular to the one of a BBH merger. Figure 1.6 shows the Cumulative Distribution Function (CDF) of the sizes of the 90 per cent Credibility Level localisation volumes ( $V_{90}$ ) of the GW events detected during the first three observing runs. The median value of such distribution is of the order of  $10^{8.5}$  cubic Megaparsecs. According to the redshift-dependent AGN

luminosity function presented in [Kulkarni et al. \(2019\)](#) this median localisation volume might contain hundreds to thousands of AGN with a bolometric luminosity greater than  $10^{45}\text{erg s}^{-1}$ , and even more regular galaxies that do not host an active nucleus. For this reason, consistently being able to confidently associate every GW event to its host environment is currently impossible.

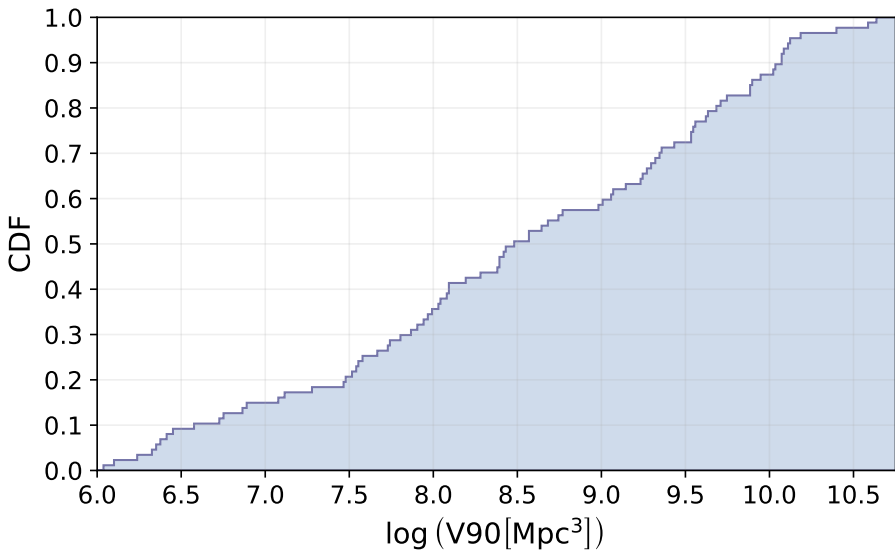


**Figure 1.6:** Cumulative Distribution Function of the sizes of the 90 per cent Credibility Level localisation volumes (V90) of the GW events detected by the LVK collaboration during the first three observing runs. From the shown distribution are excluded the localisation volumes of GW200308\_173609 and of GW200322\_091133, since these events are poorly-localised, and the available posterior samples do not allow for an estimation of their value of V90.

### 1.5.1 Spatial correlation analyses with all-sky AGN catalogues

One way of estimating what fraction of the detected GW events took place in specific types of environments is through the analysis of the spatial correlation between the positions of such potential hosts and the GW sky maps of the

measured mergers. The statistical constraining power of this approach depends on the number density of the potential hosts that are considered and on the completeness of the catalogues that are used. For this reason very luminous AGN represent an ideal class of objects of this type of studies, since all-sky catalogues with high levels of completeness are available. Two examples of such catalogues are the Million Quasars (Milliquas) catalogue ([Flesch 2023](#)) and Quaia ([Storey-Fisher et al. 2024](#)).

### 1.5.1.1 Milliquas

Milliquas is an AGN catalogue containing 1,021,800 objects in its latest version ([Flesch 2023](#)). It is presented as a collection of all the Quasars published up to June 30th, 2023. Figure 1.7 shows the mollweide projection of the sky distribution of such objects.

It is evident that, since Milliquas is an ensemble of several catalogues, its content is not uniformly distributed over the sky. In the northern sky in particular is noticeable that the region with the highest number of objects per square degree is the footprint of the Sloan Digital Sky Survey (SDSS) ([Kollmeier et al. 2019](#)), while the most crowded region in the southern sky is the footprint of the Two-degree-Field Galaxy Redshift Survey ([Colless et al. 2001](#)), which is visible in the figure as a stripe-shaped over-density of objects around an equatorial declination of  $-30^\circ$ .

While the completeness of Milliquas in the most crowded regions can be close to unity, this is not in general the case for the other parts in the sky. Nonetheless, Milliquas consists of a valid tool to establish whether there is or not a spatial correlation between detected GW events and very luminous AGN in the Local Universe. In fact, while the all-sky average number density of spectroscopically identified AGN below  $z = 0.3$  with a bolometric luminosity greater than  $10^{45}\text{erg s}^{-1}$  is approximately the 48 per cent of the number density of the same objects in the SDSS footprint, this fraction reaches approximately the 87 per cent when AGN brighter than  $10^{46}\text{erg s}^{-1}$  are considered.

### 1.5.1.2 Quaia

Quaia ([Storey-Fisher et al. 2024](#)) is an all-sky AGN catalogue containing objects identified ad extra-galactic by the Gaia mission ([Gaia Collaboration et al. 2016](#)) in its third data release ([Gaia Collaboration et al. 2023](#)) that have a counterpart observed by the Wide-field Infrared Survey Explorer (WISE) ([Wright et al. 2010](#)) and contained in the unWISE catalogue ([Lang 2014; Meisner et al. 2019](#)).

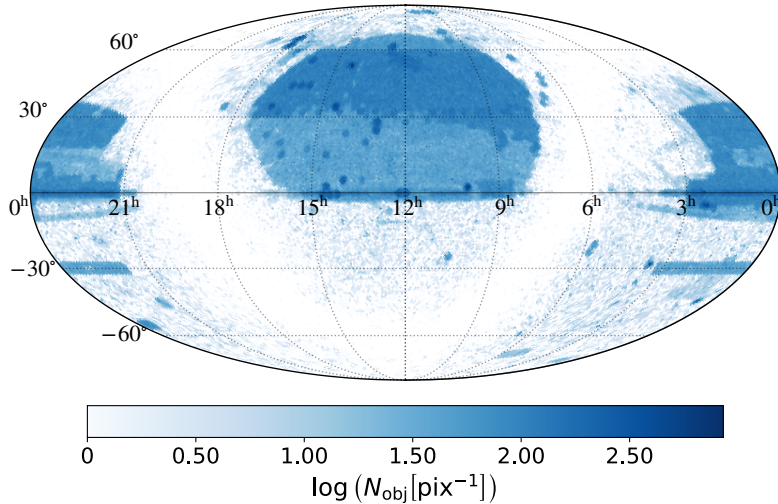


**Figure 1.7:** Mollweide projection of the latest version of the Milliquas catalogue (v8). The distribution of objects is displayed in a Healpix map with NSIDE=64. The colour of each pixel indicates the logarithm of the number of objects present in the catalogue in that sky position.

All the objects in Quaia have passed a series of selections based on the proper motions and the colours of the objects, aimed to increase the purity of the sample. The final result is an all-sky catalogue which contains 1,295,502 quasars with a magnitude in the Gaia G band lower than 20.5. Their sky distribution is shown in Figure 1.8.

The redshift estimate for each object in Quaia is evaluated by training a  $k$ -Nearest Neighbor model using as training set the AGN in Quaia that have an available spectroscopic redshift estimate in SDSS. What makes Quaia an ideal instrument for spatial correlation analyses is its remarkably uniform distribution of objects over the whole sky, once the region containing the galactic plane is excluded, together with its high level of completeness.

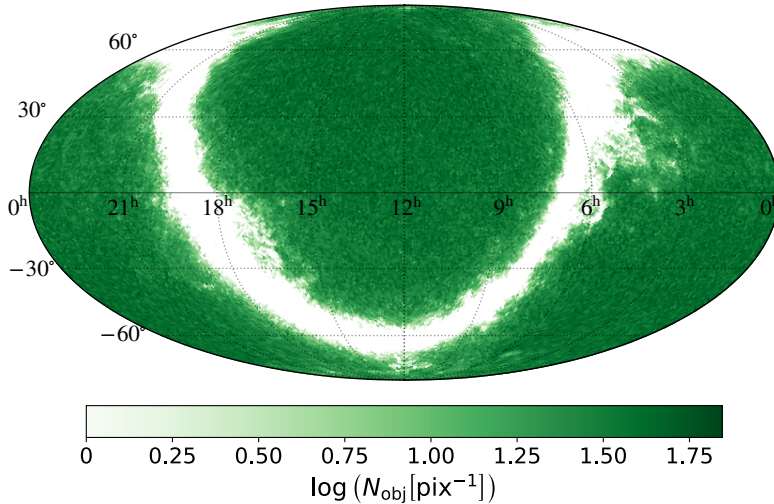


**Figure 1.8:** Mollweide projection of the all sky AGN catalogue Quaia. The distribution of objects is displayed in a Healpix map with NSIDE=64. The colour of each pixel indicates the logarithm of the number of objects present in the catalogue in that sky position. This Figure is also present in the work described in Chapter 4 of this thesis.

### 1.5.2 Spatial correlation analyses with unusual AGN flaring activities

Binary mergers happening in an AGN disc are expected to produce an EM counterpart, even if not always detectable, due to the interaction between the gas and the components of the binary or the remnant of the GW event (Bartos 2016a; McKernan et al. 2019). In particular, it has been proposed that an observable flare coming from an AGN can be produced when the gas that interacts with the recoiled merger remnant which is traveling through the disc produces a shocked Bondi tail (Ostriker 1999; Antoni et al. 2019). Such flare is modeled to be manifest when the kicked BH reaches the surface of the disc with an optical depth of  $\tau = 1$ .

Recently, 20 AGN flares have been labeled by Graham et al. (2023) as potential EM counterparts to the GW events detected during the third observing run of the LVK collaboration. These EM transients were found not compatible with being coming from SNe, Tidal Disruption Events, microlensing events,

or regular AGN variability. They were found by analysing AGN light curves observed by the Zwicky Transient Facility (ZTF) (Bellm et al. 2019; Graham et al. 2019), a time-domain survey that since March 2018 covers the Northern sky every 2-3 nights, observing in the  $g$  and in the  $r$  band.

The sky distribution of the 20 selected flares is shown by the pink round markers in Figure 1.9.

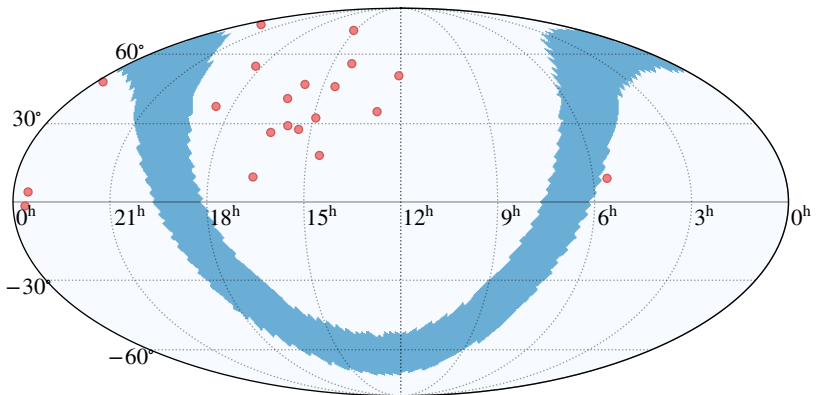


**Figure 1.9:** Mollweide projection of the positions of the 20 AGN flares identified in Graham et al. (2023) as potential counterparts to BBH mergers (pink round markers). The distribution of objects is displayed in a Healpix map with NSIDE=32. The pixel corresponding to a galactic declination  $b$  between  $-10^\circ$  and  $10^\circ$  are in light-blue. This Figure is also present in the work described in Chapter 5 of this thesis.

The low volume number density of these unusual AGN flares, together with the fact that they are transient, not permanent EM signatures makes them ideal tools for spatial and temporal correlation analyses aimed to check whether it is plausible or not that a causal correlation exists with the mergers detected by the LVK collaboration. This is because the probability of having one of these flares matching by pure chance both spatially and in time with a BBH merger, without any physical causality relation between the two signals is typically low. For this reason, if such a causal connection exists, it should be possible to assess it confidently.

## 1.6 In this thesis

This thesis contains four studies I have conducted together with my co-authors. All of these works revolve around the investigation of the spatial correlation between AGN and GW events detected by the LVK collaboration. This analyses have required the creation and the characterisation of suitable all-sky AGN catalogues and the development of a statistical framework with a Likelihood function able to take into account the properties of such catalogues and of the sky maps of the detected mergers. The results this method consist of observational constraints on the efficiency of the AGN channel, which can be used as a proxy for constraining the properties of the accretion discs themselves.

In Chapter 2 I present the results of a Likelihood ratio method which applies the statistical framework presented in [Bartos et al. \(2017a\)](#) to O3-like sky GW detection I have simulated. This method is used to calculate the number of detections needed in order to be able to reject the hypothesis according to which there is no correlation between AGN and BBH mergers. We estimate to what fraction of the total merger rate the AGN binary formation channel has to contribute to have the possibility of rejecting the no-connection hypothesis with the number of detections obtained during O3. This is repeated varying the number density of the AGN that are considered as potential hosts. For example, we estimate that the number of detections performed in O3 potentially allows such a rejection with a  $3\sigma$  confidence if rare (i.e. with number densities lower than  $10^{-7.5} \text{Mpc}^{-3}$ ) AGN are considered, and if the the accretion disc-assisted binary formation channel contributes to a significant fraction (30 per cent or more) of the total merger rate.

In Chapter 3 I first describe an updated version of the statistical method presented in Chapter 2. This consists of a new Likelihood function, the maximisation of which can put observational constraints on what fraction of the detected BBH mergers has originated in an AGN. In particular, this new statistical framework we developed is able to take into account the incompleteness of the AGN catalogue that uses, and the exact position of each potential host within the 90 per cent Credibility Level localisation volume of the GW detections. After testing its validity on mock data, we apply this method to the 30 BBH mergers detected during the first three observing runs of the LVK collaboration with a 90 per cent Credibility Interval on the luminosity distance entirely contained within  $z = 0.3$ . In particular we cross-match these events with three different catalogues of AGN in the same redshift range. These catalogues are created selecting objects from Milliquas that are also present in unWISE and

that have a spectroscopic estimate of their redshift. What characterise each of these catalogues are the different thresholds on bolometric luminosity that have been used to create them. We find that the fraction of the detected BBH mergers that has originated in an AGN more luminous than  $10^{45.5} \text{ erg s}^{-1}$  ( $10^{46} \text{ erg s}^{-1}$ ) is not greater than 49 (17) per cent at a 95 per cent Credibility Level. To our knowledge, these are the first observational constraints on the efficiency of the AGN channel for the formation of binaries systems that merge in the LVK waveband.

In Chapter 4 is presented a generalisation of the results described in Chapter 3. In particular we apply the same spatial correlation-based statistical approach to infer the fractional contribution of the AGN formation channel to the total merger rate, using as input data the Quaia all-sky AGN catalogue and the sky maps of all the GW events detected until the first half of the fourth observing run of the LVK collaboration (O4a). To do this we first estimate the bolometric luminosity of each object contained in Quaia up to  $z = 1.5$ . In the same range, we estimate for the first time the completeness of this catalogue as a function of redshift and luminosity. With respect to the work presented in Chapter 3 we therefore expand our dataset. We number of sky maps used go from 30 to 159 on the entire redshift range covered by the LVK interferometers. Moreover, the high level of completeness of Quaia allows us to put constraints on the relation between GW events and AGN over a wider range of bolometric luminosity. In particular we find that no more than the 23 (28) per cent of the detected mergers have happened in an AGN brighter than  $10^{45} \text{ erg s}^{-1}$  ( $10^{45.5} \text{ erg s}^{-1}$ ) at a 95 per cent Credibility Level.

Finally, in Chapter 5 I present a spatial and temporal correlation analysis aimed to investigate whether there is or not a causal connection between the GW events detected during O3 and the 20 unusual AGN flares proposed in [Graham et al. \(2023\)](#) as potential EM counterparts to binary mergers. We find that current data favour the hypothesis according to which there is no causal connection between such transients and the LVK detections. Performing Monte Carlo realisations of realistic catalogues of flares, we find that the number of spatial and temporal matches between the detected GW events and the observed EM transients is to be expected in the case of random-chance association, without any physical relation between the two types of signal. The BBH mergers the sky maps of which have a match with one of the 20 flares presented in [Graham et al. \(2023\)](#) are characterised by components that occupy the high-mass end of the stellar-mass BH mass spectrum inferred by ([The LIGO Scientific Collaboration et al. 2021](#)). We find that this can be explained by the fact that these events are in general associated to large uncertainty on their position, therefore they

have a high chance of having an AGN within their 90 per cent Credibility Level localisation volume just because of random association.

## 1.7 Future outlook

All the work presented in this thesis shows that the efficiency of the various formation paths proposed for merging stellar-mass BBHs can already be constrained with the data that has been so far collected. However, all the results of the spatial correlation analyses here described are purposely agnostic from the point of view of the underlying physical model. This means that in the statistical framework no prior knowledge is assumed regarding the distribution of the intrinsic binary parameters one should expect to measure in events coming from a specific formation channel, such as the AGN one.

Introducing physically-informed priors on parameters such as the eccentricity of the binaries, the masses of their components, and their spins will enable the possibility of performing a new type of spatial correlation-based investigation, which might lead to different constraints with respect to the ones described in the following chapters of this thesis. Moreover, physically-informed spatial correlation-based methods will also help to rank the different intrinsic properties of the merging binaries as a function of the amount of information that the assumption of a non-uniform prior on them is able to add to the analysis. This will consist of an indication regarding which are the binary parameters that are more tightly related to the host environment where the system has formed and evolved.

Another future development of spatial correlation analyses aimed to investigate the connection between BBH mergers and potential rare host environments is related to making forecasts on the constraining power of GW detectors that will start to operate in the next decade, like third-generation ground-based ones such as Einstein Telescope (ET) (Maggiore et al. 2020) and Cosmic Explorer (CE) (Reitze et al. 2019) and space-borne ones like the Laser Interferometer Space Antenna (LISA) (Amaro-Seoane et al. 2017). The sensitivity of ET and CE will be two orders of magnitude better with respect to the one of Advanced LIGO (Vitale & Evans 2017). However, the expected uncertainties on the sky positions and luminosity distances of the detected events are too large to allow a consistent one-to-one association between BBH mergers and their host galaxy (Pieroni et al. 2022). Nonetheless, analyses like the ones presented in this thesis will have their constraining power greatly enhanced by the fact that thousands of events every year are currently expected to be detected with an

uncertainty on their position in the sky of 1 to few square degrees. Since these third-generation detectors are expected to identify BBH mergers up to  $z \approx 30$  (Hall & Evans 2019), it will be possible to incorporate a redshift-dependence in the Likelihood function and then estimate the fractional contribution to the total BBH merger rate of the different proposed formation paths as a function of cosmic time.

Similar forecasts can be already made also concerning the mergers of binaries of Massive Black Holes with masses between  $10^5 M_{\odot}$  and  $10^7 M_{\odot}$  that will be observed by LISA. These mergers are expected to take place after the merger of two galaxies, if the two central BHs form a binary tight enough to efficiently lose orbital energy via GW emission, until they merge. The uncertainty on the sky position coming from LISA's detections is estimated to be of the order of one to 10 square degrees for mergers happening at  $z = 1$  (Mangiagli et al. 2020). One strength of the statistical method presented in this thesis is that it can be applied to any kind of sky map and to any catalogue of potential hosts. Therefore no major adjustments to it are needed in order to make it applicable to LISA data. Cross-matching the sky maps of the detected Massive Black Hole binary mergers with catalogues of galaxies that are either currently observed as undergoing a merger event, or that are thought to have just experienced one, like starburst galaxies or E+A galaxies (Bekki et al. 2005), will help in putting constraints on the delay between the moment in which two galaxies start to merge and the moment in which their central Massive Black Holes coalesce. This constraint will be important to better understand the interactions between these massive objects and the stellar and gaseous content of galaxies, as well as the mechanisms that can bring binaries of SMBHs to be tight enough to make GW emission efficient.

Both in the case of ground based and of space-borne GW detectors, an important step of spatial correlation based methods to characterise the formation paths of GW events is to create the best possible catalogues of potential hosts and to characterise them. These catalogues should ideally be all-sky and complete. Future developments of this branch of GW astronomy therefore include the creation of these catalogues, and the mapping of their number density and completeness as a function of parameters like redshift, sky position, intrinsic luminosity, and accretion rate. This task is crucial for being able to put trustworthy constraints, but is not trivial, given the different properties and limitations of different surveys and the assumptions that have to be made when estimating the intrinsic properties of potential hosts, starting from observable. An example of this is that in order to calculate the bolometric luminosity of an AGN one has to assume the shape of its Spectral Energy Distribution (SED)

and the bolometric correction needed to convert the luminosity emitted in a band of the EM spectrum into the bolometric one.



# 2

# DETECTABILITY OF A SPATIAL CORRELATION BETWEEN STELLAR-MASS BLACK HOLE MERGERS AND ACTIVE GALACTIC NUCLEI IN THE LOCAL UNIVERSE

Work published in **N. Veronesi, E. M. Rossi, S. van Velzen, R. Buscicchio, 2022, *Monthly Notices of the Royal Astronomical Society*, 514, 2092.** Reprinted here in its entirety.

## Abstract

The origin of the Binary Black Hole (BBH) mergers detected through Gravitational Waves (GWs) by the LIGO-Virgo-KAGRA (LVK) collaboration remains debated. One fundamental reason is our ignorance of their host environment, as the typical size of an event’s localization volume can easily contain thousands of galaxies. A strategy around this is to exploit statistical approaches to assess the spatial correlation between these mergers and astrophysically motivated host galaxy types, such as Active Galactic Nuclei (AGN). We use a Likelihood ratio method to infer the degree of GW-AGN connection out to  $z = 0.2$ . We simulate BBH mergers whose components’ masses are sampled from a realistic distribution of the underlying population of Black Holes (BHs). Localization volumes for these events are calculated assuming two different interferometric network configurations. These correspond to the configuration of the third (O3) and of the upcoming fourth (O4) LVK observing runs. We conclude that the 13 BBH mergers detected during the third observing run at  $z \leq 0.2$  are not enough to reject with a  $3\sigma$  significance the hypothesis according to which there is no connection between GW and AGN more luminous than  $\approx 10^{44.3} \text{erg s}^{-1}$ , that have number density higher than  $10^{-4.75} \text{Mpc}^{-3}$ . However, 13 detections are enough to reject this no-connection hypothesis when rarer categories of AGN

are considered, with bolometric luminosities greater than  $\approx 10^{45.5} \text{ erg s}^{-1}$ . We estimate that O4 results will potentially allow us to test fractional contributions to the total BBH merger population from AGN of any luminosity higher than 80 per cent.

## 2.1 Introduction

Since the first direct GW detection has been announced (Abbott et al. 2016), the two interferometers of Advanced LIGO (LIGO Scientific Collaboration et al. 2015) and the one of Advanced Virgo (Acernese et al. 2015) have measured the signal coming from tens of compact objects mergers in three observing runs (Abbott et al. 2019, 2021a, 2024, 2023a). Thanks to improved sensitivities and the addition of a fourth detector, KAGRA (Somiya 2012; Aso et al. 2013), this number will grow in the upcoming years (Abbott et al. 2018).

Different formation pathways for these merging BBHs have been proposed (Mapelli 2021). They might arise from the evolution of isolated stellar binary systems (Dominik et al. 2012; Belczynski et al. 2016; Spera et al. 2019), or form in dense environments, in which dynamical interactions can efficiently drive binaries of compact objects towards the merger (Stone 2017; Rodriguez & Loeb 2018; Antonini et al. 2019; Gerosa & Berti 2019; Rodriguez et al. 2021; Rizzuto et al. 2021). One particular example of such environments can be the accretion disk around Super Massive Black Holes (SMBHs) in Active Galactic Nuclei (Bartos et al. 2017b; Stone et al. 2017; McKernan et al. 2018; Ford et al. 2019; Samsing et al. 2020; Gayathri et al. 2021). It has been shown that in such an environment, compact objects can migrate towards a radius close to the one of the innermost stable circular orbit, and there be trapped for the remaining AGN lifetime (Peng & Chen 2021). The large number density of compact objects and the high escape velocity in that region can facilitate the occurrence of hierarchical mergers (i.e. mergers in which at least one of the two components is the remnant of a previous merger) (Yang et al. 2019; Gerosa & Fishbach 2021; Wang et al. 2021b). The mass of the remnants of hierarchical mergers can be higher than the lower bound of the Pair Instability mass gap predicted by stellar formation models (Farmer et al. 2019; Woosley & Heger 2021). This formation pathway has therefore the theoretical advantage of being able to explain the non-vanishing merger rate inferred for binaries with components heavier than  $50M_{\odot}$  (The LIGO Scientific Collaboration et al. 2021).

There are potentially several ways to address the formation pathways' open question and in particular to assess a plausible connection between GW events

(BBH mergers in particular) and AGN. The most straightforward would be to directly detect an ElectroMagnetic (EM) counterpart in coincidence with the GW event. This might be possible in dense environments like the accretions disks of AGN (McKernan et al. 2019; Wang et al. 2021a), and such a counterpart might have already been observed (Graham et al. 2020) (However, see also Ashton et al. 2021). The typical localization volumes of GW events make their association with an EM counterpart challenging. The interferometers currently operating are in fact only able to associate to GW detections comoving volumes that can easily contain thousands of different galaxies. Similarly to what happens in the case of the emission of an EM counterpart, a companion GW signal can be originated from the same source of a detected event in the case of mergers happening near a SMBH. These events could therefore be identified by the independent detection of an associated gravitational echo (Kocsis 2013; Gondán & Kocsis 2021).

Another way to infer the origin of the detected events is by statistically comparing the measured source population properties, such as mass and spin distributions, with model expectations. This kind of analysis has been done for several potential host environments, including AGN (McKernan et al. 2020; Gayathri et al. 2021; Tagawa et al. 2021; ?; Li 2022). While the expected distribution of spin parameters is still debated, all these analyses conclude that heavy ( $\geq 50M_{\odot}$ ) stellar-mass BHs are expected to be generated through the AGN formation channel.

Finally, the increasing number of detections allows us to exploit statistical approaches to explore the spatial correlation between GW events and specific types of host environments. These approaches can overcome the big challenge of large localization volumes. Bartos et al. (2017a) proposed a statistical likelihood-ratio-based method to find out how many GW detections would be needed to establish which fraction of BBH mergers detected through GWs happened in an AGN. This earlier work was based on the GW localization volume distribution expected for detections performed by the LIGO-Virgo network at design sensitivity and assuming only mergers of pairs of  $10M_{\odot}$  BHs.

In this work, we present an analysis based on the same method, although we use simulated GW detections constructed from the latest results on the inference of the underlying BBH component masses' distribution. To simulate these detections we employ detectors' sensitivities representative of the third observing run of the LIGO and Virgo interferometers, as well as those expected to characterize the fourth one, when KAGRA will join the network.

This paper is organized as follows: In Section 2.2 we provide an overview of all the steps of the analysis, with details in the following subsections. How we

simulated the GW detections the localization volumes of which are needed in the statistical analysis is described in subsection 2.2.1, while in subsection 2.2.2 we present how this statistical investigation works. The results of our works are presented in section 2.3. Finally, in Section 2.4 we draw conclusions and discuss the next steps to improve our fit to observed data.

## 2.2 Method

To investigate the spatial correlation between Gravitational Waves 90 per cent Credibility Level localization volumes (hereafter "V90") and the positions of AGN in the local Universe, we first build two catalogues of simulated GW detections anchored in current observations. For the first, we simulate the response of the detector network active during O3. For the second catalogue, we use the same synthetic population of BBHs, and we simulate their detection by the interferometric network configuration expected for O4, which includes also KAGRA. To create the simulated detections we first sample the joint probability distribution of the binary mass ratio  $q = m_2/m_1$  and primary component's mass  $m_1$ ; which is, by definition, greater than the mass of the secondary one,  $m_2$ . We then sample the spin distribution for each binary component, the distribution for the inclination of the orbital plane with respect to the line of sight, and for the luminosity distance between the position of the event and the detectors. The assumed distributions, as well as the configurations and the detector sensitivity curves used in our simulations, are described in section 2.2.1.

Once the mock observations have been simulated, we evaluate V90 for all the detections using BAYESTAR ([Singer & Price 2016](#)), a sky localization algorithm able to perform in a few seconds a Bayesian, non-Markov Chain Monte Carlo analysis.

We then use the newly created distribution for V90 to sample a set of comoving volumes that are then exploited in an algorithm based on the likelihood-ratio method described in [Bartos et al. \(2017a\)](#). This algorithm crossmatches the positions of the GW localization volumes with the positions of AGN in the Local Universe, which are assumed to be isotropically distributed in comoving volume. The final output of this algorithm (described in detail in 2.2.2) is the number of GW detections needed to test the hypothesis according to which a certain fraction ( $f_{\text{AGN}}$ ) of the detected BBH mergers happened in an AGN; having the chance of rejecting the no-correlation hypothesis (none of the detected BBH mergers happened in an AGN) with a given confidence.

## 2.2.1 Simulation of GW detections

A distribution of V90 is required by our statistical method. We obtain such distribution by simulating several realistic GW detections for both O3 and O4 configurations. We describe the details of these simulations in the following sections.

### 2.2.1.1 Source population

Our simulated GW events are derived from the population analysis based on the latest results of the LVK Collaboration. We assume for  $m_1$  the POWER LAW + PEAK analytical model presented in [Abbott et al. \(2021c\)](#) and we simultaneously sample values of  $m_1$  and  $q$  from their joint posterior probability distribution. This distribution has been obtained through the standard hierarchical bayesian analysis presented in [The LIGO Scientific Collaboration et al. \(2021\)](#) and posterior samples are publicly available. The secondary component's mass is then calculated as  $m_2 = qm_1$ . We use the same mass distribution to simulate BBH mergers irrespective of them happening in an AGN. This is done to maintain our estimate conservative and model-independent. We, therefore, neglect the effects of the hypotheses according to which GW events originated in dense environments are more likely to involve higher-mass BHs with respect to the ones that originated from an isolated binary system.

For simplicity, we assume for all the BHs the spin direction to be aligned with respect to the binary orbital angular momentum, and a uniform spin magnitude distribution between 0 and 1. The distribution of V90 is not expected to be significantly affected by such an assumption.

The simulated binaries are uniformly distributed in comoving volume and their inclinations  $\iota$  are sampled according to a uniform distribution over  $\arccos(\iota)$ . The cosmological parameters we assume during our analysis are the ones inferred from the Planck Cosmic Microwave Background observations ([Planck Collaboration et al. 2020](#)).

### 2.2.1.2 The network of detectors

Next, we simulate the network of detectors. The whole analysis presented in this work is done for two different settings: the first one aims at reproducing the V90 distribution for O3, while the second one aims to forecast the distribution of the detected volumes expected during O4. In both cases, we assume a duty cycle of 78 per cent for all the different detectors individually, and we keep a network Signal-to-Noise Ratio (SNR) threshold of 8, adding a Gaussian measurement

error to the SNR and requiring that at least two detectors contribute to the network SNR with an individual  $\text{SNR} \geq 4$ . The signals of the injected events are then compared with the detectors' noise in the  $10 - 5000\text{Hz}$  frequency range. We use an IMRPhenomD waveform type ([Husa et al. 2016](#); [Khan et al. 2016](#)) to model the injections.

To reproduce the volume distribution of the events measured during O3, we model a network of three detectors: LIGO Hanford, LIGO Livingstone, and Virgo, using the sensitivities characterized by the following IDs: `ALIGOMID-LOWSENSITIVITYP1200087` for the two LIGO interferometers, and `ADVMID-LOWSENSITIVITYP1200087` for Virgo interferometer.

For the O4 predictions, we add a fourth KAGRA-like interferometer, and we change the sensitivity curves of each detector. Specifically, we use `ALIGOADVO4T1800545` for LIGO and Virgo detectors, and `ALIGOKA-GRA80MPCT1800545` for KAGRA.

### 2.2.1.3 Evaluation of 90% CL localization volumes

For O3 (O4), out of the 200k (100k) injections, 663 (1737) have a SNR higher than the threshold. Out of these simulated mergers whose signals exceed the SNR threshold (hereafter referred to as *detections*), 274 for O3 and 317 for O4 have a measured value for the luminosity distance that corresponds to  $z \leq 0.2$ . We evaluate the value of  $V_{90}$  for each of these low-redshift events using the BAYESTAR algorithm ([Singer & Price 2016](#)). For these close events, we show the cumulative distribution of  $V_{90}$  in Figure 2.1. The blue and green histograms are detections simulated for O3 and O4, respectively. The top axis shows the expectation value of the number of AGN within the corresponding localization volume, assuming a uniform number density of AGN equal to  $n_{\text{AGN}} = 10^{-4.75}\text{Mpc}^{-3}$ . The same value for this parameter was used in [Barrios et al. \(2017a\)](#) and [Corley et al. \(2019\)](#). This number density corresponds to AGN with a bolometric luminosity higher than  $\approx 10^{44.3}\text{erg s}^{-1}$  in the Local Universe. This value for the minimum bolometric luminosity for AGN at a specific number density has been obtained by integrating the double power law that represents the AGN LUMINOSITY FUNCTION in ([Hopkins et al. 2007](#)), using the best fit values for  $z = 0.1$ . This holds for all the values of bolometric luminosities mentioned hereafter.

As a sanity check, we verify that our sample of  $V_{90}$  from O3 simulations and the values of  $V_{90}$  for the 13 observations of O3 with redshift  $z \leq 0.2$  are compatible with a single common distribution. We do this with a 2 samples Kolmogorov-Smirnov test. We find that the hypothesis according to which the

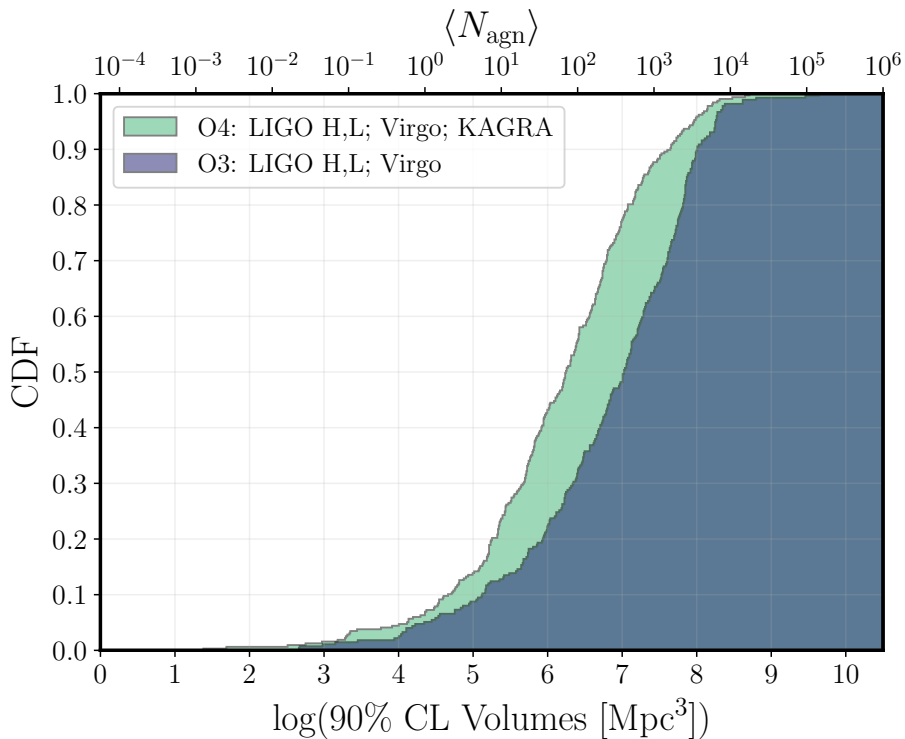


**Figure 2.1:** Cumulative distributions of the 90% CL localization volumes of simulated GW events with  $\text{SNR} > 8$  and  $z \leq 0.2$ . The blue and the green histograms are for O3 and O4 runs, respectively. The top axis shows the expected number of AGN within the corresponding localization volume, for a homogeneous distribution of AGN with a number density of  $n_{\text{AGN}} = 10^{-4.75} \text{ Mpc}^{-3}$ .

two samples come from the same distribution cannot be rejected ( $p$ -value  $\approx 0.39$ ).

### 2.2.2 Minimum number of GW detections to test the AGN origin

We consider a Universe where a fraction of GW events  $f_{\text{AGN}}$  originate in an AGN-type of galaxy. Our goal is to calculate how many GW detections are needed to infer this AGN-BBH mergers connection; more precisely, the minimum number  $N_{\text{GW}}^{3\sigma}$  of GW detections below  $z = 0.2$  needed to reject with a  $3\sigma$  significance the hypothesis of no-connection between detected BBH mergers and AGN. We evaluate  $N_{\text{GW}}^{3\sigma}$  as a function of the fraction  $f_{\text{AGN}}$  of GW events originated from an AGN. We calculate such a number by investigating the spatial correlation between AGN positions (assumed to be uniformly distributed in comoving volume) and the localization volumes of simulated GW detections, starting from the statistical approach presented in [Bartos et al. \(2017a\)](#).

We assume that GW localization volumes are spherical, and calculate the radius  $r_{\text{gw}}^{\max}$  of the biggest volume depicted in Figure 2.1. We then populate with AGN a sphere of radius

$$r = d_{\text{L}}(0.2) + r_{\text{gw}}^{\max}, \quad (2.1)$$

where  $d_{\text{L}}(0.2)$  is the luminosity distance corresponding to  $z = 0.2$ . The centre of this sphere corresponds to the position of the interferometric network we simulate the detections of. All the AGN are treated as point sources and their distribution is uniform in comoving volume. We then consider a set of  $N_{\text{gw}}$  GW detections and draw for each of them a value of  $V_{90}$  from the relevant distribution in Figure 2.1. We denote with  $V_i$  the localization volume associated to the  $i$ -th detection. We require that the centre of each  $V_i$  has a distance from the interferometric network smaller than  $d_{\text{L}}(0.2)$ . A fraction  $f_{\text{AGN}}^{\text{eff}} = 0.9f_{\text{AGN}}$  of the centres of the localization volumes are set in order to correspond to the position of an AGN. We here use  $f_{\text{AGN}}^{\text{eff}}$  instead of  $f_{\text{AGN}}$  to take into account the fact that we are here dealing with 90 per cent CL localization volumes, and therefore we expect only the 90 per cent of the origins of the simulated GWs to be actually located in such volumes.

We then count the number  $N_i$  of AGN in each localization volume  $V_i$ . Equation 2.1 ensures that each GW localization volume is entirely contained in our simulated Universe.

For every set of  $N_{\text{GW}}$  simulated GW detections, we then calculate

$$\lambda = 2 \log \left[ \frac{\mathcal{L}(f_{\text{AGN}})}{\mathcal{L}(0)} \right], \quad (2.2)$$

where  $\mathcal{L}(0)$  and  $\mathcal{L}(f_{\text{AGN}})$  are the likelihood functions of the no-connection hypothesis and of the  $f_{\text{AGN}}$ -correlation hypothesis, respectively. These likelihood functions are constructed assuming a Poissonian distribution for  $N_i$ . See [Bartos et al. \(2017a\)](#) for more details.

Every simulation is therefore associated to a value of  $\lambda$  that depends on  $n_{\text{AGN}}$ ,  $N_{\text{GW}}$ ,  $f_{\text{AGN}}$ , the value of V90 of each simulated GW event, and the number  $N_i$  of AGN within such volume.

We expect  $\lambda$  to be positive in simulations in which  $N_{\text{GW}} f_{\text{AGN}}^{\text{eff}}$  localization volumes' centres correspond to an AGN. We refer to simulations that satisfy this requirement as signal realizations, and to the value of  $\lambda$  obtained from each of them as  $\lambda_s$ . Likewise, we call  $\lambda_b$  every value of  $\lambda$  that is obtained from a background realization. These realizations are simulations in which the centres of the localization volumes are randomly distributed, uniformly in comoving volume. We, therefore, expect  $\lambda_b$  to be negative.

We perform 3,000 signal realizations and the same amount of background realizations, for each set of values of  $N_{\text{GW}}$ ,  $n_{\text{AGN}}$  and  $f_{\text{AGN}}$ .

Once a value for  $f_{\text{AGN}}$  and for  $n_{\text{AGN}}$  has been set, an increase in  $N_{\text{GW}}$  leads to a greater separation between the distribution of  $\lambda_s$  and the distribution of  $\lambda_b$ .

The target degree of significance in the rejection of the no-connection hypothesis is reached when the median value of the distribution of  $\lambda_s$  corresponds to a p-value lower than 0.00135 when compared to the  $\lambda_b$  distribution.

To evaluate  $N_{\text{GW}}^{3\sigma}$  for a specific value of  $f_{\text{AGN}}$ , we calculate 30 p-values, keeping such parameter fixed together with  $N_{\text{GW}}$ . We repeat these calculations for multiple values of  $N_{\text{GW}}$ , and then fit the trend of the average p-value for a given  $N_{\text{GW}}$  as a function of  $N_{\text{GW}}$  itself. Such trend is well fitted by a decreasing exponential function for every value of  $f_{\text{AGN}}$  we investigated. Once the parameters of these fits are known, we invert the fit function and calculate the number of detections corresponding to a p-value of 0.00135. We repeat the same analysis for 6 different values of  $f_{\text{AGN}}$  between 0.5 and 1.

## 2.3 Results

### 2.3.1 Minimum number of GW detections with fixed $n_{\text{AGN}}$

In this section, we present the results obtained keeping the AGN number density parameter fixed to  $n_{\text{AGN}} = 10^{-4.75} \text{Mpc}^{-3}$ . The trend of  $N_{\text{GW}}^{3\sigma}$  as a function of  $f_{\text{agn}}$  is shown in Figure 2.2. The error bars correspond to the standard deviation of 1,000 values of  $N_{\text{gw}}^{3\sigma}$  calculated for each of the 6 values of  $f_{\text{agn}}$  we test. The results for O3 and O4 are represented by the blue squares and the green dots, respectively.

The trend of  $N_{\text{GW}}^{3\sigma}$  as a function of  $f_{\text{agn}}$  is fitted with the same functional form used in [Bartos et al. \(2017a\)](#), which is the following:

$$N_{\text{GW}}^{3\sigma} = af_{\text{agn}}^{-b}. \quad (2.3)$$

The best fit values we obtain in the case of the O3 simulated events are  $a = 35.8 \pm 1.2$  and  $b = 1.73 \pm 0.08$ , while for O4 simulated events we obtain  $a = 20.7 \pm 0.7$  and  $b = 1.73 \pm 0.11$ .

We then perform the same analysis for O3 with a lower ( $2\sigma$ ) significance threshold for the rejection of the no-connection hypothesis. In this case, the best-fit values for the fit are  $a = 17.7 \pm 0.5$  and  $b = 1.57 \pm 0.12$ .

### 2.3.2 Significance of the no-connection hypothesis rejection as a function of $n_{\text{AGN}}$ and $f_{\text{agn}}$

During the third observing run of the LVK Collaboration, 13 detected BBH mergers have an expectation value of redshift lower than 0.2. As we can infer from the results presented so far, with this low number of "closeby" events it is not possible to reject with a  $2\sigma$  significance the no-connection hypothesis for any value of  $f_{\text{agn}}$ , assuming  $n_{\text{AGN}} = 10^{-4.75} \text{Mpc}^{-3}$ .

Nonetheless, decreasing the value of  $n_{\text{AGN}}$ , every GW detection becomes more significant, and a lower number of detection is needed to rule out the no-connection hypothesis.

Hence, we perform the same analysis as above but keeping  $N_{\text{GW}}$  fixed at the value of 13, and varying both  $f_{\text{agn}}$  and  $n_{\text{AGN}}$ . For each point in this 2D parameter space, we determine the p-value associated to the median of the distribution of  $\lambda_s$  when compared to the distribution of  $\lambda_b$ .

The results of such analysis are shown in Figure 2.3. The white dashed (solid) line divide the parameter space into two decision regions, corresponding

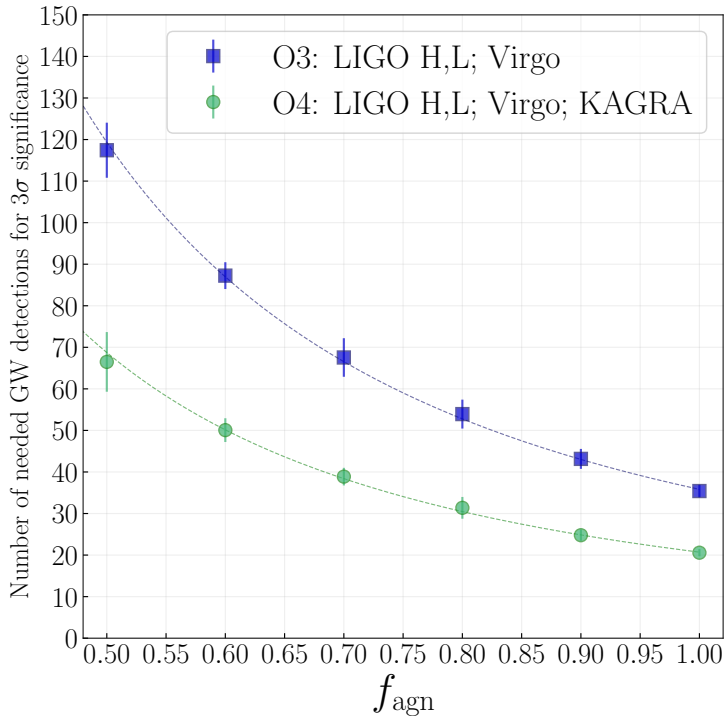


**Figure 2.2:** Number of GW detections needed to reject with a  $3\sigma$  significance the no GW-AGN connection hypothesis as a function of the fraction of GW originated from an AGN. The error bars represent the standard deviation over 1,000 realizations of  $N_{\text{GW}}^{3\sigma}$  obtained for each tested value of  $f_{\text{agn}}$ . The results for the third and the fourth observing run of LVK Collaboration interferometers are represented by the blue squares and the green dots, respectively. The data points have been fitted with the following function:  $n_{\text{AGN}}^{3\sigma} = af_{\text{agn}}^{-b}$ . The best-fit values for the O3 scenario are  $a = 35.8 \pm 1.2$  and  $b = 1.73 \pm 0.08$ , while for the O4 scenario they are  $a = 20.7 \pm 0.7$  and  $b = 1.73 \pm 0.11$ . The best-fit function for O3 (O4) is represented by the blue (green) dashed line.

to parameter choices for  $f_{\text{agn}}$  and  $n_{\text{AGN}}$  whose associated p-values are lower or higher than 0.00135 (0.02275), i.e. a significance higher or lower than  $3\sigma$  ( $2\sigma$ ), respectively. The no-connection hypothesis can be rejected accordingly in the respective regions.

For example, with 13 GW detections and assuming a number density of AGN  $n_{\text{AGN}} = 10^{-7.50} \text{Mpc}^{-3}$ , we can, in principle, reject the no-connection hypothesis with a  $3\sigma$  ( $2\sigma$ ) significance if  $f_{\text{agn}} \geq 0.40$  ( $f_{\text{agn}} \geq 0.25$ ). Such a low number density corresponds, in the local Universe, to AGN with a bolometric luminosity  $\approx 10^{46.2} \text{erg s}^{-1}$  or higher.

## 2.4 Discussion and conclusion

We perform a statistical investigation based on the method presented in [Bartos et al. \(2017a\)](#) in order to assess, using only AGN positions and GW localization volumes, how many GW detections are needed to reject the no GW-AGN connection hypothesis. We find that the 13 O3 GW detections with expected  $z \leq 0.2$  are not enough to reject the no-connection hypothesis with either  $3\sigma$  or  $2\sigma$  significance. This result is obtained considering AGN with a number density  $n_{\text{AGN}} = 10^{-4.75} \text{Mpc}^{-3}$ . Nonetheless, Figure 2.3 shows that with the same number of detections, it is possible to reject the no-connection hypothesis for specific values of the AGN number density and of the fraction of GW events that originated inside an AGN. More precisely, the lower the AGN number density (i.e. the higher the luminosity of the considered AGN), the more likely it is to reject such a hypothesis with a given significance threshold. As far as O4 is concerned, the green line in Figure 2.2 shows that at least 21 detections associated with redshift  $z \leq 0.2$  will be needed to be able to reject the no-connection hypothesis between BBH mergers and AGN with  $n_{\text{AGN}} \geq 10^{-4.75} \text{Mpc}^{-3}$ . The number of expected detections of BBH mergers during O4 is  $79_{-44}^{+89}$  ([Abbott et al. 2020](#)). In our simulations of O4 detections, roughly 18.25% of the detected events correspond to  $z \leq 0.2$ . Our estimate is therefore that during O4,  $14_{-8}^{+17}$  BBH mergers will be associated with  $z \leq 0.2$ . As shown in Figure 2.2, 30 O4 closeby BBH detections would be enough to test values of  $f_{\text{agn}}$  higher than  $\approx 80\%$ , using AGN of any luminosity. The same degree of GW-AGN connection could be tested using a lower number of O4 detections in combination with the 13 closeby O3 detections.

We restrict our analysis to GW events with an expectation value for the redshift of  $z \leq 0.2$  for two different reasons. First, far GW events are typically associated with much larger localization volumes than the ones associated

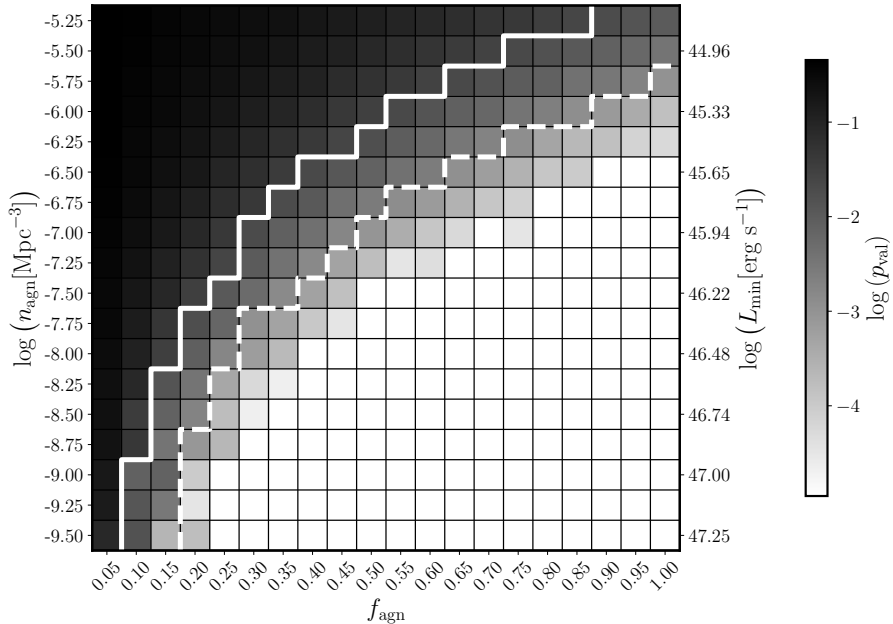


**Figure 2.3:** Significance of the rejection of the no-connection hypothesis as a function of the AGN number density ( $n_{\text{AGN}}$ ) and the fraction of GW events originated in an AGN ( $f_{\text{agn}}$ ). The p-values (and hence the significance) here represented refer to the detections of 13 events associated with  $z \leq 0.2$ . On the right of the dashed (solid) white line there is the region of the 2D parameter space in which the no-connection hypothesis can be rejected with a  $3\sigma$  ( $2\sigma$ ) significance. The p-values here represented are obtained from the comparison of the median of the  $\lambda_s$  distribution with respect to the  $\lambda_b$  distribution. Every value of  $\lambda_s$  has been calculated using Eq. (2.2) in a simulation in which a fraction  $f_{\text{agn}}$  of GWs come from an AGN. On the other hand, every value of  $\lambda_b$  comes from a simulation in which no GW event is originated in an AGN. On the right-hand axis, we report the logarithm of the minimum bolometric luminosity  $L_{\min}[\text{erg s}^{-1}]$  that has to be considered in the integration of the AGN LUMINOSITY FUNCTION at  $z = 0.1$  (Hopkins et al. 2007) to obtain the value of  $\log(n_{\text{AGN}}[\text{Mpc}^{-3}])$  indicated on the left-hand side of the grid.

with closer events. The inclusion of large GW localization volumes in our algorithm makes it too computationally demanding. The second reason is that for very luminous AGN in the local Universe, we expect to have high values of completeness in real AGN catalogues. These high values are needed in order to produce reliable results when applying the method described in this work to real, observed GW events and AGN. The incompleteness in observed AGN catalogues can be nonetheless taken into account with an appropriate rescaling of  $f_{\text{agn}}$  (Bartos et al. 2017a).

The main assumptions we made in this work were: considering spherical GW localization volumes, and neglecting redshift evolution for AGN and GW events as well as AGN clustering. We expect these assumptions not to remarkably impact on our final results. The BBH merger rate, the AGN number density, and the expected AGN-assisted merger rate do not significantly vary within the redshift range we consider (Hopkins et al. 2007; Yang et al. 2020; The LIGO Scientific Collaboration et al. 2021). Taking into consideration the real shape of GW events localization volumes and the clustering of AGN in the local Universe is important when performing a maximum likelihood estimation to find which value of  $f_{\text{agn}}$  best represents real observations. Such estimation is not the aim of this work but is currently being implemented in ongoing projects, in which the exploitation of realistic AGN catalogues and GW sky maps is required.

Our findings motivate more in-depth statistical investigations regarding the connection that may exist between GW events and luminous AGN in the local Universe. Such investigations, together with detailed physical models of mergers of compact objects in accretion disks of SMBHs might be able to unveil part of the mystery concerning the origin of BBH mergers.

## Acknowledgements

EMR acknowledges support from ERC Grant “VEGA P.”, number 101002511. RB is supported by the Italian Space Agency Grant “Phase A LISA mission activities”, Agreement No. 2017-29-H.0, CUP F62F17000290005. This material is based upon work supported by NSF’s LIGO Laboratory which is a major facility fully funded by the National Science Foundation. This research has made use of data or software obtained from the Gravitational Wave Open Science Center ([gw-openscience.org](http://gw-openscience.org)), a service of LIGO Laboratory, the LIGO Scientific Collaboration, the Virgo Collaboration, and KAGRA. LIGO Laboratory and Advanced LIGO are funded by the United States National Science Foundation (NSF) as well as the Science and Technology Facilities Council (STFC) of

the United Kingdom, the Max-Planck-Society (MPS), and the State of Niedersachsen/Germany for support of the construction of Advanced LIGO and construction and operation of the GEO600 detector. Additional support for Advanced LIGO was provided by the Australian Research Council. Virgo is funded, through the European Gravitational Observatory (EGO), by the French Centre National de Recherche Scientifique (CNRS), the Italian Istituto Nazionale di Fisica Nucleare (INFN) and the Dutch Nikhef, with contributions by institutions from Belgium, Germany, Greece, Hungary, Ireland, Japan, Monaco, Poland, Portugal, Spain. The construction and operation of KAGRA are funded by Ministry of Education, Culture, Sports, Science and Technology (MEXT), and Japan Society for the Promotion of Science (JSPS), National Research Foundation (NRF) and Ministry of Science and ICT (MSIT) in Korea, Academia Sinica (AS) and the Ministry of Science and Technology (MoST) in Taiwan.

*Software:* Numpy ([Harris et al. 2020](#)); Matplotlib ([Hunter 2007](#)); SciPy ([Virtanen et al. 2020](#)); K3Match ([Schellart 2013](#)); Astropy ([Astropy Collaboration et al. 2013, 2018](#)); BAYESTAR ([Singer & Price 2016](#)).

## Data Availability

The data underlying this article will be shared on reasonable request to the corresponding author.



# 3

## THE MOST LUMINOUS AGN DO NOT PRODUCE THE MAJORITY OF THE DETECTED STELLAR-MASS BLACK HOLE BINARY MERGERS IN THE LOCAL UNIVERSE

Work published in **N. Veronesi**, E. M. Rossi, S. van Velzen, 2023, *Monthly Notices of the Royal Astronomical Society*, 526, 6031. Reprinted here in its entirety.

### Abstract

#### 3.1 Introduction

The astrophysical mass spectrum of stellar-mass Black Holes (sMBHs) inferred from the results of the first three observing runs of Advanced LIGO ([LIGO Scientific Collaboration et al. 2015](#)) and Advanced Virgo ([Acernese et al. 2015](#)) extends also to masses between  $50 M_{\odot}$  and  $120 M_{\odot}$  ([The LIGO Scientific Collaboration et al. 2021](#)). This evidence challenges our current understanding of stellar evolution, since no remnant with a mass in that range is expected to be the final stage of the life of a single star ([Heger & Woosley 2002](#); [Belczynski et al. 2016](#)). Pair Instability Supernovae are expected to happen in that mass range, and are expected to leave no compact remnant, thus opening a gap in the black hole mass spectrum ([Woosley 2019](#); [Mapelli 2021](#)).

The detection of mergers of sMBHs within this mass gap can be interpreted as an evidence of binary formation channels beyond the “isolated stellar binary” channel (however, see also [de Mink & Mandel 2016](#); [Costa et al. 2021](#); [Tanikawa et al. 2021](#)). Other channels for Black Hole Binary (BBH) formation and merger involve dense dynamical environments, such as Globular Clusters ([Rodriguez et al. 2016](#); [Rodriguez & Loeb 2018](#); [Rodriguez et al. 2021](#)), Nu-

clear Star Clusters (Antonini et al. 2019; Kritos et al. 2022), and accretion discs around Supermassive Black Holes (SMBHs) in Active Galactic Nuclei (AGN) (Stone et al. 2017; Fabj et al. 2020; Ford & McKernan 2022; McKernan et al. 2022b; Li & Lai 2022, 2023a; ?). The formation of binaries with massive components in all these dense environments is facilitated by dynamical interactions such as exchanges in the case of three-body encounters. In the interaction between a binary system and a third object, the least massive of the three objects is expected to be scattered away from the binary system, that is tightened by this process (Hills & Fullerton 1980; Ziosi et al. 2014). In case the gravitational potential of the host environment is deep enough to retain the remnant of a BBH merger despite the post-merger recoil kick, this can take part in a subsequent merger (Gerosa & Berti 2019). Binaries that merge in this so-called hierarchical scenario (Yang et al. 2019; Barrera & Bartos 2022) are expected to show specific signatures in the mass and spin distributions of their components. Examples of these features are a low mass ratio, and isotropically oriented spins (Gerosa & Berti 2017; Gerosa & Fishbach 2021; Tagawa et al. 2021; Wang et al. 2021b; Fishbach et al. 2022; Li et al. 2022; Mahapatra et al. 2022).

What differentiates AGN from other dynamically dense potential hosts of BBH mergers, is the presence of a gaseous disc. Accretion discs around SMBHs are expected to contain compact objects (McKernan et al. 2012; Tagawa et al. 2020). The dynamical evolution of these objects is heavily influenced by the interaction with the gas of the disc. This interaction is expected to make the sMBHs migrate towards the innermost region of the AGN disk on timescales inversely proportional to their mass (McKernan et al. 2011; DeLaurentiis et al. 2023b). This migration should end when the net torque exerted by the gas on the migrating compact object is null. This is expected to happen at specific distances from the central SMBH, the so-called “migration traps” (Bellovary et al. 2016; Peng & Chen 2021; Grishin et al. 2024).

Due to the large localisation volumes associated to GW detections, the fractional contribution to the total merger rate of each individual binary formation channel is still unknown. The direct detection of an ElectroMagnetic (EM) counterpart of a BBH merger would be optimal to identify its host galaxy. The identification of candidate EM counterparts of mergers from AGN discs have been claimed (Graham et al. 2020, 2023, however, see also Ashton et al. 2021), and several works have investigated what should be the features of such counterparts (Palenzuela et al. 2010; Loeb 2016; Bartos 2016a; McKernan et al. 2019; Petrov et al. 2022). However, the current observational evidence based on EM counterparts is still not sufficient to constrain what fraction of the detected BBH mergers come from a specific channel.

Besides the search for EM counterparts, another method to investigate the contribution of a formation channel to the total detected merger rate is to infer how the distributions of the parameters of the merging binary should be for that specific formation path, and then compare these predictions to the data obtained by the LIGO and Virgo interferometers. This approach has been utilised in several previous works focused on the eccentricity of the binary (Romero-Shaw et al. 2021, 2022; Samsing et al. 2022), the components' spin orientation (Vajpeyi et al. 2022), the components' mass distribution (Gayathri et al. 2021, 2023; Belczynski et al. 2022; Stevenson & Clarke 2022), its redshift dependence (Karathanasis et al. 2022), and its relation with the distribution of the magnitude and the orientation of the spins (McKernan et al. 2020; Qin et al. 2022; Wang et al. 2022; Zevin & Bavera 2022). These works agree in saying that BBHs that merge in a dynamical environment tend to have higher masses involved, and more isotropically orientated spins. However, there is still no general agreement on the relative contributions to the total merger rate of all the possible formation channels.

Finally, a promising possibility to directly infer the fraction of the observed GW events that happened in a specific host environment is through the investigation of the spatial correlation between GW sky maps and the positions of such potential hosts. The statistical power of this approach has been investigated using simulated data, finding that it is possible to put constraints on the fraction of observed GW events that happened in an AGN, ( $f_{\text{AGN}}$ ), especially when rare (i.e. very luminous) potential sources are taken into account (Bartos et al. 2017a; Corley et al. 2019; Veronesi et al. 2022). These previous works used as main inputs the size of the 90 per cent Credibility Level localisation volume (further referred to as V90) of each GW observation and the number of AGN within it.

In this work we put for the first time upper limits on  $f_{\text{AGN}}$ , based on the observed GW-AGN spatial correlation in the case of high-luminosity AGN. These upper limits are obtained through the application of a statistical method that uses for the first time as input the exact position of every AGN. The likelihood function  $\mathcal{L}(f_{\text{AGN}})$  described in Section 3.3.1 takes also into account the incompleteness that characterizes the catalogue of potential hosts. We implement a likelihood maximization algorithm and check its performance on 3D Gaussian probability distributions as emulators of GW sky maps, and a mock catalogue of AGN. We then apply this method to check the spatial correlation between the objects of three all-sky catalogues of observed AGN and the 30 BBH mergers, with a 90% Credible Interval (CI) on the redshift posterior distribution fully contained within  $z = 0.3$ . Every AGN catalogue is characterized by a different

lower cut in bolometric luminosity.

This paper is organized as follows: in Section 3.2 we describe the properties of the observed all-sky AGN catalogues and of the detected GW events our statistical method is applied on. In the same section, we report how we generate the AGN mock catalogue and the Gaussian probability distributions necessary to test the likelihood performance. In Section 3.3 we describe in detail the analytical form of the likelihood function, how we test it on the mock AGN catalogue, and how we apply it to real data. In Section 3.4 we present the results of this application and the constraints on  $f_{\text{AGN}}$  it produces. Finally, in Section 3.5 we draw conclusions from these results and discuss how they can be improved and generalised in the near future.

We adopt the cosmological parameters of the Cosmic Microwave Background observations by Planck (Planck Collaboration et al. 2016):  $H_0 = (67.8 \pm 0.9) \text{ km s}^{-1}\text{Mpc}^{-1}$ ,  $\Omega_m = 0.308 \pm 0.012$ ,  $n_s = 0.968 \pm 0.006$ .

## 3.2 Datasets

In this section we first describe the selection criteria that we adopt to build the three all-sky catalogues of observed AGN, and we present the 30 detected GW events used when applying our statistical method to real data. We then describe the creation of the AGN mock catalogue and of the 3D Gaussian probability distributions used to validate our statistical method.

### 3.2.1 AGN catalogues

In order to construct our AGN catalogues, we start from the unWISE catalogue (Schlafly et al. 2019), which is based on the images from the WISE survey (Wright et al. 2010), and cross-match it with version 7.7b of the Milliquas catalogue (Flesch 2021). This Milliquas catalogue puts together all quasars from publications until October 2022, and contains a total of 2,970,254 objects. The cross-match is performed to associate a spectroscopic redshift measurement to as many unWISE objects as possible. We then select the objects with redshift estimates of  $z \leq 0.3$ . The reason in favour of restricting our analysis to  $z \leq 0.3$  is that the constraining power of our approach scales linearly with the completeness of the AGN catalogue that is used, and this redshift cut allows us to have an AGN completeness  $\gtrsim 0.5$ .

We then use the flux in the W1 band of the WISE survey to calculate the bolometric luminosity of every object and select only the ones brighter than the

luminosity threshold that characterizes each of the three catalogues we create. These thresholds are  $10^{45} \text{ erg s}^{-1}$ ,  $10^{45.5} \text{ erg s}^{-1}$ , and  $10^{46} \text{ erg s}^{-1}$ . Finally, we perform a color selection. We select objects with  $\text{mag(W1)} - \text{mag(W2)} \geq 0.8$ , where  $\text{mag(W1)}$  is the magnitude in the W1 band and  $\text{mag(W2)}$  is the magnitude in the W2 band. This is done to select objects based on their features related to thermal emission from hot dust, filtering out any contribution from the host galaxy to the AGN luminosity (Assef et al. 2013). Such a selection is has been proven to lead to a catalogue characterized by a reliability not smaller than 95 per cent (Stern et al. 2012). The resulting contamination fraction lower than 5 per cent is not expected to bias our results in a significant way. In the lowest luminosity threshold catalogue, this colour cut removes  $\approx 62$  per cent of all AGN, while this percentage drops to  $\approx 5$  per cent and  $\approx 2$  per cent for the  $10^{45.5} \text{ erg s}^{-1}$  and  $10^{46} \text{ erg s}^{-1}$  threshold catalogues, respectively. We are left with three catalogues containing 5,791, 1,412, and 242 AGN for the bolometric luminosity thresholds of  $10^{45} \text{ erg s}^{-1}$ ,  $10^{45.5} \text{ erg s}^{-1}$ , and  $10^{46} \text{ erg s}^{-1}$ , respectively. These three catalogues will be further referred to as CAT450, CAT455, and CAT460. The two catalogues characterized by the two highest luminosity thresholds are both subsamples of CAT450. Even if the AGN in the catalogues are not uniformly distributed in the sky (see Figure 3.1), they show no significant redshift-dependent incompleteness. This can be established by checking that the number of AGN ( $N_{\text{AGN}}$ ) in a specific bin of comoving distance ( $D_{\text{com}}$ ) is proportional to  $D_{\text{com}}^2$  up to the maximum redshift of the catalogues:  $z = 0.3$  (see Figure 3.2). A simple three-regions partition of the catalogues is used to identify areas with similar 2D sky-projected number density of AGN. For CAT455 we have that:

- 809 objects are within the footprint of the seventeenth data release of the Sloan Digital Sky Survey (SDSS) (York et al. 2000; Blanton et al. 2017; Abdurro’uf et al. 2022) (which corresponds approximately to 35.28 per cent of the sky). This is the most crowded region of the three, with a 2D number density of  $\approx 0.0556$  objects per square degree;
- 41 objects are characterized by a galactic latitude  $b$  with an absolute value smaller than  $10^\circ$  (approximately 17.36 per cent of the sky). In this region the Galactic plane of the Milky Way prevents observations from detecting most of the extra-galactic content, and is therefore the least crowded region of our catalogue, with 2D number density of  $\approx 0.0057$  objects per square degree;
- The remaining 562 objects populate the remaining 47.36 per cent of the

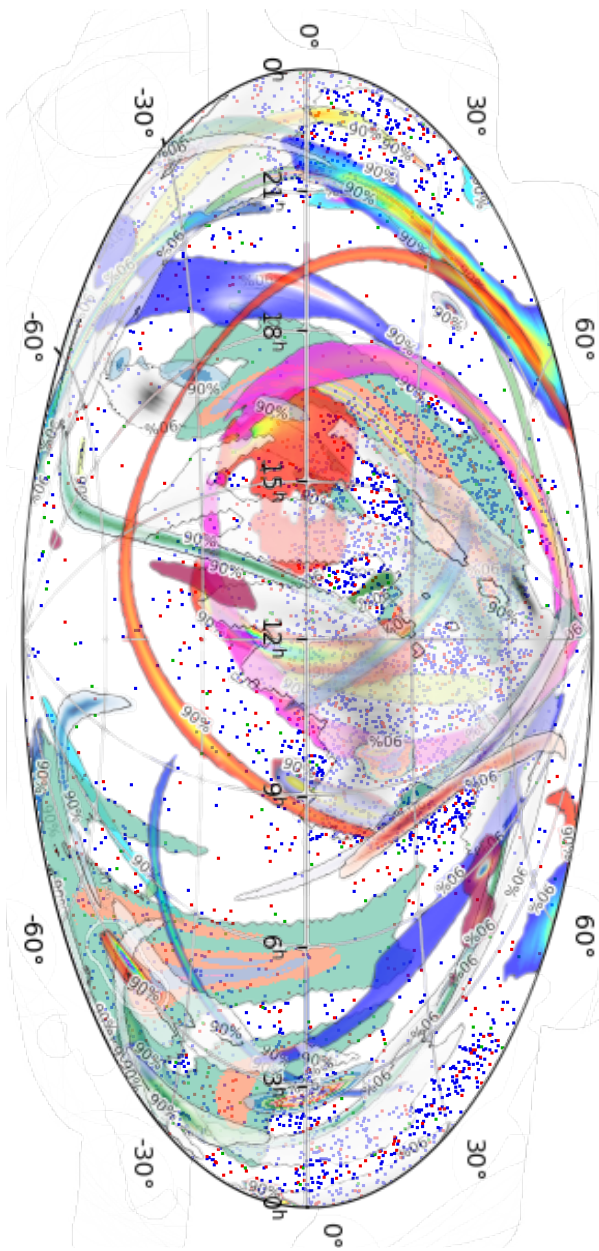


**Figure 3.1:** Positions of the AGN in CAT450 (blue dots), CAT455 (red dots), and CAT460 (green dots) described in Section 3.2.1, and 90 per cent CL localisation surfaces of the 30 detected BBH mergers listed in 3.2. These have a 90 per cent CI of the redshift posterior fully contained within  $z = 0.3$  (coloured regions). Regions with different colours correspond to different events. The sky map is visualized in equatorial coordinates.

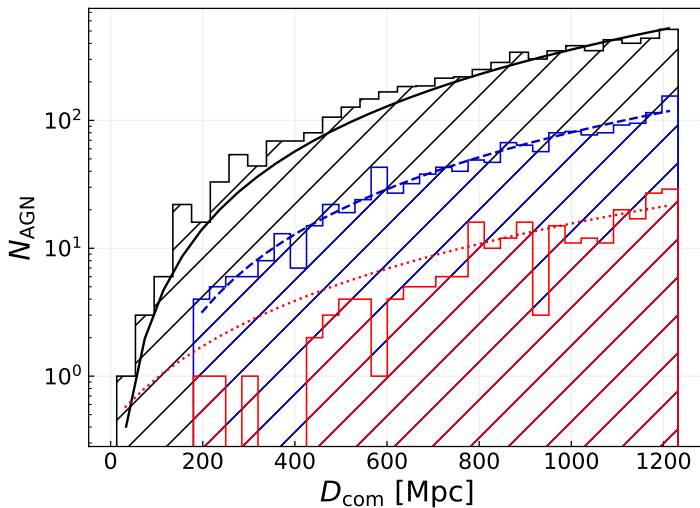


**Figure 3.2:** Number of AGN  $N_{\text{AGN}}$  in the catalogues presented in Section 3.2.1 as a function of comoving distance  $D_{\text{com}}$ . The black, blue, and red histograms refer to CAT450, CAT455, and CAT460, respectively. The black solid line, the blue dashed one, and the red dotted one show the best fit functions we obtain when fitting the number of objects per bin using the following form:  $N_{\text{AGN}} \propto D_{\text{com}}^2$ . These fits show no evidence of a significant redshift-dependent incompleteness of the catalogues. The apparent dearth of objects with  $D_{\text{com}} \leq 400$  Mpc in CAT460 can be explained in terms of a random statistical fluctuation with respect to the expectation value.

sky. The average 2D number density in this region is  $\approx 0.0288$  objects per square degree.

Because the AGN we consider and their host galaxies are relatively bright, many of them fall within the flux limit of the SDSS spectroscopic galaxy sample ([Strauss et al. 2002](#)), which has a completeness close to 100 per cent. In addition, the SDSS spectroscopic target selection ([Richards et al. 2002](#)) is tuned to target AGN or quasars below this flux limit. For this reason, the completeness of our catalogues in the SDSS footprint can be assumed to be close to 100 per cent. We calculate the incompleteness of the other two regions from the ratio of the projected 2D densities. Small deviations from unity for the completeness in the SDSS footprint are not expected to significantly change our final results. The same partition of the sky has been used to estimate the completeness of CAT450 and CAT460. The estimated completenesses, weighted over the area occupied by each region, are  $\approx 48$  per cent,  $\approx 61$  per cent, and  $\approx 87$  per cent for CAT450, CAT455, and CAT460, respectively.

We calculate the number densities of the AGN catalogues we create, correcting for their completeness. We obtain a completeness-corrected number density of  $1.53 \cdot 10^{-6} \text{Mpc}^{-3}$ ,  $2.93 \cdot 10^{-7} \text{Mpc}^{-3}$ , and  $3.54 \cdot 10^{-8} \text{Mpc}^{-3}$  for CAT450, CAT455, and CAT460, respectively. To illustrate the content of our catalogues, we show in Table 3.1 as an example the first ten entries of CAT450.

### 3.2.2 Detected Gravitational Wave events

When applying our statistical method to real data, we exploit the localisation volumes of 30 BBH mergers. These were detected during the first three observing runs of the LIGO and Virgo interferometers. We select those with the 90 per cent CI of the redshift posterior distribution within  $z = 0.3$  and false alarm rate below 1 per year. Our selected events are among the ones used in [The LIGO Scientific Collaboration et al. \(2021\)](#) to infer the parameters of the sMBH astrophysical population. These sky maps have been downloaded from the Gravitational Wave Open Science Center ([Abbott et al. 2021b](#)).

Table 3.2 lists these events. Among the parameters we report for each event, three are intrinsic properties of the binary. These are the masses of the two components of the binary, and the effective inspiral spin parameter. The latter is a weighted average of the projections of the two components' spins on the direction of the angular momentum of the binary (for a more detailed description of this parameter, see [Ajith et al. 2011; Abbott et al. 2023a; The LIGO Scientific Collaboration et al. 2021](#)). The other parameters reported for each detected GW

**Table 3.1:** First ten objects from our publicly available catalogue of AGN with a bolometric luminosity higher than  $10^{45} \text{ erg s}^{-1}$ , in ascending order of Right Ascension. For every object we indicate the original ID from the literature, the paper that first presented it, its unWISE ID, Right Ascension, Declination, redshift, the paper that first presented that redshift estimate, the magnitude in the W1 band, and the luminosity in the same band,  $L_{\text{W1}}$ . We calculate the bolometric luminosity multiplying  $L_{\text{W1}}$  by a bolometric correction factor, approximated to 10 for this band and in the luminosity range we consider (Hopkins et al. 2007). Out of the 5,791 objects in the catalogue, a total of 3,561 have a redshift measurement obtained from SDSS. In particular, 1,582 of these measurements are taken from Lyke et al. (2020), 1,025 from Ahumada et al. (2020), and 954 from Liu et al. (2019). The full catalogue will be made available on the journal website and at [https://github.com/niccoloveronesi/AGNallskycat\\_Veronesi23.git](https://github.com/niccoloveronesi/AGNallskycat_Veronesi23.git).

Name	Citation for Name	unWISE ID	R.A. [deg]	Dec. [deg]	$z$	Citation for $z$	$L_{\text{W1}}$ [ $\text{erg s}^{-1}$ ]
UVQSO00000.15-200427.7	Monroe et al. (2016)	0000hm197.00005716	0.00065	-20.07433	0.291	Monroe et al. (2016)	13.65 $2.72 \cdot 10^{44}$
SDSS J000005.49+310527.6	Ahumada et al. (2020)	0000jp31.860001234	0.02290	31.09102	0.286	Ahumada et al. (2020)	14.20 $1.58 \cdot 10^{44}$
PHL 2525	Lamontagne et al. (2000)	0000hm122.00001902	0.10172	-12.76328	0.200	Lamontagne et al. (2000)	11.04 $1.29 \cdot 10^{45}$
2MASX J0004028-0541012	Masci et al. (2010)	0000hm061.00015237	0.16774	-5.68361	0.094	Masci et al. (2010)	11.33 $1.90 \cdot 10^{44}$
RXS J00009+1723	Wei et al. (1999)	0000hp166.00024250	0.23319	17.39413	0.215	Wei et al. (1999)	12.93 $2.64 \cdot 10^{44}$
SDSS J000102.18-102326.9	Lyke et al. (2020)	0000hm107.00014745	0.25911	-10.39078	0.294	Lyke et al. (2020)	14.75 $1.01 \cdot 10^{44}$
RX J00013-0728	Tesch & Engels (2000)	0000hp075.00010333	0.32534	7.47432	0.270	Tesch & Engels (2000)	14.06 $1.57 \cdot 10^{44}$
PGC 929358	Paturel et al. (2003)	0000hm137.00004668	0.33219	-14.07310	0.087	Paturel & Sadler (2007)	11.65 $1.21 \cdot 10^{44}$
PGC 1698547	Paturel et al. (2003)	0000hp242.0009501	0.38474	24.04179	0.104	Ahumada et al. (2020)	11.72 $1.65 \cdot 10^{44}$
RX J00015+0529	Tesch & Engels (2000)	0000hp060.0003070	0.38896	5.48926	0.250	Ahumada et al. (2020)	12.67 $4.71 \cdot 10^{44}$

### 3.2. DATASETS

**Table 3.2:** List of the 30 BBH mergers detected during the first three observing runs of the LIGO and Virgo interferometers with a CI of the redshift posterior contained within  $z = 0.3$  and a false alarm rate below 1 per year. For every event, we report its ID, the mass of both the primary ( $m_1$ ) and the secondary ( $m_2$ ) component, the effective inspiral spin parameter  $\chi_{\text{eff}}$  (Ajith et al. 2011), the redshift, the SNR, and the value of V90. The last three columns correspond to the number of AGN inside V90, belonging to our three catalogues. We report the median and the 90 per cent credible intervals for the masses, the effective spin parameter, the redshift, and the SNR.

Event ID	$m_1$	$m_2$	$\chi_{\text{eff}}$	$z$	SNR	V90 [Mpc $^3$ ]	$\bar{N}_{\text{V90,CAT450}}$	$N_{\text{V90,CAT455}}$	$\bar{N}_{\text{V90,CAT460}}$
GW150914_095045	$34.6^{+4.4}_{-3.6}$	$30.0^{+2.9}_{-2.6}$	$-0.04^{+0.12}_{-0.10}$	$0.10^{+0.03}_{-0.03}$	$26.0^{+0.1}_{-0.1}$	$3.39^{+0.10}_{-0.06}$	3	0	0
GW151226_035853	$14.2^{+11.1}_{-10.6}$	$7.5^{+2.4}_{-2.8}$	$0.20^{+0.23}_{-0.19}$	$0.10^{+0.03}_{-0.03}$	$12.7^{+0.3}_{-0.4}$	$1.32^{+0.2}_{-0.17}$	10	1	0
GW170104_101158	$28.7^{+6.6}_{-4.2}$	$20.8^{+4.7}_{-4.7}$	$-0.04^{+0.15}_{-0.19}$	$0.22^{+0.07}_{-0.09}$	$13.8^{+0.2}_{-0.3}$	$1.42^{+0.2}_{-0.17}$	196	30	6
GW170608_020116	$10.6^{+4.0}_{-3.4}$	$7.8^{+2.7}_{-2.7}$	$0.05^{+0.13}_{-0.17}$	$0.07^{+0.03}_{-0.03}$	$15.3^{+0.2}_{-0.3}$	$2.98^{+0.2}_{-0.2}$	3	0	0
GW170809_082821	$34.1^{+8.0}_{-5.3}$	$24.2^{+4.8}_{-3.3}$	$0.07^{+0.17}_{-0.17}$	$0.21^{+0.05}_{-0.05}$	$12.8^{+0.4}_{-0.3}$	$4.21^{+0.2}_{-0.2}$	35	6	1
GW170814_103043	$30.9^{+3.9}_{-3.4}$	$24.9^{+3.0}_{-3.0}$	$0.08^{+0.12}_{-0.12}$	$0.13^{+0.03}_{-0.03}$	$17.7^{+0.2}_{-0.3}$	$2.96^{+0.2}_{-0.2}$	2	0	0
GW170818_022509	$34.8^{+6.6}_{-4.2}$	$27.6^{+4.1}_{-5.1}$	$-0.06^{+0.19}_{-0.22}$	$0.21^{+0.07}_{-0.07}$	$12.0^{+0.3}_{-0.3}$	$6.04^{+0.6}_{-0.6}$	3	1	0
GW190412_053044	$27.7^{+6.0}_{-5.0}$	$9.0^{+1.4}_{-1.4}$	$0.21^{+0.13}_{-0.13}$	$0.15^{+0.04}_{-0.04}$	$19.8^{+0.2}_{-0.3}$	$9.16^{+0.2}_{-0.2}$	20	3	0
GW190425_081805	$2.1^{+0.5}_{-0.4}$	$1.3^{+0.3}_{-0.2}$	$0.07^{+0.07}_{-0.07}$	$0.03^{+0.02}_{-0.01}$	$12.4^{+0.4}_{-0.4}$	$7.78^{+0.6}_{-0.6}$	9	1	0
GW190630_185205	$35.1^{+6.5}_{-5.5}$	$24.0^{+5.5}_{-5.2}$	$0.10^{+0.14}_{-0.13}$	$0.18^{+0.07}_{-0.07}$	$16.4^{+0.2}_{-0.2}$	$9.20^{+0.2}_{-0.2}$	148	33	4
GW190707_093226	$12.1^{+2.6}_{-2.5}$	$7.9^{+1.6}_{-1.6}$	$-0.04^{+0.09}_{-0.09}$	$0.17^{+0.06}_{-0.06}$	$13.1^{+0.2}_{-0.2}$	$1.23^{+0.2}_{-0.2}$	17	3	1
GW190708_232457	$19.8^{+4.3}_{-4.3}$	$11.6^{+2.1}_{-2.1}$	$0.05^{+0.10}_{-0.10}$	$0.19^{+0.07}_{-0.07}$	$13.4^{+0.2}_{-0.2}$	$1.02^{+0.1}_{-0.1}$	1560	305	43
GW190720_000836	$14.2^{+5.6}_{-3.3}$	$7.5^{+2.8}_{-1.8}$	$0.19^{+0.14}_{-0.14}$	$0.16^{+0.07}_{-0.07}$	$10.9^{+0.3}_{-0.3}$	$4.24^{+0.4}_{-0.4}$	20	7	1
GW190725_174728	$11.8^{+10.1}_{-9.1}$	$6.3^{+2.5}_{-2.5}$	$-0.04^{+0.36}_{-0.36}$	$0.20^{+0.05}_{-0.05}$	$9.1^{+0.4}_{-0.4}$	$3.81^{+0.8}_{-0.8}$	106	44	11
GW190728_064510	$12.5^{+6.9}_{-6.3}$	$8.0^{+2.6}_{-2.6}$	$0.13^{+0.19}_{-0.19}$	$0.18^{+0.05}_{-0.05}$	$13.1^{+0.3}_{-0.3}$	$3.88^{+0.7}_{-0.7}$	17	4	0
GW190814_211039	$23.3^{+1.4}_{-1.4}$	$2.6^{+0.1}_{-0.1}$	$0.00^{+0.07}_{-0.07}$	$0.05^{+0.01}_{-0.01}$	$25.3^{+0.1}_{-0.2}$	$3.55^{+0.1}_{-0.1}$	0	0	0
GW190917_033853	$9.7^{+3.4}_{-3.4}$	$2.1^{+1.1}_{-1.1}$	$-0.08^{+0.21}_{-0.13}$	$0.15^{+0.05}_{-0.05}$	$8.3^{+0.5}_{-0.5}$	$1.05^{+0.8}_{-0.8}$	60	22	3
GW190924_021846	$8.8^{+1.8}_{-1.8}$	$5.1^{+1.2}_{-1.2}$	$0.03^{+0.18}_{-0.18}$	$0.11^{+0.04}_{-0.04}$	$12.0^{+0.3}_{-0.4}$	$1.27^{+0.2}_{-0.2}$	13	1	0
GW190925_232845	$20.8^{+6.5}_{-5.9}$	$15.5^{+2.5}_{-3.6}$	$0.09^{+0.15}_{-0.15}$	$0.19^{+0.08}_{-0.08}$	$9.7^{+0.7}_{-0.6}$	$2.86^{+0.8}_{-0.8}$	401	94	12
GW190930_133541	$14.2^{+8.0}_{-6.0}$	$6.9^{+2.4}_{-2.1}$	$0.19^{+0.22}_{-0.22}$	$0.16^{+0.06}_{-0.06}$	$9.7^{+0.5}_{-0.5}$	$1.32^{+0.8}_{-0.8}$	63	13	2
GW19103_022549	$11.8^{+6.2}_{-5.2}$	$7.9^{+1.7}_{-1.7}$	$0.21^{+0.16}_{-0.16}$	$0.20^{+0.09}_{-0.09}$	$8.9^{+0.3}_{-0.3}$	$3.16^{+0.8}_{-0.8}$	255	62	8
GW191105_143512	$10.7^{+3.7}_{-3.6}$	$7.7^{+1.9}_{-1.9}$	$-0.02^{+0.13}_{-0.13}$	$0.23^{+0.09}_{-0.09}$	$9.7^{+0.3}_{-0.3}$	$1.53^{+0.8}_{-0.8}$	164	36	3
GW191129_134029	$10.7^{+4.1}_{-3.3}$	$6.7^{+1.7}_{-1.7}$	$0.06^{+0.16}_{-0.16}$	$0.16^{+0.05}_{-0.05}$	$13.1^{+0.2}_{-0.2}$	$5.92^{+0.7}_{-0.7}$	101	20	2
GW191204_171526	$11.9^{+3.3}_{-3.3}$	$8.2^{+1.4}_{-1.4}$	$0.16^{+0.08}_{-0.08}$	$0.13^{+0.05}_{-0.05}$	$17.5^{+0.2}_{-0.2}$	$1.24^{+0.2}_{-0.2}$	12	1	0
GW191216_213338	$12.1^{+4.6}_{-2.3}$	$7.7^{+1.6}_{-1.6}$	$0.11^{+0.13}_{-0.13}$	$0.07^{+0.02}_{-0.02}$	$18.6^{+0.2}_{-0.2}$	$3.66^{+0.6}_{-0.6}$	2	2	0
GW200115_042309	$5.9^{+2.0}_{-2.0}$	$1.44^{+0.85}_{-0.85}$	$-0.15^{+0.24}_{-0.24}$	$0.06^{+0.03}_{-0.03}$	$11.3^{+0.5}_{-0.5}$	$3.79^{+0.6}_{-0.6}$	3	2	0
GW200129_065458	$34.5^{+3.2}_{-3.2}$	$28.9^{+3.4}_{-9.3}$	$0.11^{+0.14}_{-0.14}$	$0.18^{+0.05}_{-0.05}$	$26.8^{+0.2}_{-0.2}$	$7.06^{+1.0}_{-1.0}$	7	0	0
GW200202_153413	$10.1^{+3.3}_{-6.4}$	$7.3^{+1.1}_{-1.1}$	$0.04^{+0.13}_{-0.13}$	$0.09^{+0.03}_{-0.03}$	$10.8^{+0.4}_{-0.4}$	$2.32^{+0.6}_{-0.6}$	2	0	0
GW200311_115853	$34.2^{+3.8}_{-3.8}$	$27.7^{+1.7}_{-1.7}$	$-0.02^{+0.06}_{-0.06}$	$0.23^{+0.05}_{-0.05}$	$17.8^{+0.2}_{-0.2}$	$5.94^{+1.0}_{-1.0}$	7	2	0
GW200316_215756	$13.1^{+10.8}_{-2.9}$	$7.8^{+1.9}_{-2.9}$	$0.13^{+0.10}_{-0.10}$	$0.22^{+0.08}_{-0.08}$	$10.3^{+0.7}_{-0.7}$	$9.22^{+1.0}_{-1.0}$	12	5	0

event in Table 3.2 are the redshift, the SNR, V90, and the number of AGN from our all-sky observed catalogues that are inside V90. The 90 per cent CL sky regions of the same BBH mergers that are listed in Table 3.2 are displayed in Figure 3.1.

### 3.2.3 AGN mock catalogue

We test our statistical method explained below on an AGN mock catalogue characterized by a non-uniform incompleteness. In order to create it, we first have to construct a *complete* parent mock catalogue, where we assume that all AGN are accounted for. These are uniformly distributed in comoving volume between  $z = 0.0$  and  $z = 0.4$  with a number density of  $n_{\text{AGN}} = 10^{-7} \text{Mpc}^{-3}$ . The non-uniform *incomplete* catalogue is a sub-sample of this complete one. Non-uniform incompleteness is a feature present also in the observed AGN catalogues exploited in this paper (see section 3.2.1). The incomplete mock catalogue is created by dividing the complete one in three different regions, and sub-sampling each of them in a different way as follows:

- The first region has galactic coordinate  $b$  bigger than  $30^\circ$ . This corresponds to 25 per cent of the sky. In this first region no sub-sampling has been performed, hence its completeness is 100 per cent;
- The second region has  $b$  between  $-30^\circ$  and  $30^\circ$ . This corresponds to 50 per cent of the sky. In this second region, we remove 30 per cent of the objects from the parent complete catalogue, hence the completeness in this region is 70 per cent.
- The third region has Galactic coordinate  $b$  smaller than  $-30^\circ$ . This corresponds to the remaining 25 per cent of the sky. Here we removed the 70 per cent of the objects from the complete catalogue, so the completeness of this region is 30 per cent.

The incomplete mock catalogue has a total of 1,160 objects, and a weighted average completeness of 67.5 per cent.

### 3.2.4 Simulated Gravitational Wave sky maps

The sky maps of our simulated GW events are described for simplicity as 3D Gaussian probability distributions. These distributions are created such that the size of their 90 per cent Credibility Level volume is the same as the size

of an actual V90 simulated with the same source parameters, assuming the O3 configuration of the LIGO and Virgo detectors. For these simulated events we assume a Black Hole mass distribution that follows the POWER LAW + PEAK model described in [The LIGO Scientific Collaboration et al. \(2021\)](#). For simplicity the spins of the components of the binaries are assumed to be aligned with the binary angular momentum, with a magnitude uniformly distributed between 0 and 1. This choice does not bias our analysis. This is because assuming aligned spins leads to distributions of V90 consistent with the observed one ([Veronesi et al. 2022](#)). The size of V90 is the only parameter of the simulated BBH merger detections that enters the analysis presented in this paper, together with the spatial position. The inclination  $\iota$  of the binaries is sampled from a uniform distribution in  $\arccos \iota$ . Once we have sampled the distributions of all the parameters of the merging BBH (masses and spins of the components, position of the merger and inclination of the binary), we model its GW signal with an IMRPhenomD waveform type ([Husa et al. 2016; Khan et al. 2016](#)). We then simulate the detection of this signal with a network composed of three interferometers: LIGO Hanford, LIGO Livingston, and Virgo. The sensitivity curves we use for these three detectors are the ones correspondent to the following IDs: ALIGOMIDLOWSENSITIVITYP1200087 for the LIGO interferometers, and ADVMIDLOWSENSITIVITYP1200087 for Virgo. The duty cycle indicates for what fraction of the total observing time each of the detectors is online. To all detectors, we assign the average value of the duty cycles that characterized the third observing run of LIGO and Virgo: 0.78 ([Abbott et al. 2021a, 2023a](#)). We keep a Signal to Noise Ratio (SNR) detection threshold of 8 for the network, and require  $\text{SNR} \geq 4$  for at least two of the three detectors. This cut leads to a realistic distribution of V90 ([Veronesi et al. 2022](#)), allowing us to circumvent the need to calculate the detection confidence level, according to the LIGO-Virgo-KAGRA collaboration criteria.<sup>1</sup> We finally measure V90 for every simulated detection using the BAYESTAR algorithm ([Singer & Price 2016](#)). The sensitivity curves used to create these simulated detections and the value chosen for the duty cycles aim to reproduce the network that performed real detections during the third observing run of the LIGO and Virgo interferometers (O3). However, we apply the method these simulations are used to test also to GW events detected before O3. This does not introduce any bias in the testing strategy described in Section 3.3.2, because there is no V90 from the first and second observing runs which is smaller (bigger) than the smallest

---

<sup>1</sup>These are based on the False Alarm Rate or the probability of being of astronomical origin,  $p_{\text{astro}}$  ([Abbott et al. 2021a, 2023a](#)).

(biggest) one from O3 (see Table 3.2).

To each simulated detection we therefore associate a value of V90. We call R90 the radius of a sphere of volume V90. The 3D spherically symmetric Gaussian distributions we use as mock GW sky maps are combinations of three 1D Gaussian distributions with equal standard deviation. For every value of R90, we calculate the standard deviation each of the 1D distributions must have in order for the 90 per cent credibility contour of the 3D Gaussian distribution to be a spherical surface of radius R90.

Knowing the exact position of each GW event we simulate, we can then sample the coordinates of the centre of the correspondent mock sky map from a Gaussian distribution centered on it. The standard deviation of such Gaussian is calculated from the value of R90 associated to the simulated BBH merger.

The sample of mock sky maps for the testing of our statistical method is therefore represented by 3D Gaussian distributions characterized by the positions of their centres and the radii of their 90 per cent credibility level regions (R90). The test strategy described in detail later in Section 3.3.2 is independent on the shape of the sky maps used during the cross match with mock AGN catalogues. For this reason, the choice of using a 3D Gaussian distribution does not lead to any bias in the obtained results concerning the test of the validity of the statistical method.

## 3.3 Method

### 3.3.1 Likelihood function

Our statistical framework compares two scenarios. In the first scenario AGN are physically associated to BBH mergers, while in the second one, AGN are background sources, i.e, their presence inside the the localisation volume of a GW event is coincidental.

The general analytical form of the likelihood function used in this work is based on the one described in [Braun et al. \(2008\)](#) and first used to draw conclusions on the detectability of a GW-AGN connection by [Bartos et al. \(2017a\)](#).

This can be written as follows:

$$\begin{aligned}\mathcal{L}(f_{\text{AGN}}) &= \prod_{i=1}^{N_{\text{GW}}} \mathcal{L}_i(f_{\text{AGN}}) \\ &= \prod_{i=1}^{N_{\text{GW}}} [c \cdot 0.9 \cdot f_{\text{AGN}} \cdot \mathcal{S}_i + (1 - c \cdot 0.90 \cdot f_{\text{AGN}}) \mathcal{B}_i] ,\end{aligned}\quad (3.1)$$

where  $\mathcal{L}_i$  is the single-event likelihood associated to the  $i$ -th GW event,  $f_{\text{AGN}}$  is the fraction of GW events that originate from an AGN,  $N_{\text{GW}}$  is the total number of GW events,  $c$  is the average <sup>2</sup> completeness of the AGN catalogue, and  $\mathcal{S}_i$  ( $\mathcal{B}_i$ ) is the signal (background) probability density function. If the value of  $\mathcal{S}_i$  is bigger than the value of  $\mathcal{B}_i$ ,  $\mathcal{L}_i(f_{\text{AGN}})$  will peak at the maximum allowed value of its parameter:  $f_{\text{AGN}} = 1$ , meaning that the  $i$ -th GW event is likely physically associated to one of the AGN that are inside its localisation volume. The opposite is true if the value of  $\mathcal{B}_i$  is bigger than the value of  $\mathcal{S}_i$ . The product of all the single-event likelihoods is then what determines the degree of GW-AGN association through the value of  $f_{\text{AGN}}$  corresponding to its maximum. The 0.9 pre-factor in front of  $f_{\text{AGN}}$  is used to take into account that the localisation volumes we use are associated to a confidence level of 90 per cent. The introduction of the  $c$  factor is a novelty with respect to previous similar works that used only complete mock AGN catalogues (Bartos et al. 2017a; Corley et al. 2019; Veronesi et al. 2022). If such a term was not present when using incomplete catalogues, the likelihood function would on average peak at a lower value of  $f_{\text{AGN}}$  with respect to the true one. This would happen because, even if a physical association exists, it might not be detected if the AGN host of a GW event is not present in the catalogue. The  $c$  factor in Equation 3.1 corrects for this potential bias. Previous studies used as main input the size of each GW event's V90 and the number of AGN within it ( $N_{\text{V90}}$ ). In this work, we additionally exploit the information embedded in the exact position of every AGN within the localisation volume: i.e., the value of the 3D GW localisation probability density function at the AGN position. We therefore write the signal probability density function for the  $i$ -th GW as:

$$\mathcal{S}_i = \frac{\sum_{j=1}^{N_{\text{V90}_i}} p_j}{n_{\text{AGN}} V90_i} ,\quad (3.2)$$

---

<sup>2</sup>As we mention later on, we tested that working with an average incompleteness over the whole catalogue gives indistinguishable (correct) results with respect to accounting for a position-dependent incompleteness.

where  $n_{\text{AGN}}$  is the average number density of AGN in the catalogue, and  $p_j$  is the probability density associated to the position of the  $j$ -th AGN. The denominator in Equation 3.2 represents the expected number of AGN from a catalogue of number density  $n_{\text{AGN}}$  that are contained in a region of size  $V90_i$ . Therefore, the signal probability density function represents the total probability density associated to the positions of all the AGN within  $V90_i$ , normalized by their expected number. The more objects there are within  $V90_i$  and/or the more clustered they are towards the peak of the probability density distribution, the higher the value of  $\mathcal{S}_i$  is. This is in accord with the fact that  $\mathcal{S}_i$  in Equation 3.2 describes how likely the scenario in which AGN are physically associated to BBH mergers is. On the other hand, the probability density function associated to the scenario where AGN are background sources, accidentally present in GW localisation volumes, can be expressed with a flat probability for an AGN to be found anywhere in  $V90$ :

$$\mathcal{B}_i = \frac{0.9}{V90_i} , \quad (3.3)$$

where the 0.9 term at the numerator guarantees that  $\mathcal{S}_i$  and  $\mathcal{B}_i$  are normalized to the same value. From Equations 3.2 and 3.3 it follows that the likelihood function in Equation 3.1 is dimensionful with units of one over volume. This means that for it to be turned into a probability density function, it should be normalized dividing it by its integral over the whole [0,1] range of  $f_{\text{AGN}}$ . During the testing of the statistical method on mock data and its application to real GW detections and AGN catalogues the non-normalized version of the likelihood function is usually computed, unless specified otherwise. In particular we normalize this function when extracting the posterior distribution on  $f_{\text{AGN}}$ .

In our statistical analysis the prior on  $f_{\text{AGN}}$  is assumed to be uniform between 0 and 1.

### 3.3.2 Test on mock data

To test the performance of the likelihood we use data coming from the cross-match between the incomplete AGN mock catalogue described in Section 3.2.3 and the mock GW detections described in Section 3.2.4.

This test consists of a Monte Carlo simulation of 1,000 realizations. Every realization is characterized by the same total number of simulated detected BBH mergers. This number of detections is the same one used during the application to real data:  $N_{\text{GW}} = 30$ . At the start of each realization, we draw a value from the prior distribution of  $f_{\text{AGN}}$ . This represents the true value of this parameter for the specific realization, and will be further referred to as  $f_{\text{AGN},\text{true}}$ . We

then sample a binomial distribution characterized by the parameters  $n = N_{\text{GW}}$  and  $p = f_{\text{AGN},\text{true}}$  to obtain the number of simulated detected GWs that come from an AGN of the complete mock catalogue presented in Section 3.2.3 within  $z = 0.2$ . The remaining events of the  $N_{\text{GW}}$  simulated detections are the ones coming from a position randomly sampled from a uniform distribution in the same redshift range. The redshift cut on the potential sources of both the signal and the background events is performed to be sure that the entirety of V90 is within the volume of the mock AGN catalogue. This is necessary to avoid any boundary-related underestimation of  $\mathcal{S}_i$  during the cross-match of these localisation volumes with the incomplete AGN mock catalogue.

We cross-match the 3D Gaussian distributions representing the sky maps of the 30 GW events with the incomplete AGN mock catalogue and calculate the value of the likelihood as a function of  $f_{\text{AGN}}$  using Equations 3.1, 3.2, and 3.3. We then compute the normalized posterior distribution on  $f_{\text{AGN}}$ :  $\mathcal{P}(f_{\text{AGN}})$ . Finally, we calculate the Credibility Level (CL) of  $f_{\text{AGN},\text{true}}$  and the corresponding Credibility Interval (CI). The CI is defined as the range of  $f_{\text{AGN}}$  that is associated to values of the posterior equal or greater than  $\mathcal{P}(f_{\text{AGN},\text{true}})$ . We say for example that  $f_{\text{AGN},\text{true}}$  has a CL of 90 per cent if the integral of  $\mathcal{P}(f_{\text{AGN}})$  evaluated over the corresponding CI is 0.9.

The blue line in the Probability-Probability plot presented in Figure 3.3 shows the cumulative distribution of the 1,000 values of CLs associated to  $f_{\text{AGN},\text{true}}$  from all the realizations. The grey lines show the cumulative distribution of 100 uniform samples between 0 and 1. Since the distribution of the CLs associated to  $f_{\text{AGN},\text{true}}$  is statistically indistinguishable from a uniform one, we can conclude that our statistical method is able to produce trustworthy results when tested on mock data. Therefore, maximizing the likelihood described in Equations 3.1, 3.2 and 3.3 leads to an accurate estimate of  $f_{\text{AGN}}$ .

Finally, we test that our results do not change if we use in Equation 3.1 the actual value of the catalogue completeness ( $c$ ) in each localisation volume. More specifically, this individual completeness is calculated as a weighted average of the completeness of the AGN catalogue in the 3D region occupied by each V90. Our test yields indistinguishable results, therefore, for simplicity, we only present the ones computed using the average catalogue completeness.

### 3.3.3 Application to real data

Once we have tested the accuracy of the statistical method, we apply it to real data. We cross-match the skymaps of the 30 detected BBH mergers presented in 3.2.2, and listed in Table 3.2 with the all-sky AGN catalogues described in

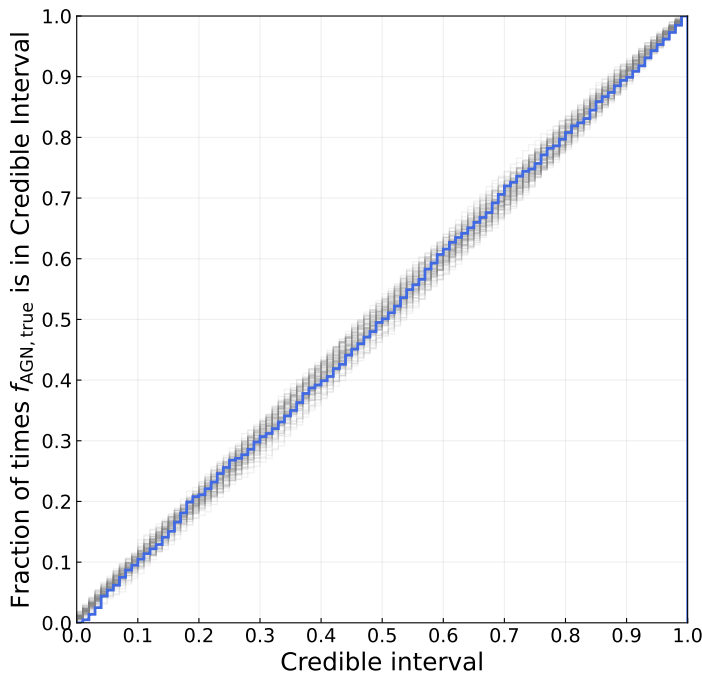


**Figure 3.3:** Fraction of times  $f_{\text{AGN},\text{true}}$  lies within a certain Credible Interval as a function of the credibility level of such an interval. The blue line shows the result obtained by testing the likelihood function described in Section 3.3.1 on mock data. The gray lines show the cumulative distributions of 100 samples of a uniform distribution in the  $[0,1]$  range.

Section 3.2.1. We then calculate  $\mathcal{L}(f_{\text{AGN}})$  using Equations 3.1, 3.2, and 3.3.

In the case of CAT455 and CAT460 the combination of the data coming from the cross-match with the 30 GW events leads to a monotonically decreasing likelihood, as a function of  $f_{\text{AGN}}$ . We therefore decide to evaluate upper limits on this parameter integrating the normalized likelihood between  $f_{\text{AGN}} = 0$  and  $f_{\text{AGN}} = 1$ . Since the prior is assumed to be uniform, through this integration we obtain the cumulative posterior distribution on  $f_{\text{AGN}}$ .

The same process has been followed also for CAT450, even if in this case the likelihood turns out to be rather insensitive to  $f_{\text{AGN}}$ . Specifically, in this last case, the posterior is prior-dominated: data do not allow us to put much tighter constraints on  $f_{\text{AGN}}$  than the ones imposed by the flat prior only. This is caused by the high number of objects contained in the AGN catalogue (Veronesi et al. 2022), combined with the non-negligible level of incompleteness that characterizes the same catalogue. We therefore decide not to repeat the analysis with an AGN catalogue characterized by a lower luminosity threshold. Such a catalogue would likely also show redshift-dependent completeness, which will have to be taken into account in future works aimed to explore the relation between BBH mergers and lower-luminosities AGN. A meaningful exploitation of AGN catalogues denser than the ones used in this work will be possible only when we will have data from more and/or better localized BBH mergers.

## 3.4 Results

The cumulative posterior distributions over  $f_{\text{AGN}}$  we obtain through the application of our statistical method to observed data are shown in Figure 3.4. The black solid line shows the posterior distribution in the case of the cross-match of the observed GW events with CAT460, while the dashed (dotted) line shows it in the case of a CAT455 (CAT450). On the vertical axis there is the probability for the true value of  $f_{\text{AGN}}$  being smaller than the correspondent value on the horizontal axis. As an example, the solid blue line shows that the upper limit of the 95 per cent credibility interval is  $f_{\text{AGN}} = 0.17$  in the case of the cross-match with CAT460. Figure 3.5 shows a region of the two-dimensional parameter space that has been investigated in this work. On the vertical axis one can read the thresholds in bolometric luminosities of AGN on the left-hand side, and the correspondent values of number densities on the right-hand side. The three number densities correspondent to the three luminosity thresholds we use to create CAT450, CAT455, and CAT460 have been calculated taking into account their estimated completeness. For each of these completeness-corrected

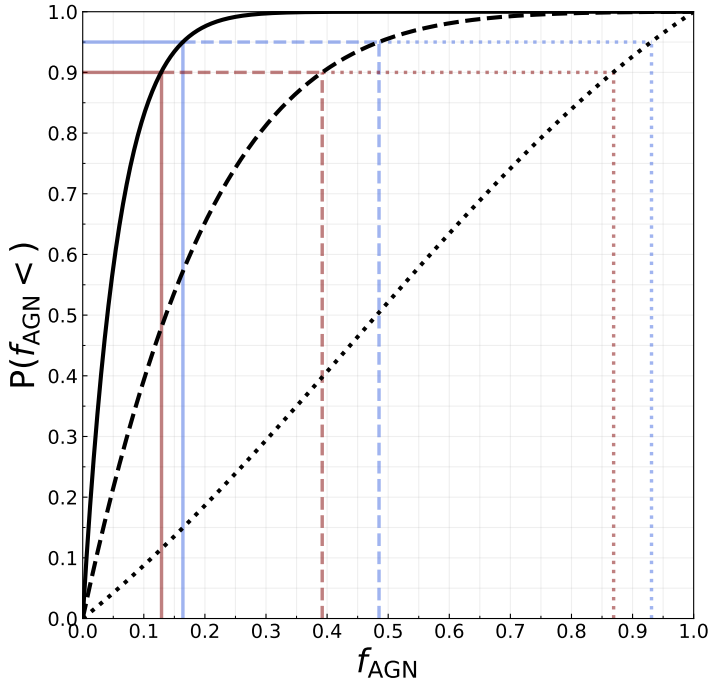


**Figure 3.4:** Black solid line: Cumulative posterior distribution for the fraction of detected GWs originated in an AGN ( $f_{\text{AGN}}$ ) with a bolometric luminosity higher than  $10^{46} \text{ erg s}^{-1}$ . Every value on the vertical axis corresponds to the probability associated to the true value of  $f_{\text{AGN}}$  being smaller than the correspondent value on the horizontal axis. The dashed (dotted) line shows the posterior distribution obtained using a luminosity threshold of  $10^{45.5} \text{ erg s}^{-1}$  ( $10^{45} \text{ erg s}^{-1}$ ). The maroon lines indicate that the upper limit of the 90 per cent credibility interval corresponds to  $f_{\text{AGN}} = 0.13$  for the  $10^{46} \text{ erg s}^{-1}$  luminosity cut, to  $f_{\text{AGN}} = 0.40$  for the  $10^{45.5} \text{ erg s}^{-1}$  luminosity cut, and to  $f_{\text{AGN}} = 0.87$  for the  $10^{45} \text{ erg s}^{-1}$  luminosity cut. The blue lines indicate that the upper limit of the 95 per cent credibility interval corresponds to  $f_{\text{AGN}} = 0.17$  for the  $10^{46} \text{ erg s}^{-1}$  luminosity cut, to  $f_{\text{AGN}} = 0.49$  for the  $10^{45.5} \text{ erg s}^{-1}$  luminosity cut, and to  $f_{\text{AGN}} = 0.94$  for the  $10^{45} \text{ erg s}^{-1}$  luminosity cut.

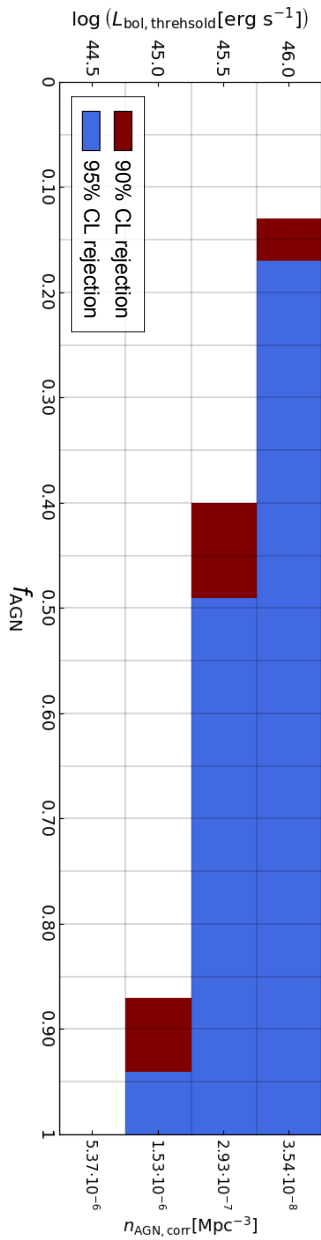


**Figure 3.5:** Rejected regions at 90 and 95 per cent credibility level of the two-dimensional parameter space  $\{L_{\text{bol}}, f_{\text{AGN}}\}$  investigated in this work. The bolometric luminosity threshold for the observed AGN is indicated on the vertical axis on the left-hand side, while the fraction of detected BBH mergers that come from AGN brighter than those thresholds is on the horizontal axis. The maroon (blue) regions are the ones that the analysis presented in this work rejects with a 90 (95) per cent credibility. The right vertical axis shows the number density obtained from the Hopkins et al. (2007) luminosity function, normalized to match the completeness-corrected number density of our catalogue.

number densities we calculate their ratio with respect to the number density obtained integrating in the same luminosity range the best-fit AGN luminosity function at  $z = 0.1$  presented in Hopkins et al. (2007). The mean of this ratios, together with the number density estimated from Hopkins et al. (2007) for a bolometric luminosity threshold of  $10^{44.5} \text{ erg s}^{-1}$ , has been used to calculate the completeness-corrected number density for such a luminosity cut. All the possible values of  $f_{\text{AGN}}$  are on the horizontal axis. The maroon (blue) region is the part of the parameter space that we reject with a 90 (95) per cent credibility level.

In The LIGO Scientific Collaboration et al. (2021) the total BBH merger rate per comoving volume has been parametrized as a power law as a function of redshift:  $\mathcal{R}(z) \propto (1+z)^\kappa$ . The value of the spectral index has been estimated to be  $\kappa = 2.7_{-1.9}^{+1.8}$ , and the best measurement of the merger rate  $\mathcal{R}$  occurs at  $z \approx 0.2$ :  $\mathcal{R}(z = 0.2) \leq 41 \text{ Gpc}^{-3} \text{ yr}^{-1}$  at 90 per cent credibility. Combining this result with the upper limit of  $f_{\text{AGN}} \leq 0.49$  ( $f_{\text{AGN}} \leq 0.17$ ) obtained in this work, we find that the 95 per cent credibility upper limit on the rate of BBHs merging in AGN brighter than  $10^{45.5} \text{ erg s}^{-1}$  ( $10^{46} \text{ erg s}^{-1}$ ) is  $\mathcal{R}_{\text{AGN}}(z = 0.2) \simeq 20 \text{ Gpc}^{-3} \text{ yr}^{-1}$  ( $\mathcal{R}_{\text{AGN}}(z = 0.2) \simeq 7 \text{ Gpc}^{-3} \text{ yr}^{-1}$ ) at  $z \approx 0.2$ . It is important to remember that these results have been obtained assuming 100 per cent completeness in the SDSS footprint in our catalogues of luminous, redshift selected AGN. However, small variations over this assumption are not expected to produce qualitatively different results with respect to the ones presented in this section, since they scale linearly with the AGN catalogue completeness (see Equation 3.1).

### 3.5 Discussion and conclusion

We present a likelihood-based method to constrain the fractional contribution of the AGN channel to the observed merger rate of BBHs. In particular we compare the scenario in which AGN are physically associated to BBH mergers to the one in which the presence of AGN in localisation volumes of GW events is only due by chance. We use as input data the size of each GW localisation volume and the exact position of all the AGN that are in it. We calculate the posterior distribution of the fraction of the detected GW events that come from an AGN,  $f_{\text{AGN}}$ . We then put observational constraints on this parameter by determining the upper limits associated to the 90 and 95 per cent CIs of the posterior distribution.

We first validate this method on a mock AGN catalogue characterized by a non-uniform completeness (see Figure 3.3).

We then apply the same statistical analysis to observed data. We use the sky maps of the 30 BBH mergers detected by the LIGO and Virgo interferometers characterized by a 90 per cent C.I. of the redshift distribution entirely contained within  $z = 0.3$ . We cross-match these sky maps with three all-sky catalogues of AGN we create starting from cross-matching the unWISE catalogue (Schlafly et al. 2019) with the Milliquas one (Flesch 2021). We select only the objects with a spectroscopic measurement of redshift correspondent to  $z \leq 0.3$  and with a bolometric luminosity higher than  $10^{45} \text{ erg s}^{-1}$ ,  $10^{45.5} \text{ erg s}^{-1}$ , and  $10^{46} \text{ erg s}^{-1}$ . We calculate the posterior cumulative distribution on  $f_{\text{AGN}}$  and conclude that in the case of the two highest luminosity thresholds we can put upper limits on this parameter that are tighter with respect to the ones one can obtain from the sole assumption of a uniform prior between 0 and 1. In the case of the cross-match with the AGN catalogue characterized by the highest (intermediate) luminosity threshold we find that  $f_{\text{AGN}} = 0.17$  ( $f_{\text{AGN}} = 0.49$ ) is the upper limit of the 95 per cent credibility interval. Figure 3.4 shows the entire cumulative posterior distributions, while Figure 3.5 shows more explicitly which parts of the two-dimensional AGN luminosity- $f_{\text{AGN}}$  parameter space are rejected with a 90 and a 95 per cent credibility. Previous works used only simulated GW data and mock AGN catalogues to draw conclusions about the possibility of exploring the spatial correlation between the two. Instead, we present the first constraints on  $f_{\text{AGN}}$  based on observational data only. Moreover, in the previous analyses the number of potential hosts within the V90 of every GW event was used as the main source of information, together with the size of V90. As mentioned above, the likelihood function we present in this work also takes into account for the first time the exact position of every AGN within V90 and the overall completeness of the AGN catalogue. The results obtained in this work are observational upper limits on the correlation between the detected BBH mergers and the high luminosity, and spectroscopically selected AGN that are in the catalogues described in Section 3.2.1. They can be used in the future to inform theoretical models of compact binary objects in AGN discs. Such results hint towards the conclusion that physical conditions of the gas and the stars in the discs of high-luminosity AGN are not sufficiently able to drive the formation and the merger of binaries of sMBHs in order to be major contributors to the total merger rate. This conclusion would be in agreement with the recent theoretical result obtained by Grishin et al. (2024), where it is stated that migration traps in AGN discs are not expected to be present in the case of a bolometric luminosity higher than  $10^{45} \text{ erg s}^{-1}$  for an AGN alpha viscosity parameter of  $\alpha = 0.01$ . Their inability to create migration traps would explain why AGN characterized by a luminosity higher than such a threshold are not to be considered potential

preferred hosts of BBH mergers.

One way for generalizing the results presented in this paper is the creation of a more complete all-sky AGN catalogue. The introduction of objects with only a photometric measurement of the redshift is a possible method of doing that. This would increase the number density of the catalogue, but will also increase the probability of considering objects that have been erroneously identified as AGN. This confidence on the classification of each object will have to be taken into account in the expression of the likelihood function.

The results concerning the posterior distributions shown in Figure 3.4 are relative to the fraction of BBH mergers that have happened in an AGN with a bolometric luminosity higher than the three thresholds we have considered. We perform this luminosity cuts in order to be sure to have a good level of completeness in our observed AGN catalogues. In order to draw general conclusion on the AGN formation channel for BBHs, future works will investigate the correlation between GW events and AGN in a broader range of luminosities. Such an investigation will have to take into consideration the fact that low values of completeness and its dependence on redshift lower the statistical power of the method, increasing the uncertainty on the predictions.

The analysis described in this paper is restricted to BBH mergers whose host environment is expected to be at  $z \leq 0.3$  with 90 per cent credibility. This selection has been done because a higher level of completeness for catalogues of observed AGN can be reached if we restrict our analysis to the local Universe. Future works might explore the GW-AGN correlation on a wider redshift range. The effectiveness of their results will be increased because of the possible exploitation of more detected BBH mergers, but might also be damped by low levels of completeness of the considered AGN catalogues.

Dedicated tests performed by varying the different parameters in the Monte Carlo analysis described in Section 3.3.2 have proven that the prediction power of the method presented in this work depends mainly on three elements: the completeness of the AGN catalogue, the number of GW detections, and the size of their localisation volumes. Observational limitations (e.g. the presence of the Milky Way plane that does not allow the detection of light coming from objects behind it) prevent us from having an AGN catalogue with a completeness level close to unity. On the other hand,  $79^{+89}_{-44}$  BBH mergers are expected to be observed via GWs during the fourth observing run (O4) of the LIGO-Virgo-KAGRA collaboration (Abbott et al. 2020), and at least the same amount of detections can be predicted for the fifth observing run (O5). This would at least triple the amount of detected events available for statistical analyses on the BBH population. This increase of the number of detections, together with

the improvement on the localisation power expected for O4 and O5 with respect to previous observing runs, will noticeably increase the prediction power of likelihood-based methods like the one presented in this paper, that will be able to put more stringent constraints on the fractional contribution of high-luminosity AGN to the total BBH merger rate, and to make use of also denser catalogues of potential hosts, such as the ones containing AGN with luminosities lower than the ones considered in this work.

## Acknowledgements

The authors thank Ilya Mandel for the stimulating discussion regarding the how to assess the validity of the method when tested on simulated data, and the anonymous referee for their comments that helped to improve the presentation of our results. EMR acknowledges support from ERC Grant “VEGA P.”, number 101002511. This research has made use of data or software obtained from the Gravitational Wave Open Science Center ([gwosc.org](http://gwosc.org)), a service of LIGO Laboratory, the LIGO Scientific Collaboration, the Virgo Collaboration, and KAGRA. LIGO Laboratory and Advanced LIGO are funded by the United States National Science Foundation (NSF) as well as the Science and Technology Facilities Council (STFC) of the United Kingdom, the Max-Planck-Society (MPS), and the State of Niedersachsen/Germany for support of the construction of Advanced LIGO and construction and operation of the GEO600 detector. Additional support for Advanced LIGO was provided by the Australian Research Council. Virgo is funded, through the European Gravitational Observatory (EGO), by the French Centre National de Recherche Scientifique (CNRS), the Italian Istituto Nazionale di Fisica Nucleare (INFN) and the Dutch Nikhef, with contributions by institutions from Belgium, Germany, Greece, Hungary, Ireland, Japan, Monaco, Poland, Portugal, Spain. KAGRA is supported by Ministry of Education, Culture, Sports, Science and Technology (MEXT), Japan Society for the Promotion of Science (JSPS) in Japan; National Research Foundation (NRF) and Ministry of Science and ICT (MSIT) in Korea; Academia Sinica (AS) and National Science and Technology Council (NSTC) in Taiwan. *Software:* Numpy ([Harris et al. 2020](#)); Matplotlib ([Hunter 2007](#)); SciPy ([Virtanen et al. 2020](#)); Astropy ([Astropy Collaboration et al. 2013, 2018](#)); BAYESTAR ([Singer & Price 2016](#)).

## Data Availability

The data underlying this article are available in  
niccoloveronesi/AGNallskycat\_Veronesi23, at

[https://github.com/niccoloveronesi/AGNallskycat\\_Veronesi23.git](https://github.com/niccoloveronesi/AGNallskycat_Veronesi23.git).



# 4

# AGN FLARES AS COUNTERPARTS TO THE MERGERS DETECTED BY LIGO AND VIRGO: A NOVEL SPATIAL CORRELATION ANALYSIS

Work publicly available in **N. Veronesi**, S. van Velzen, E. M. Rossi  
<https://arxiv.org/pdf/2405.05318.pdf>, currently under review for publication on *Monthly Notices of the Royal Astronomical Society*, Reprinted here in its entirety.

## Abstract

The primary formation channel for the stellar-mass Binary Black Holes which have been detected merging by the LIGO-Virgo-KAGRA (LVK) collaboration is yet to be discerned. One of the main obstacles is that such Gravitational Wave (GW) events are not in general expected to produce an Electromagnetic (EM) counterpart. This might not be the case if the mergers happen in gaseous environments, such as the accretion discs of Active Galactic Nuclei (AGN). Recently, 20 AGN flares detected by the Zwicky Transient Facility have been investigated as potential counterparts of GW events by Graham et al. (2023). We present a new spatial correlation analysis involving such events that uses the up-to-date posterior samples of 78 mergers detected during the third observing run of the LVK collaboration. We apply a likelihood method which takes into account the exact position of the EM signal within the 3D sky map of the GW events. We find that current data favour the hypothesis of no causal connection between the detected mergers and the AGN flares. We place an upper limit of 0.155 at a 90 per cent credibility level on the fraction of coalescences that are physically related to a flare. Moreover, we show that the mass distribution of the merging binaries that appear in coincidence with AGN flares, characterised by values typically larger than the ones of the full population of GW events, is also consistent with the no-connection hypothesis. This is because of a positive correlation between the binary mass and the reconstruction volume.

## 4.1 Introduction

During the third observing run (O3) of the LIGO-Virgo-KAGRA (LVK) collaboration, Gravitational Waves (GWs) coming from 80 confirmed mergers of binaries of compact objects were detected ([Abbott et al. 2023a, 2024](#)). Several channels for the formation of the merging systems have been proposed (see [Mapelli 2021](#), for a recent review). These pathways can be divided into two main categories: the evolution of isolated stellar binary systems, and the formation inside dense environments, such as Nuclear Star Clusters or accretion discs of Active Galactic Nuclei (AGN). The formation of merging Binary Black Holes (BBHs) in AGN discs is expected to be facilitated not only by the high density of compact objects, but also by their dynamical interaction with the gas ([Stone et al. 2017; Tagawa et al. 2020; Li & Lai 2022, 2023b,a; DeLaurentiis et al. 2023a; Qian et al. 2024; Rowan et al. 2023, 2024; Rodríguez-Ramírez et al. 2024](#)). For this reason, the so-called “AGN-channel” for the formation of merging binaries has been recently studied and modelled extensively.

The component masses of binaries coalescing in accretion discs around Massive Black Holes are expected to populate the high end of the astrophysical stellar-mass Black Hole mass spectrum presented in [The LIGO Scientific Collaboration et al. \(2021\)](#). This is mainly because Type I migration caused by the interaction between a gaseous disk and the compact objects within it makes mass segregation very efficient, since the migration time-scale is inversely proportional to the mass of the compact object ([Armitage 2007; McKernan et al. 2011; Secunda et al. 2019](#)). Moreover, the vicinity to the central Massive Black Hole implies that mergers of compact objects inside an AGN accretion disc happen in the presence of a deep gravitational potential. For this reason, the speed at which the remnant objects get kicked from the location of the merger, typically of the order of hundreds of kilometres per second, is likely lower than the escape speed of the environment. Therefore there is the possibility for it to be retained and to take part to another BBH merger. In this scenario of hierarchical mergers, the components of the binaries are expected to have high masses and dimensionless spins close to  $\approx 0.7$ , which is the value that the remnant of a previous merger is expected to have, due to total angular momentum conservation ([Gerosa & Berti 2017; Gerosa & Fishbach 2021](#)). In addition, binaries of compact objects merging inside an AGN disc have been modelled as able to develop and maintain a measurable level of eccentricity also in the LVK frequency range ([Samsing et al. 2022; Calcino et al. 2023; Fabj & Samsing 2024](#)). The detection of non-zero eccentricity in one or more GW signals would therefore

represent a strong hint regarding the efficiency of disc-assisted BBH formation. Finally, the symmetry of an astrophysical environment such as a rotating disc has been claimed to be sufficient to explain the anti-correlation between the binary effective spin parameter  $\chi_{\text{eff}}$  and the mass ratio  $q$  that has been observed in the population of mergers detected by the LVK collaboration (McKernan et al. 2022a; Santini et al. 2023). The comparison of the binary parameters' distributions predicted for the AGN channel with the ones of detected GW events is a viable approach for estimating the fractional contribution of this formation path to the total BBH merger rate. Nevertheless, such approach is not the only one. It is in fact also possible to put constraints on the this channel's efficiency by analysing the spatial correlation between the sky maps of the events detected by the LVK interferometers and the positions of observed AGN (Bartos et al. 2017a; Veronesi et al. 2022, 2023). In particular, in Veronesi et al. (2023) was found that the fraction of detected BBH mergers that took place in an AGN brighter than  $10^{45.5} \text{erg s}^{-1}$  ( $10^{46} \text{erg s}^{-1}$ ) is lower than 0.49 (0.17) at 95 per cent credibility level.

A third way to identify the host environment of the merging binaries is the direct detection of a transient Electromagnetic (EM) counterpart. The vast majority of the detected GW events are coalescences of BBHs, which are not generally expected to produce a detectable associated EM signal. However, such counterparts are expected to be produced, even if not necessarily detectable, whenever mergers take place in gaseous environments, like AGN accretion discs (Bartos 2016b; McKernan et al. 2019). A possible origin of these counterparts is Bondi accretion on the merging objects at a hyper-Eddington rate, that triggers a Bondi explosion (Wang et al. 2021c). Another potential source of a detectable EM transient is a jet coming from the accretion of magnetized medium onto the remnant object that traverses the gaseous disc after receiving a recoil kick from the merger event (Chen & Dai 2024). Recently Graham et al. (2023, G23, hereafter) have identified AGN 20 unusual flaring activities observed by the Zwicky Transient Facility (ZTF; Bellm et al. 2019; Graham et al. 2019) as potential EM counterparts of the GW events detected during O3. These transients have been labelled as not caused by Supernovae (SNe), Tidal Disruption Events (TDEs), or regular AGN variability. A possible physical cause of such flares is Bondi drag accretion and shock of the gas that interacts gravitationally with the kicked remnant of a merger event that happened inside the disc. The flare is expected to be manifest when such remnant reaches the  $\tau = 1$  optical depth surface of the disc. In Tagawa et al. (2024) is presented an emission model based on the presence of a Blandford-Znajek jet produced from BHs in AGN discs (Tagawa et al. 2022, 2023), and it is applied to the flares reported in

G23, finding that such model can be consistent with the observed events after a number of assumptions were made, mainly regarding the accretion rate onto the stellar-mass BH, and the fraction of jet power that ends up in radiation.

In this work we present the results of a spatial and temporal correlation study for the identification of the host environment of the mergers detected by the LVK collaboration. In particular, this analysis focuses on the connection between the mergers detected during O3 and the 20 EM transients presented and examined in G23.

We calculate the posterior probability distribution of  $f_{\text{flare}}$ , the fraction of the LVK events detected during O3 that are causally connected to an AGN flare. We do this by using an adapted version of the statistical approach presented in Veronesi et al. (2023). This is a model-independent approach, we only take into account spatial and temporal correlation, but otherwise remain agnostic about which AGN and GW events are favorable counterparts.

In Section 4.2 we present the properties of the data that have been used in the analysis, which include the GW detections and the AGN flares considered as potential EM counterparts. The description of the statistical method used to check the significance of the GW-AGN flares connection is in Section 4.3, while the results of its application to the observed data are presented in Section 4.4. Finally, in Section 4.5 we draw final conclusions from our results and discuss what are their implications concerning the physical relation between BBH mergers and AGN flares.

We adopt the cosmological parameters of the Cosmic Microwave Background observations by Planck (Planck Collaboration et al. 2016):  $H_0 = (67.8 \pm 0.9) \text{ km s}^{-1}\text{Mpc}^{-1}$ ,  $\Omega_m = 0.308 \pm 0.012$ , and  $n_s = 0.968 \pm 0.006$ .

## 4.2 Datasets

In this section we first present the main properties of the AGN flares selected in G23 as potential EM counterparts to O3 detections. We then describe and list the GW events we use in our analysis. Finally we show all the spatial and temporal associations that exist between the two catalogues, both in the case of a 3D cross-match, and in the case of a 2D sky-projected one.

### 4.2.1 AGN flares

All the AGN flares we use in our analysis have been observed by ZTF. This facility uses a  $47\text{deg}^2$  field-of-view camera to cover the majority of the sky

above a declination of  $-30^\circ$  every two or three nights in the g-band and in the r-band. To select potential EM counterparts for the GW events detected during O3, in G23 the data from the fifth release (DR5)<sup>1</sup> were used, and the search has been limited to AGN at a redshift  $z \leq 1.2$ , given the sensitivity the interferometers of LIGO and Virgo had during O3. The light curves of the observed AGN flares have been fitted with a Gaussian rise - exponential decay form (see Equation 13 in G23). From the original full sample were then removed all the flares that have been considered as originated from SNe, TDEs, or regular AGN variability. This selection has been done based on the timescales of the transients, their g-r colour, their rate of colour evolution, and their total observed energy. The resulting selected sample consists of 20 AGN flares that are considered as potential EM counterparts for the GW events detected during O3. All these flares have peaked during the time window that can allow a causal connection with at least one merger. This temporal match is considered possible if the AGN has not flared before the first GW detection or more than 200 days after the last one. Any merger happening after that time is not considered as a potential counterpart, since the estimated time required for the remnant of the merger to reach the edge of the accretion disc is of the order of tens of days.

In Table 4.1 we list the main properties of the 20 potential counterparts. In particular we report the name of the AGN, the Right Ascension (RA) and Declination (Dec), the redshift, the Modified Julian Day (MJD) of the peak, and the Gaussian rise time of the light curve,  $t_g$ . The sky distribution of these transients is shown in Figure 4.1.

### 4.2.2 GW events

We make use of 78 GW events detected during O3, which are contained in the Gravitational Wave Transient Catalog (GWTC) 2.1 (Abbott et al. 2024) and in GWTC 3 (Abbott et al. 2023a). The former includes all the events detected up to the first half of O3, O3a, started on April 1st, 2019 and ended on October 1st of the same year, while the latter includes all the events detected during the second half of O3, O3b, that started on November 1st, 2019, and ended on March 27th, 2020. We only had to exclude GW200308\_173609 and GW200322\_091133 because for these two poorly-localized events the posterior samples do not allow the evaluation of the size of the 90 per cent Credibility Level localisation volume (V90).

We work with the latest (at the time in which this paper is written) ver-

---

<sup>1</sup><https://www.ztf.caltech.edu/page/dr5>

**Table 4.1:** List of the 20 AGN flares that were selected in G23 as potential EM counterparts of GW events detected during O3. We report the name of the flaring object, its Right Ascension and Declination, its redshift, the MJD of the peak, and the Gaussian rise timescale. For J053408.41+085450.6 we use the same photometric estimate of the redshift that has been used in G23. For the AGN located at J150748.68+723506.1 and at J234420.76+471828.9 there is no available redshift estimate in the literature. These two sources are therefore excluded from the three-dimensional spatial correlation analysis presented in the following sections.

AGN name	RA [deg]	Dec [deg]	Redshift	MJD <sub>peak</sub>	$t_g$ [days]
J053408.42+085450.7	83.535	8.914	0.5*	58890	17
J120437.98+500024.0	181.158	50.007	0.389	58894	17
J124942.30+344928.9	192.426	34.825	0.438	58671	16
J140941.88+552928.1	212.425	55.491	0.074	58616	11
J143157.51+451544.0	217.990	45.262	0.693	58859	12
J143536.15+173755.4	218.901	17.362	0.095	58673	9
J145500.22+321637.1	223.751	32.277	0.177	58590	14
J150748.68+723506.1	226.953	72.585	—	58971	20
J152433.35+274311.6	231.139	27.720	0.069	58611	8
J154342.46+461233.4	235.927	46.209	0.599	58975	21
J154806.31+291216.3	237.026	29.205	1.090	58997	55
J160822.16+401217.8	242.092	40.205	0.627	58921	27
J161833.77+263226.0	244.641	26.541	0.126	58600	11
J163641.61+092459.2	249.173	9.416	1.155	58694	9
J181719.95+541910.0	274.333	54.319	0.234	58784	17
J183412.42+365655.2	278.552	36.949	0.419	58689	13
J224333.95+760619.2	340.891	76.105	0.353	58772	11
J233252.05+034559.7	353.217	3.767	1.119	58855	40
J233746.08-013116.3	354.442	-1.521	0.115	58703	8
J234420.76+471828.9	356.087	47.308	—	58669	11

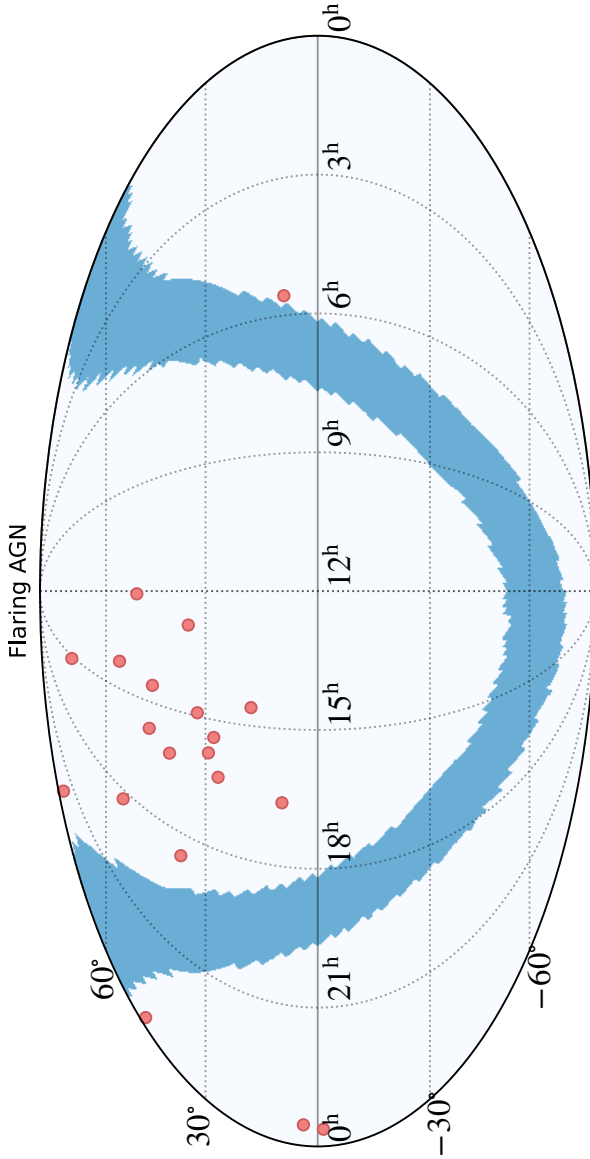


**Figure 4.1:** Mollweide projection of the sky position of the 20 AGN flare identified as potential EM counterparts of GW events in G23. The resolution corresponds to the one of an HealPix map with NSIDE=32. The pink markers correspond to the position of the flares, while the light blue region correspond to pixels that have a galactic latitude between  $-10^\circ$  and  $10^\circ$ . They correspond to the region that includes the galactic plane.

sions of the posterior samples published by the Gravitational Wave Open Science Center (GWOSC) ([Abbott et al. 2023b](#)). Such samples were published on May 13th, 2022 for GWTC-2.1, and on June 23rd, 2023 for GWTC-3. Since G23 has been published in January 2023, we make use of a different, updated version of the posterior distributions for the events of GWTC-3, with respect to such work. The same is true for all the GW events for which in G23 GWTC-2.0 has been used. For such mergers, we use the posterior distributions of GWTC-2.1. The posterior samples coming from the IMRPHENOMXPHM ([Pratten et al. 2021](#)) waveform model have been used for every GW event a part from GW190425\_081805, GW191219\_163120, GW200105\_162426, and GW200115\_042309, for which the MIXED posterior samples were used.

To reproduce the analysis of GW23, we have to estimate the fraction of the 90 per cent credibility level localisation area ( $A_{90}$ ) that is outside the galactic plane and has been observed by ZTF at least 20 times in both the g-band and r-band in the 200 days following the LVK detection. This threshold number of observations is used to be consistent with G23. We call this parameter  $f_{\text{cover}}$ . To calculate it we use the ZTF forced photometry service ([Masci et al. 2023](#)) to obtain the number and the MJD of the observations at each sky location. The values of  $f_{\text{cover}}$  for all the sky maps we use in this work are listed in Table 4.4, together with the ID of the corresponding GW event, the catalogue it is contained in, the sizes of  $A_{90}$  and  $V_{90}$ , and the MJD of the detection. The sizes of  $V_{90}$  we report refer to comoving localisation volumes, and not to Euclidean volumes in luminosity distance. This choice implies a cosmological model to be assumed during the cross-matching process, but leads to no difference in its results.

### 4.2.3 Matching events

The positions of the 20 flares listed in Table 4.1 are cross-matched with the sky maps of the GW events listed in Table 4.4. This is done using the `postprocess.crossmatch` function of the `ligo.skymap` package, searching space by descending probability density per unit comoving volume. The cross-matching is performed both in the 3D comoving space, and in the 2D sky-projected space. For the 3D case, the two AGN flares without any redshift information are excluded. This is consistent with the approach used in G23, since these two potential counterparts are also not contained in their sample of 7 matching events.

To be considered as matching with a merger event, an AGN flare has to be found within the 90 per cent Credibility Level localisation volume (or area)

**Table 4.2:** List of the 3D matches between GW events detected during O3 and AGN flares contained in ZTF DR5 and identified as potential EM counterparts. We report the ID of the GW event, the name of the flaring AGN, and the credibility level of its position within the localisation volume of the binary merger.

GW ID	AGN name	Credibility level
GW190514_065416	J224333.95+760619.2	0.175
GW190521_030229	J124942.30+344928.9	0.360
GW190620_030421	J124942.30+344928.9	0.778
GW190706_222641	J183412.42+365655.2	0.181
GW190708_232457	J233746.08-013116.3	0.839
GW190719_215514	J181719.95+541910.0	0.185
GW190731_140936	J053408.42+085450.7	0.479
GW190803_022701	J053408.42+085450.7	0.644
GW190803_022701	J120437.98+500024.0	0.543
GW200128_022011	J120437.98+500024.0	0.879
GW200216_220804	J154342.46+461233.4	0.727
GW200220_124850	J154342.46+461233.4	0.137

of the sky map. Following GW23, we also require that the difference between the flare’s peak time and the GW detection time is smaller than 200 days and larger than the flare’s Gaussian rise time. The 3D (2D) cross-matching process leads to a total of 12 (32) matches. These are listed in Table 4.2 and Table 4.3. For each match we list the ID of the corresponding GW event, the name of the flaring AGN, and the credibility level corresponding to its position within the sky map of the merger.

### 4.3 Method

The goal of this work is to establish whether the matches between GW events and AGN flares that are listed in Table 4.2 and Table 4.3 are due to a causal connection or to random chance association. To do this, we calculate the posterior distribution of the parameter  $f_{\text{flare}}$ , the fraction of detected mergers that have a connection with a flaring event. We use an adapted version of the likelihood function presented in [Veronesi et al. \(2023\)](#). The general form of this function

**Table 4.3:** List of the 2D sky-projected matches between GW events detected during O3 and AGN flares contained in ZTF DR5 and identified as potential EM counterparts. We report the ID of the GW event, the position of the flaring AGN name, and the credibility level of such position within the localisation area of the binary merger.

GW ID	AGN position	Credibility level
GW190425_081805	J124942.30+344928.9	0.750
GW190425_081805	J140941.88+552928.1	0.555
GW190425_081805	J152433.35+274311.6	0.281
GW190425_081805	J163641.61+092459.2	0.120
GW190514_065416	J224333.95+760619.2	0.479
GW190519_153144	J234420.76+471828.9	0.206
GW190521_030229	J124942.30+344928.9	0.640
GW190620_030421	J124942.30+344928.9	0.747
GW190620_030421	J143536.15+173755.4	0.893
GW190620_030421	J163641.61+092459.2	0.597
GW190706_222641	J183412.42+365655.2	0.685
GW190708_232457	J233252.05+034559.7	0.713
GW190708_232457	J233746.08-013116.3	0.626
GW190719_215514	J181719.95+541910.0	0.727
GW190731_140936	J053408.42+085450.7	0.379
GW190803_022701	J053408.42+085450.7	0.777
GW190803_022701	J120437.98+500024.0	0.544
GW190403_051529	J124942.30+344928.9	0.660
GW190403_051529	J140941.88+552928.1	0.856
GW191126_115259	J150748.68+723506.1	0.888
GW191129_134029	J154342.46+461233.4	0.895
GW191219_163120	J154342.46+461233.4	0.409
GW200105_162426	J053408.42+085450.7	0.790
GW200105_162426	J154342.46+461233.4	0.552
GW200105_162426	J154806.31+291216.3	0.369
GW200105_162426	J160822.16+401217.8	0.819
GW200112_155838	J154342.46+461233.4	0.839
GW200112_155838	J160822.16+401217.8	0.341
GW200210_092255	J154342.46+461233.4	0.836
GW200216_220804	J154342.46+461233.4	0.820
GW200216_220804	J154806.31+291216.3	0.890
GW200220_124850	J154342.46+461233.4	0.145

is the following:

$$\begin{aligned} \mathcal{L}(f_{\text{flare}}) &= \prod_{i=1}^{N_{\text{GW}}} \mathcal{L}_i(f_{\text{flare}}) \\ &= \prod_{i=1}^{N_{\text{GW}}} [f_{\text{cover},i} \cdot 0.90 \cdot f_{\text{flare}} \cdot \mathcal{S}_i + (1 - f_{\text{cover},i} \cdot 0.90 \cdot f_{\text{flare}}) \mathcal{B}_i], \end{aligned} \quad (4.1)$$

where  $N_{\text{GW}}$  is the total number of GW detections. The value of  $f_{\text{cover},i}$  is used to weight the contribution of the  $i$ -th single-event likelihood function. For example, a GW event which sky map is characterised by  $f_{\text{cover}} = 0$  cannot contain any information regarding the connection with AGN flares observed by ZTF. Using  $f_{\text{cover}}$  as weight in the likelihood calculation takes this into account.

The signal probability density for the  $i$ -th GW event is calculated as follows:

$$\mathcal{S}_i = \sum_{j=1}^{N_{\text{matches}_i}} \frac{p_j}{n_{\text{flare},j}} \frac{1}{V90_i}, \quad (4.2)$$

where  $N_{\text{matches}_i}$  is the number of spatial and temporal matches the  $i$ -th GW event has with flares,  $p_j$  is the probability density associated to the position of the  $j$ -th matching EM transient, and  $n_{\text{flare},j}$  is the effective spatial number density correspondent to it. This number density is assumed to be uniform within V90.

In the analysis that involves the 2D sky-projected cross-match, A90 is used instead of V90, and both  $p_j$  and  $n_{\text{flare},j}$  are in units of  $\text{deg}^{-2}$ , and not in units of  $\text{Mpc}^{-3}$ . We calculate the effective number density as follows:

$$n_{\text{flare},j} = \frac{20}{V_{\text{ZTF,eff}}} \frac{200 - t_{g,j}}{\Delta t_{\text{search}}}, \quad (4.3)$$

where 20 is the total number of AGN flares selected from ZTF DR5 as potential counterparts of GW events,  $V_{\text{ZTF,eff}} = 1.066 \times 10^{11} \text{ Mpc}^3$  is the total effective surveyed comoving volume, and  $\Delta t_{\text{search}} = 562$  days is the total observing time of the search, between the start of O3 and 200 days after its end. We calculate the total effective comoving volume in order for it to be compatible with how  $f_{\text{cover}}$  has been calculated for each GW event, and to take into account the non uniformity of the source density in the ZTF footprint. We first map the sky into a HealPix grid with a resolution of NSIDE=32. To each pixel correspondent to a galactic latitude lower than  $-10^\circ$  or greater than  $10^\circ$  is then associated a

number between 0 and 1. This value is the fraction of the total number of GW events for which that specific pixel was observed at least 20 times in both the ZTF g-band and r-band in the 200 days following the merger detection. These values are then all summed together and the result is multiplied by the angular size of each pixel. This sum corresponds to the total effective area observed by the survey during  $\Delta t_{\text{search}}$ ,  $A_{\text{ZTF,eff}}$ , and is used in the calculation of  $n_{\text{flare},j}$ , instead of  $V_{\text{ZTF,eff}}$ , in the case of the 2D sky-projected analysis. The value of  $V_{\text{ZTF,eff}}$  is finally calculated multiplying the total comoving volume enclosed within the redshift limit adopted in the search presented in G23,  $z = 1.2$ , by the ratio between  $A_{\text{ZTF,eff}}$  and the total area of the sky. Finally, the numerator of the second fraction in Equation 4.3 takes into account the width of the time window within which a specific flare has to peak in order to allow the match with a GW event. We calculate this quantity by subtracting the Gaussian rise time of the flare from 200 days, the maximum allowed delay time between the peak of such EM transient and the GW detection.

The background probability density function  $\mathcal{B}_i$  is calculated in the same way as in Veronesi et al. (2023):

$$\mathcal{B}_i = \frac{0.9}{V90_i}, \quad (4.4)$$

where the 0.9 factor is used so that  $\mathcal{S}_i$  and  $\mathcal{B}_i$  are normalised to the same value. Just like the signal density function (Equation 4.2) A90 is used instead of V90 for the 2D cross-matching analysis.

After normalising  $\mathcal{L}(f_{\text{flare}})$  using a flat prior on  $f_{\text{flare}}$  in the  $[0, 1]$  interval, we obtain the posterior distribution of this parameter.

## 4.4 Results

In this Section we present the posterior distribution of the fraction of detected GW events that have a connection with an AGN flare,  $f_{\text{flare}}$ . Then we show the results of two more tests to check if this posterior is indeed compatible with the  $f_{\text{flare}} = 0$  hypothesis. The first of the two tests focuses the total number of matches between the catalogue of AGN flares and the one of GW events, the second on the binary mass distribution one should expect for the mergers characterised by at least one match.

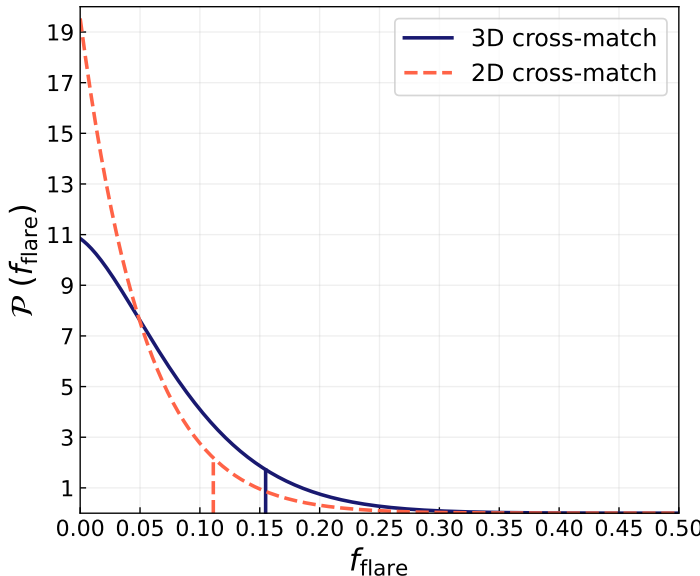


**Figure 4.2:** Posterior probability distribution on the fraction of GW events that are expected to have caused a flare in an AGN,  $f_{\text{flare}}$ . The solid blue line corresponds to the result of the 3D cross-matching analysis, while the dashed pink line to the one of the 2D sky-projected case. Both functions peak at  $\hat{f}_{\text{flare}} = 0$ . The vertical lines indicate the upper limits of the 90 per cent Credibility Intervals. These correspond to  $f_{\text{flare}} = 0.155$  and  $f_{\text{flare}} = 0.111$  for the 3D and 2D cross-matching analysis, respectively.

#### 4.4.1 Posterior distributions

The posterior probability distribution on  $f_{\text{flare}}$  is estimated using the data presented in Section 4.2 and the method described in Section 4.3. The result is shown in Figure 4.2. For both the 3D and the 2D cross-matching analyses, the posterior distribution peaks at  $\hat{f}_{\text{flare}} = 0$ . In the case of the 3D analysis, the upper limits of the 68, 90, and 95 per cent Credibility Intervals (CIs) correspond to  $f_{\text{flare}} = 0.085$ ,  $f_{\text{flare}} = 0.155$ , and  $f_{\text{flare}} = 0.192$ , respectively. The upper limits for the same CIs in the 2D sky-projected analysis are  $f_{\text{flare}} = 0.056$ ,  $f_{\text{flare}} = 0.111$ , and  $f_{\text{flare}} = 0.142$ .

#### 4.4.2 Background Monte Carlo realisations

The posterior distributions presented in Section 4.4.1 peak at  $\hat{f}_{\text{flare}} = 0$ , which corresponds to the hypothesis of no causal connection between mergers detected by the LVK interferometers and the AGN flares selected as potential EM counterparts for such events. In other words, the positioning of the flares within the GW sky maps, and the observed number of matches between GW events and AGN flares appear consistent with chance associations only, without any physical relation between the two events.

To further test this hypothesis, we perform 500 Monte Carlo (MC) realisations of this background scenario. Each of them is constructed as follows:

- To generate a catalog of AGN flares that follows the ZTF real sampling of the sky, which is not fully uniform within the footprint, we sample 20 sky-positions from the catalogue of extra-galactic transient events presented in [van Velzen et al. \(2024\)](#);
- For each simulated flare, we select its peak time by drawing from the times its sky position was observed by ZTF. To match the peak time distribution of the 20 flares from G23, we require this peak time to be later than the start of O3 and earlier than the date that corresponds to 200 days after the end of the same observing run;
- To each of the 20 sampled positions we associate a value of redshift. This is obtained by inverse-sampling a linear interpolation of the Cumulative Distribution Function of the redshifts of the potential EM counterparts to GW events listed in Table 4.1;
- To each flare we associate a value for its rise time  $t_g$ , drawn randomly from the ones listed in Table 4.1;
- Once the catalogue of simulated background ZTF flares is constructed, it is cross-matched with the 3D sky maps of the GW events detected during O3 and listed in Table 4.4. As for the cross-match performed with observed data, in order for a match to be considered as valid, the flare has to peak not more than 200 days after the GW detection, and not before that a number of days equal to the corresponding  $t_g$  have passed.

The histogram in Figure 4.3 shows the distribution of the number of spatial and temporal matches obtained in the 500 MC realisations of the background scenario. The average value of the sample is  $\bar{N}_{\text{matches}} = 14.9$  and its standard

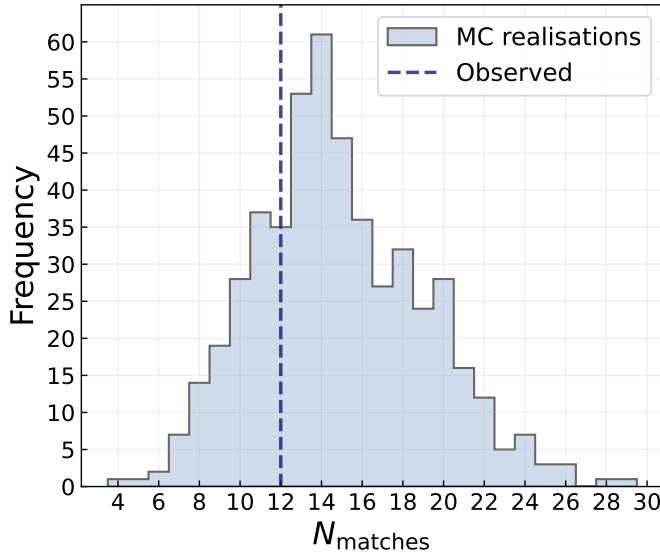


**Figure 4.3:** Distribution of the number of spatial and temporal matches between simulated ZTF AGN flares and GW 3D sky maps obtained from 500 MC realisations. Each of these realisations represents the scenario in which there is no causal connection between the two different signals, and every match is due to random chance association. The average of the distribution is  $\bar{N}_{\text{matches}} = 14.9$ , and its standard deviation is  $\sigma(N_{\text{matches}}) = 4.2$ . The vertical dashed line indicates the number of matches that have been found using real observed data (see Table 4.2).

deviation is  $\sigma(N_{\text{matches}}) = 4.2$ . The number of matches obtained from observed data (12) is less than one standard deviation away from the mean of the distribution. It is reasonable then to assess that 12 matches can be expected even only due to random chance association.

For each MC realisation, the posterior distribution of  $f_{\text{flare}}$  is also obtained. In 150 realisations this function peaks at  $\hat{f}_{\text{flare}} = 0$ , and the distribution of the value of  $\hat{f}_{\text{flare}}$  extends to  $\hat{f}_{\text{flare}} \approx 0.26$ . This is similar to the posterior of  $f_{\text{flare}}$  obtained from observed data, again confirming that the outcome of our likelihood method (Eq.4.1) is consistent with the background hypothesis.

### 4.4.3 Binary Mass distributions

Due primarily to mass segregation and the possibility of undergoing subsequent hierarchical mergers, BBHs that coalesce inside dynamically dense environments like the accretion discs of an AGN are expected to have on average a higher mass with respect to the ones that formed through the evolution of an isolated binary stellar system. In Figure 4.4 it is shown the size of V90 for each GW event detected during O3, weighted by  $f_{\text{cover}}$ , as a function of the source-frame total mass of the merging binary. The horizontal and the vertical dashed lines indicate the median weighted size of V90 and the median total mass, respectively. The pink non-round markers indicate the 11 GW events that have at least one 3D match with a potential EM counterpart. We indeed notice that most of matching GW events have a total mass that is higher than the median. A KS test for the hypothesis that the mass distributions of the matching and the non-matching merging binaries are not related yields  $p = 0.018$ . However, this apparent difference in mass might be because the matching events are also associated with localisation uncertainties larger than the median. To test this hypothesis we follow the procedure presented hereunder:

- The average effective flare number density,  $\langle n_{\text{flare}} \rangle$ , is first calculated from Equation 4.3, using the average rise time of the flares listed in Table 4.1,  $\langle t_g \rangle = 17.35$ ;
- For all the GW events we evaluate the expected number of matches due to chance association,  $N_{\text{matches,exp}}$ , multiplying the size of their localisation volume by  $\langle n_{\text{flare}} \rangle$ ;
- We extract a number of matches for each GW event, drawing from a Poisson distribution with  $N_{\text{matches,exp}}$  as expectation value;
- We finally perform a two-sample Kolmogorov-Smirnov test between the distribution of the source-frame total mass of the GW events that have at least one match in this random sample and the distribution of the source-frame mass of the ones that don't have any match. For each repetition we therefore obtain a value of the KS statistic.

The whole process is repeated 10,000 times. The histogram in Figure 4.5 shows the distribution of the KS statistic for all the repetitions of the random sampling. We see that the KS statistic of the observed 11 matching GW events is consistent with the distribution obtained from the random sampling process. This means that the fact that the observed matching events correspond on average to higher

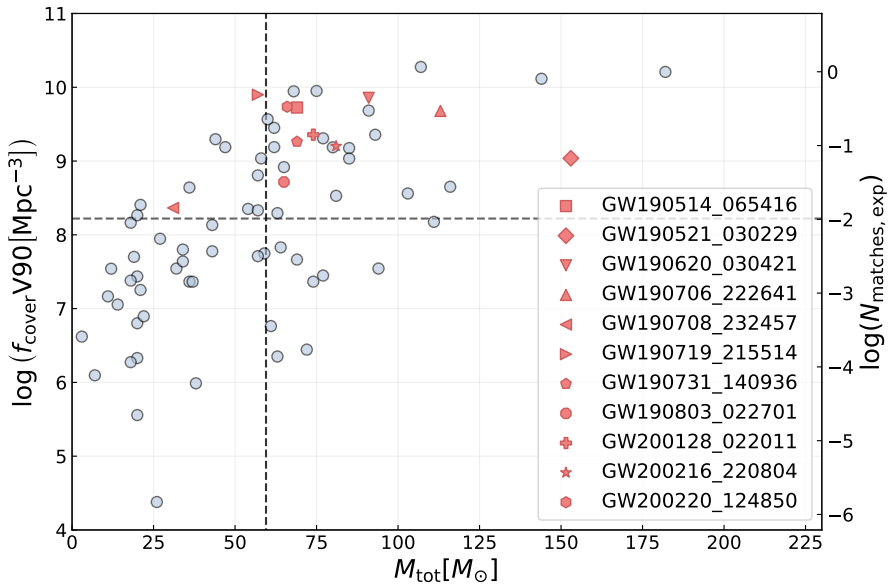


**Figure 4.4:** Effective size of V90 of the GW events detected during O3 as a function of the source-frame total mass of the binary. The 11 pink non-round markers indicate the mergers that have a spatial and temporal match with at least one of the AGN flares listed in Table 4.1. These matching sources appear to have a large mass compared to the median of the entire population (indicated with the dashed lines). However this can be explained by the correlation between mass and volume, see also Figure 4.5. On the right-hand side y-axis is indicated the expectation number of random matches evaluated assuming a uniform average effective number density calculated from Equation 4.3, using the mean  $t_g$  of the AGN flares.

binary masses with respect to the non-matching ones should be expected due to random chance association between GW sky maps and the AGN flares.

## 4.5 Discussion and conclusion

We present a statistical investigation on the connection between the GW events detected during O3 and the AGN flares selected in G23 as potential EM counterparts. We do this using the most updated version of the posterior samples released by the LVK collaboration. We make use of the statistical method presented in Veronesi et al. (2023) to estimate the posterior distribution over the fraction of GW events that have an observed AGN flare as an EM counterpart,  $f_{\text{flare}}$ . We repeat the same analysis both performing a 3D cross-match between the GW sky maps and the positions of the flares, and a 2D sky-projected one. In both cases the posterior distribution peaks at  $\hat{f}_{\text{flare}} = 0$ .

The upper limit of the 90 per cent CI is  $f_{\text{flare}} = 0.155$  in the case of the 3D cross-matching analysis and  $f_{\text{flare}} = 0.111$  for the 2D sky-projected case.

Moreover, we perform 500 MC realisations of the background hypothesis, according to which the matches between GW events and AGN flares are due to random chance association. We find that the total number of matches that exist in the case of the real observed data (12) is compatible with this scenario.

Finally we find through a random sampling process, that the observed distribution of source-frame binary masses of the mergers that have a spatial and temporal match with at least one AGN flare is compatible with the same no-connection hypothesis.

We conclude that the hypothesis of no causal connection between detected GW events and AGN flares cannot be rejected. Moreover, it appears this hypothesis is preferred by currently available data, since the posterior on  $f_{\text{flare}}$  we obtain peaks at zero.

In G23 Poisson statistic is used to calculate the probability of obtaining a number of matches equal or bigger than the observed one under the no causal connection hypothesis. They estimate this probability to be  $p = 0.0019$ . The estimate for the number of expected random matches used in G23 (2.83) is calculated assuming a spatial number density uniform in comoving volume up to  $z = 1.2$  and a temporal distribution of the flares over the whole duration of the data collection of ZTF DR5. This estimate is not compatible with the average number of matches we obtain in our Monte Carlo realisations of the background hypothesis (14.9). A key difference is that we take into account non-uniform distributions of the sky-position (by sampling from ZTF sources to

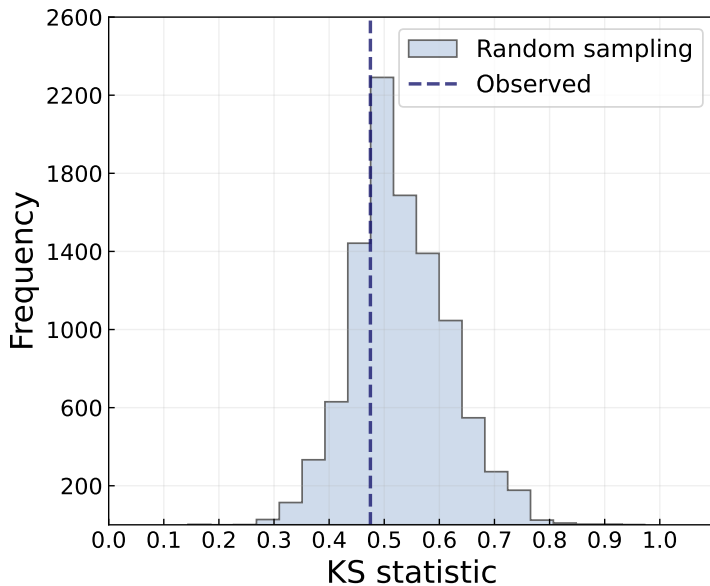


**Figure 4.5:** Distribution of the KS statistic obtained by comparing the source-frame total binary masses of GW events with a 3D spatial match with an AGN flare with the ones of the other mergers detected during O3. The histogram shows the distribution of such statistic obtained from 10,000 repetitions of random sampling, where the number of matches of every GW event was drawn from a Poisson distribution that depends on the corresponding size of V90. The vertical dashed blue line indicates the value of the KS statistic calculated with the observed data. After correcting for the correlation between mass and V90, we thus find no evidence for a difference between the mass distribution of the GW sources that match to AGN flares and the mass distributions of the ones that do not.

obtain a realistic sky distributions) and redshift of the AGN flares (by sampling from the redshifts of the observed flares), and we allow these transient events to peak only in the time window that includes all the 20 selected potential counterparts. Below we explain this difference in more detail.

The main distinction between this work and G23 is that we measure a higher effective AGN flare number density, which leads to a higher expected number of matches under the background hypothesis. This difference is mainly driven by two factors. First, in G23 the fraction of matching temporal windows is calculated assuming a mean flare lifetime of 100 days and dividing it by 1000 days, approximately the duration of the observations of ZTF DR5. However, all the 20 AGN flares considered in the analysis peaked between the start of O3 and 200 days after its end, implying the effective duration of the ZTF flare search is 562 days. As such, we calculate for each flare the fraction of matching temporal windows by dividing the width of this window ( $200 \text{ days} - t_g$ ) by 562 days. This leads to a significant difference with respect to the value assumed in G23, since the average value of the rise times,  $t_g$ , is about 17 days. The second factor is a different estimate of the effective total comoving volume probed in the ZTF search. Our estimate ( $V_{\text{ZTF,eff}} = 1.066 \times 10^{11} \text{Mpc}^3$ ) takes into account the non-uniformity of the sky distribution of the ZTF extra-galactic sources and is approximately 1.5 times smaller compared to the ZTF volume used in G23. Taken together these two effects yield an effective source density that is approximately 4.6 times larger than the one used in G23. We find a value of the total localisation volume weighted by  $f_{\text{cover}}$  similar to the ones used in G23, even using updated sky maps ( $1.457 \cdot 10^{11} \text{Mpc}^3$ , that corresponds approximately to 68 per cent of the value used in G23).

It is evident that our analysis only constraints the fraction of GW events in AGN that yield a detectable flare. Several factor can make this counterpart challenging to detect. In order to produce a potentially observable flare not later than 200 days after the GW event, the recoil velocity has to be greater than a value that depends on the physical and geometrical characteristics of the AGN disc (see Equation 5 of G23). At the same time, an increase in the recoil velocity corresponds to a decrease in the Bondi-Hoyle-Lyttleton luminosity (see Equations 3 and 6 of G23). Therefore if the merger remnant travels too fast through the accretion disc, the hypothetical resulting flare will not be possible to detect as it will not significantly exceed the luminosity of the host AGN. On top of these physical factors regarding the observability of the flare caused by a kicked remnant exiting the accretion disc, there is a geometrical one. To be visible from instruments like ZTF, the flare has in fact to happen on the side of the disc that faces Earth, and on average this is expected to be true only in

half of the cases. Finally, in order to be confidently identified as a potential EM counterpart to a GW signal, the flare has to happen in a position in the sky that allows the light-curve to be scanned with several observations in different bands over its lifetime.

Current and future time-domain surveys such as ZTF and the Vera C. Rubin Observatory (Ivezić et al. 2019) are promising tools for the identification of transient EM counterparts of GW events detected by the LVK collaboration. The low number density of events not compatible with regular AGN variability makes them ideal for spatial correlation analyses like the one presented in this work. Current data suggest that there is no correlation with events detected by the LVK interferometers, but updating the posterior distribution of  $f_{\text{flare}}$  with more data, or data more sensitive to lower amplitude flares, could yield better constraints on the relation between mergers of compact objects and AGN flares.

## Acknowledgements

The authors thank Matthew Graham for making the data of the 20 AGN flares mentioned in G23 available. EMR acknowledges support from ERC Grant “VEGA P.”, number 101002511. This research has made use of data or software obtained from the Gravitational Wave Open Science Center ([gwosc.org](http://gwosc.org)), a service of LIGO Laboratory, the LIGO Scientific Collaboration, the Virgo Collaboration, and KAGRA. LIGO Laboratory and Advanced LIGO are funded by the United States National Science Foundation (NSF) as well as the Science and Technology Facilities Council (STFC) of the United Kingdom, the Max-Planck-Society (MPS), and the State of Niedersachsen/Germany for support of the construction of Advanced LIGO and construction and operation of the GEO600 detector. Additional support for Advanced LIGO was provided by the Australian Research Council. Virgo is funded, through the European Gravitational Observatory (EGO), by the French Centre National de Recherche Scientifique (CNRS), the Italian Istituto Nazionale di Fisica Nucleare (INFN) and the Dutch Nikhef, with contributions by institutions from Belgium, Germany, Greece, Hungary, Ireland, Japan, Monaco, Poland, Portugal, Spain. KAGRA is supported by Ministry of Education, Culture, Sports, Science and Technology (MEXT), Japan Society for the Promotion of Science (JSPS) in Japan; National Research Foundation (NRF) and Ministry of Science and ICT (MSIT) in Korea; Academia Sinica (AS) and National Science and Technology Council (NSTC) in Taiwan. *Software:* Numpy ([Harris et al. 2020](#)); Matplotlib ([Hunter 2007](#)); SciPy ([Virtanen et al. 2020](#)); Astropy ([Astropy Collaboration et al. 2013, 2018](#)); BAYESTAR ([Singer & Price 2016](#)).

## Data Availability

The data underlying this article will be shared on reasonable request to the corresponding author.

## Appendix: List of GW events

In Table 4.4 we list the properties of the GW events detected during O3 we used in the analysis presented in this work.

**Table 4.4:** List of GW events used in the analysis presented in this work. For each of them we list the ID, the catalogue it is contained in, the size of its 90 per cent credibility localisation area and volume, the Modified Julian Day of the detection, and the fraction of its 90 per cent credibility level localisation area that has been observed by ZTF at least 20 times in both the g-band and r-band during 200 days following the GW detection, at a galactic latitude  $|b| > 10^\circ$ .

GW ID	Catalogue	A90 [deg $^2$ ]	V90 [Mpc $^3$ ]	MJD	$f_{\text{cover}}$
GW190403_051519	GWTC-2.1	2731	$3.872 \cdot 10^{10}$	58576.2	0.487
GW190408_181802	GWTC-2.1	271	$8.922 \cdot 10^7$	58581.8	0.670
GW190412_053044	GWTC-2.1	25	$1.112 \cdot 10^6$	58585.2	0.875
GW190413_052954	GWTC-2.1	668	$2.017 \cdot 10^9$	58586.2	0.539
GW190413_134308	GWTC-2.1	562	$2.100 \cdot 10^9$	58586.6	0.161
GW190421_213856	GWTC-2.1	1237	$1.729 \cdot 10^9$	58594.9	0.013
GW190425_081805	GWTC-2.1	8728	$7.772 \cdot 10^6$	58598.3	0.537
GW190426_190642	GWTC-2.1	4559	$2.527 \cdot 10^{10}$	58599.8	0.638
GW190503_185404	GWTC-2.1	103	$4.716 \cdot 10^7$	58606.8	0.000
GW190512_180714	GWTC-2.1	274	$9.283 \cdot 10^7$	58615.8	0.250
GW190513_205428	GWTC-2.1	448	$3.805 \cdot 10^8$	58616.9	0.590
GW190514_065416	GWTC-2.1	3186	$1.063 \cdot 10^{10}$	58617.3	0.515
GW190517_055101	GWTC-2.1	365	$3.042 \cdot 10^8$	58620.2	0.222
GW190519_153544	GWTC-2.1	672	$1.180 \cdot 10^9$	58622.6	0.308
GW190521_030229	GWTC-2.1	1021	$3.434 \cdot 10^9$	58624.1	0.500
GW190521_074359	GWTC-2.1	469	$5.611 \cdot 10^7$	58624.3	0.500
GW190527_092055	GWTC-2.1	3640	$7.788 \cdot 10^9$	58630.4	0.473
GW190602_175927	GWTC-2.1	739	$1.412 \cdot 10^9$	58636.7	0.317
GW190620_030421	GWTC-2.1	6443	$1.219 \cdot 10^{10}$	58654.1	0.618

GW ID	catalogue	A90 [deg <sup>2</sup> ]	V90 [Mpc <sup>3</sup> ]	MJD	$f_{\text{cover}}$
GW190630_185205	GWTC-2.1	960	$1.104 \cdot 10^8$	58664.8	0.507
GW190701_203306	GWTC-2.1	43	$3.494 \cdot 10^7$	58665.9	1.000
GW190706_222641	GWTC-2.1	2596	$7.799 \cdot 10^9$	58670.9	0.590
GW190707_093326	GWTC-2.1	893	$6.443 \cdot 10^7$	58671.4	0.098
GW190708_232457	GWTC-2.1	11032	$9.846 \cdot 10^8$	58673.0	0.533
GW190719_215514	GWTC-2.1	3564	$1.317 \cdot 10^{10}$	58683.9	0.612
GW190720_000836	GWTC-2.1	35	$2.303 \cdot 10^6$	58684.0	0.000
GW190725_174728	GWTC-2.1	2142	$3.780 \cdot 10^8$	58689.7	0.386
GW190727_060333	GWTC-2.1	100	$1.963 \cdot 10^8$	58691.3	0.235
GW190728_064510	GWTC-2.1	321	$2.974 \cdot 10^7$	58692.3	0.602
GW190731_140936	GWTC-2.1	3532	$8.919 \cdot 10^9$	58695.6	0.357
GW190803_022701	GWTC-2.1	1012	$2.227 \cdot 10^9$	58698.1	0.684
GW190805_211137	GWTC-2.1	1538	$1.342 \cdot 10^{10}$	58700.9	0.664
GW190814_211039	GWTC-2.1	22	$3.590 \cdot 10^4$	58709.9	0.667
GW190828_063405	GWTC-2.1	340	$2.502 \cdot 10^8$	58723.3	0.205
GW190828_065509	GWTC-2.1	593	$2.700 \cdot 10^8$	58723.3	0.234
GW190910_112807	GWTC-2.1	8305	$5.158 \cdot 10^9$	58736.5	0.394
GW190915_235702	GWTC-2.1	432	$2.417 \cdot 10^8$	58742.0	0.889
GW190916_200658	GWTC-2.1	2368	$1.537 \cdot 10^{10}$	58742.8	0.574
GW190917_114630	GWTC-2.1	1687	$1.096 \cdot 10^8$	58743.5	0.317
GW190924_021846	GWTC-2.1	376	$1.209 \cdot 10^7$	58750.1	0.939
GW190925_232845	GWTC-2.1	876	$9.957 \cdot 10^7$	58752.0	0.232
GW190926_050336	GWTC-2.1	2015	$7.945 \cdot 10^9$	58752.2	0.355
GW190929_012149	GWTC-2.1	1651	$4.851 \cdot 10^9$	58755.1	0.468
GW190930_133541	GWTC-2.1	1493	$1.223 \cdot 10^8$	58756.6	0.223
GW191103_012549	GWTC-3	2171	$2.663 \cdot 10^8$	58790.1	0.692
GW191105_143521	GWTC-3	641	$1.250 \cdot 10^8$	58792.6	0.402
GW191109_010717	GWTC-3	1649	$4.863 \cdot 10^8$	58796.0	0.308
GW191113_071753	GWTC-3	2484	$1.159 \cdot 10^9$	58800.3	0.378
GW191126_115259	GWTC-3	1378	$5.990 \cdot 10^8$	58813.5	0.425
GW191127_050227	GWTC-3	983	$3.588 \cdot 10^9$	58814.2	0.418
GW191129_134029	GWTC-3	856	$5.496 \cdot 10^7$	58816.6	0.436
GW191204_110529	GWTC-3	3380	$3.436 \cdot 10^9$	58821.5	0.449
GW191204_171526	GWTC-3	256	$7.520 \cdot 10^6$	58821.7	0.284
GW191215_223052	GWTC-3	586	$4.535 \cdot 10^8$	58832.9	0.299
GW191216_213338	GWTC-3	206	$1.280 \cdot 10^6$	58833.9	0.282

GW ID	catalogue	A90 [deg <sup>2</sup> ]	V90 [Mpc <sup>3</sup> ]	MJD	$f_{\text{cover}}$
GW191219_163120	GWTC-3	2232	$7.504 \cdot 10^7$	58836.7	0.465
GW191222_033537	GWTC-3	2168	$3.687 \cdot 10^9$	58839.1	0.417
GW191230_180458	GWTC-3	1086	$4.376 \cdot 10^9$	58847.8	0.247
GW200105_162426	GWTC-3	7882	$3.345 \cdot 10^7$	58853.7	0.438
GW200112_155838	GWTC-3	3200	$5.599 \cdot 10^8$	58860.7	0.352
GW200115_042309	GWTC-3	512	$3.792 \cdot 10^6$	58863.2	0.329
GW200128_022011	GWTC-3	2415	$5.729 \cdot 10^9$	58876.1	0.357
GW200129_065458	GWTC-3	31	$2.617 \cdot 10^6$	58877.3	0.857
GW200202_154313	GWTC-3	150	$2.155 \cdot 10^6$	58881.7	0.872
GW200208_130117	GWTC-3	30	$3.075 \cdot 10^7$	58887.5	0.000
GW200208_222617	GWTC-3	2040	$1.214 \cdot 10^{10}$	58887.9	0.397
GW200209_085452	GWTC-3	877	$2.325 \cdot 10^9$	58888.4	0.664
GW200210_092255	GWTC-3	1387	$1.595 \cdot 10^8$	58889.4	0.555
GW200216_220804	GWTC-3	2924	$1.113 \cdot 10^{10}$	58895.9	0.750
GW200219_094415	GWTC-3	781	$1.902 \cdot 10^9$	58898.4	0.435
GW200220_061928	GWTC-3	4477	$4.333 \cdot 10^{10}$	58899.3	0.301
GW200220_124850	GWTC-3	3129	$1.185 \cdot 10^{10}$	58899.5	0.475
GW200224_222234	GWTC-3	42	$1.947 \cdot 10^7$	58903.9	0.143
GW200225_060421	GWTC-3	498	$8.177 \cdot 10^7$	58904.3	0.533
GW200302_015811	GWTC-3	6016	$2.778 \cdot 10^9$	58910.1	0.230
GW200306_093714	GWTC-3	3907	$4.302 \cdot 10^9$	58914.4	0.459
GW200311_115853	GWTC-3	35	$5.799 \cdot 10^6$	58919.5	1.000
GW200316_215756	GWTC-3	187	$3.634 \cdot 10^7$	58924.9	0.217

# 5

## CONSTRAINTS ON THE AGN CHANNEL FOR THE FORMATION OF STELLAR-MASS BINARY BLACK HOLES UP TO Z=1.5 USING THE QUAIA CATALOGUE

Work by **N. Veronesi**, S. van Velzen, E. M. Rossi,  
soon to be submitted to *Monthly Notices of the Royal Astronomical Society*

### Abstract

Statistical analyses based on the spatial correlation between the sky maps of detected Gravitational Wave (GW) events and the positions of potential host environments are a valid tool to answer the open question regarding the physical origin of the binaries of which have the mergers been detected by the interferometers of the LIGO-Virgo-KAGRA (LVK) collaboration. One plausible formation channel involves the interaction between the merging compact objects and the accretion discs that power Active Galactic Nuclei (AGN). In this paper we test the efficiency of this so-called AGN channel by analysing the spatial correlation between 159 GW events detected not later than June 1st, 2024, and the AGN contained in the all-sky catalogue Quaia. To do so, we estimate the bolometric luminosities of all the potential hosts and the completeness of Quaia up to redshift  $z = 1.5$ . We find at a 95 per cent credibility level that un-obscured AGN with a bolometric luminosity higher than  $10^{44.5} \text{erg s}^{-1}$  ( $10^{45} \text{erg s}^{-1}$ ) do not contribute to more than the 21 (11) per cent of the mergers detected by the LVK collaboration. A significant fraction of the detected mergers might still come from categories of AGN that are not included in our analysis, like faint or obscured ones.

## 5.1 Introduction

A consistent one-to-one association between the mergers of compact objects (COs) detected through Gravitational Waves (GWs) by the LIGO-Virgo-KAGRA (LVK) collaboration ([Acernese et al. 2015](#); [LIGO Scientific Collaboration et al. 2015](#); [Akutsu et al. 2021](#)) and their host galaxy is currently out of reach.

This is primarily caused by the typical size of the uncertainties that are associated to the sky position and to the luminosity distance of each GW event. The impossibility of associating each merger to its host environment hampers the chances to answer the open question regarding the physical origin of the binary systems of which the coalescences have been directly measured. Among the possible binary formation scenarios that have been proposed (see [Mapelli 2021](#), for a review), there is one according to which binaries of COs like Binary Black Holes (BBHs), binary Neutron Starts (BNSs), and Neutron Star-Black Hole binaries (NSBHs) can be efficiently assembled and driven to merger in dense environments like Globular Clusters ([Rodriguez et al. 2016](#)) or Nuclear Stellar Clusters ([Chattopadhyay et al. 2023](#)). In such hosts binaries can have their semi-major axes shrunk by interactions with single objects. Single-binary encounters are expected to harden binaries, which is crucial for the formation of systems that are able to merge within a Hubble time due to loss of orbital energy, emitted in the form of GWs. The least massive object of the three is expected to be ejected from the location of the single-binary interaction ([Hills & Fullerton 1980](#); [Ziosi et al. 2014](#)), meaning that the remnant hardened binary will be composed of the two heaviest elements that take part in the encounter.

Another reason why dynamically dense environments might be the hosts of the most massive mergers detected by the LVK collaboration is the fact that their escape velocities can be large enough to retain the recoil-kicked remnant of a merger, turning it into the potential component of a subsequent GW event. This "hierarchical merger" scenario might consist of a physical interpretation for the existence of stellar-mass Black Holes (sBHs) in the Pair-Instability Mass Gap ([Gerosa & Berti 2017, 2019](#); [Yang et al. 2019](#); [Barrera & Bartos 2022](#)). This discontinuity is predicted between  $\approx 50M_{\odot}$  and  $\approx 120M_{\odot}$  in the sBH mass spectrum as a consequence of the complete disruption of the core during the SuperNova event at the end of the life cycle of stars with very high masses, that are therefore expected to leave no remnant ([Heger & Woosley 2002](#); [Belczynski et al. 2016](#)). However, the astrophysical mass distribution of sBHs predicted by the LVK collaboration shows evidence for the presence of objects in the Pair-Instability Mass Gap ([Abbott et al. 2023a](#)). This fact challenges the hypothesis

according to which all the merging systems detected by the LVK collaboration evolved from an isolated stellar binary.

Accretion discs of AGN are a unique type of potential host environment for the assembly and the merger of binaries of COs. This is mainly because in the so-called "AGN formation channel" the binaries and their components are not expected to interact only with other stellar objects, but also with the gas the accretion disc consists of. Thanks to this interaction, the disc might for example capture COs that have orbits moderately inclined with respect to its plane ([Ostriker 1983](#); [Fabj et al. 2020](#); [Nasim et al. 2023](#)). These disc captures have the effect of increasing the number density of COs in the disc, where the binary formation can be gas-assisted ([Tagawa et al. 2020](#); [DeLaurentiis et al. 2023b](#); [Rowan et al. 2023](#)). Another process which, as far as the formation of merging CO binaries is concerned, is typical of the AGN scenario is migration, the radial motion of COs orbiting around the central SuperMassive Black Hole (SMBH). Inward migration takes place in AGN discs where the net torque exerted by the gas onto the orbiting CO is negative ([Paardekooper et al. 2010](#); [Bellovary et al. 2016](#)), and can increase the number density of sBHs and Neutron Stars (NSs) in the inner part of the accretion disc, facilitating the formation of binaries.

One possible way to put constraints on the fractional contribution of the AGN channel to the total merger rate of CO binaries is through the investigation of the spatial correlation between the sky maps of the events detected by the LVK collaboration and the positions of observed AGN. This approach has been first suggested in [Bartos et al. \(2017a\)](#), where it was estimated that 300 GW detections would have been sufficient to be able reject the hypothesis according to which there is no GW-AGN relation in favour of the hypothesis that states that the AGN channel contributes to half of the total merger rate. In [Corley et al. \(2019\)](#) it was later found that the number of needed detections decreases by a factor  $\approx 3$  if it is assumed that the inclination of the binary angular momentum with respect to the line of sight is known with an uncertainty of  $5^\circ$ . In the simulated GW detections used in both [Bartos et al. \(2017a\)](#) and [Corley et al. \(2019\)](#) the interferometers of LIGO and Virgo have been assumed to be working at Design Sensitivity.

In [Veronesi et al. \(2022\)](#) the analysis has been repeated assuming a realistic distribution of the sizes of the 90 per cent localisation volumes (V90) of the simulated GW detections. This distribution has been created from mock detections simulated using the sensitivity curves that characterised the LIGO and Virgo interferometers during their third observing run (O3). It was found that the amount of data collected during O3 was enough to reject the no-connection hypothesis in favour of the one according to which the AGN channel contributes to

half of the total merger rate only in the case in which rare AGN with a number density lower than  $10^{-7}\text{Mpc}^{-3}$  are taken into account.

The first observational constraint on the efficiency of the AGN channel was put using the spatial-correlation approach in Veronesi et al. (2023). The statistical framework of that work consisted in an improved version of the one first suggested for the investigation of the AGN-GW relation in Bartos et al. (2017a), and then used also in Corley et al. (2019) and in Veronesi et al. (2022). In Veronesi et al. (2023) the completeness of the AGN catalogues used during the cross-match with GW sky maps and the exact position of the potential host environments have been taken into account for the first time in this type of analysis. Moreover, in the same work, the value of the fractional contribution of the AGN channel to the total merger rate,  $f_{\text{AGN}}$ , has been constrained for the first time via Likelihood maximisation. Using catalogues of AGN with a spectroscopic estimate of redshift of  $z \leq 0.3$  obtained from Milliquasv7.7b (Flesch 2021) and the sky maps of the 30 GW events detected in the same redshift range during the first three observing runs of the LVK collaboration, it was found that the fraction of the detected mergers that have originated in an AGN more luminous than  $10^{45.5}\text{erg s}^{-1}$  ( $10^{46}\text{erg s}^{-1}$ ) is not expected to be higher than 0.49 (0.17). A similar statistical investigation has been conducted also in (Veronesi et al. 2024). In this case the sky maps of the GW events detected during O3 have been cross-matched spatially and temporally with the 20 unusual AGN flaring activities detected by the Zwicky Transient Facility (ZTF) (Bellm et al. 2019; Graham et al. 2019) that have been identified in Graham et al. (2023) as potential transient ElectroMagnetic counterparts. The estimate of the spatial correlation analysis is that the hypothesis according to which there is no connection between the GW events and unusual flares is the one favoured by data.

In this work we present new observational constraints on  $f_{\text{AGN}}$ . We use a spatial-correlation-based method similar to the one presented in Veronesi et al. (2023), and apply it to a larger dataset. In particular we use the sky maps of all the GW events detected by the interferometers of the LVK collaboration up to June 1st, 2024, therefore including data coming from the fourth observing run (O4). This brings the total number of used sky maps to 159, which is more than five times the amount of GW events used in Veronesi et al. (2023). These are cross-matched with the AGN of Quaia (Storey-Fisher et al. 2024). This all-sky catalogue is the result of a re-analysis of the one containing the objects identified as extra-galactic by the Gaia mission (Gaia Collaboration et al. 2023). The remarkable uniformity and completeness up to  $z = 1.5$  of Quaia make it a valid tool for all-sky spatial correlation analyses like the one presented in this

work.

In Section 5.2 we present the main characteristics of the data used in this work, which include the different GW detections and the Quaia catalogue. In Section 5.3 we then describe the likelihood function that we maximise in order to obtain our new constraints on  $f_{\text{AGN}}$ , which are presented in Section 5.4. Finally, in Section 5.5 we draw the main conclusions regarding the AGN channel that can be inferred from the results of our analysis, and discuss about future developments of statistical spatial-correlation-based approaches. We adopt the cosmological parameters of the Cosmic Microwave Background observations by Planck (Planck Collaboration et al. 2016):  $H_0 = (67.8 \pm 0.9) \text{ km s}^{-1}\text{Mpc}^{-1}$ ,  $\Omega_m = 0.308 \pm 0.012$ , and  $n_s = 0.968 \pm 0.006$ .

## 5.2 Datasets

In this section we first present the main characteristics of the GW events the sky maps of which are used in our analysis. We then describe the main properties of the Quaia catalogue and how we estimate its completeness as a function of redshift for different sub-samples of it, characterised by different thresholds of bolometric luminosity,  $L_{\text{bol}}$ .

### 5.2.1 GW events

In this work we use the 159 sky maps of mergers of CO binaries detected by the interferometers of the LVK collaboration up to June 1st, 2024. In particular all the confident GW events from the first three observing runs are included, with the only exclusion of GW200308\_173609 and of GW200322\_091133. These two events are not taken into consideration because they are poorly localised, and the corresponding value of V90 cannot be estimated from the currently available posterior samples. Moreover, we use all the events from the first half of O4 (O4a) as well as all the events from its second half (O4b) that have been detected not later than June 1st, 2024. For this currently ongoing observing run, we select the detections that have a probability of being of terrestrial origin smaller than 1 per cent.

The sky maps of the events detected during the first three observing runs are downloaded from the Gravitational Wave Open Science Center (GWOSC) (Abbott et al. 2023a). We use the posterior samples obtained using the IMR-PHENOMXPHM waveform model (Pratten et al. 2021) for all these events but

GW190425\_081805, GW191219\_163120, GW200105\_162426, and GW200115\_042309. For these four events we use the MIXED posterior samples.

The sky maps of the 71 events of O4 we use in the analysis presented in this work are downloaded from the Gravitational-Wave Candidate Event Database (GraceDB)<sup>1</sup>, operated by the LIGO Scientific Collaboration. For each event we use the most recent version of its sky map, which is either obtained from the Bilby localisation algorithm (Ashton et al. 2019) or from the Bayestar one (Singer & Price 2016).

Figure 5.1 shows the luminosity distance of all the 159 GW events used in this work as a function of the correspondent value of V90. The median value of the luminosity distance (2012.3 Mpc) and of V90 ( $7.67 \cdot 10^7 \text{Mpc}^3$ ) are indicated by the horizontal dashed line and by the vertical one, respectively.

### 5.2.2 Quaia AGN catalogue

In order to obtain precise estimates of  $f_{\text{AGN}}$  with methods based on spatial correlation like the one used in this work, is important to use an AGN catalogue that has the highest possible value of completeness. This property of a catalogue is in general a function of the redshifts, the sky positions, and the luminosities of the objects that are considered.

In the analyses here presented, the Quaia AGN catalogue (Storey-Fisher et al. 2024) is cross-matched with the sky maps of the GW events described in Section 5.2.1. This is done once the completeness of such a catalogue has been estimated. Quaia is an all-sky catalogue that contains objects identified as extra-galactic in the third data release of the Gaia mission (Gaia Collaboration et al. 2023). The final version of this catalogue is obtained by selecting the objects that have an infrared counterpart in the unWISE catalogue (Lang 2014; Meisner et al. 2019) and by performing cuts in colours and proper motion in order to decrease the amount of contaminants (see Section 3.1 of Storey-Fisher et al. 2024, for details). The result is a catalogue containing 1,295,502 objects with a magnitude in the Gaia G-band  $\text{mag}_G < 20.5$ . The redshifts of these objects are estimated using a  $k$ -Nearest Neighbors model trained on the AGN present in Quaia of which the spectra are in the 16th Data Release (DR16Q) of the Sloan Digital Sky Survey (SDSS) (Lyke et al. 2020).

Figure 5.2 shows the mollweide projection of the sky distribution of the AGN contained in the Quaia catalogue. The colour of each pixel depends on the amount of objects in the correspondent position in the sky. The size of each

---

<sup>1</sup><https://gracedb.ligo.org/>

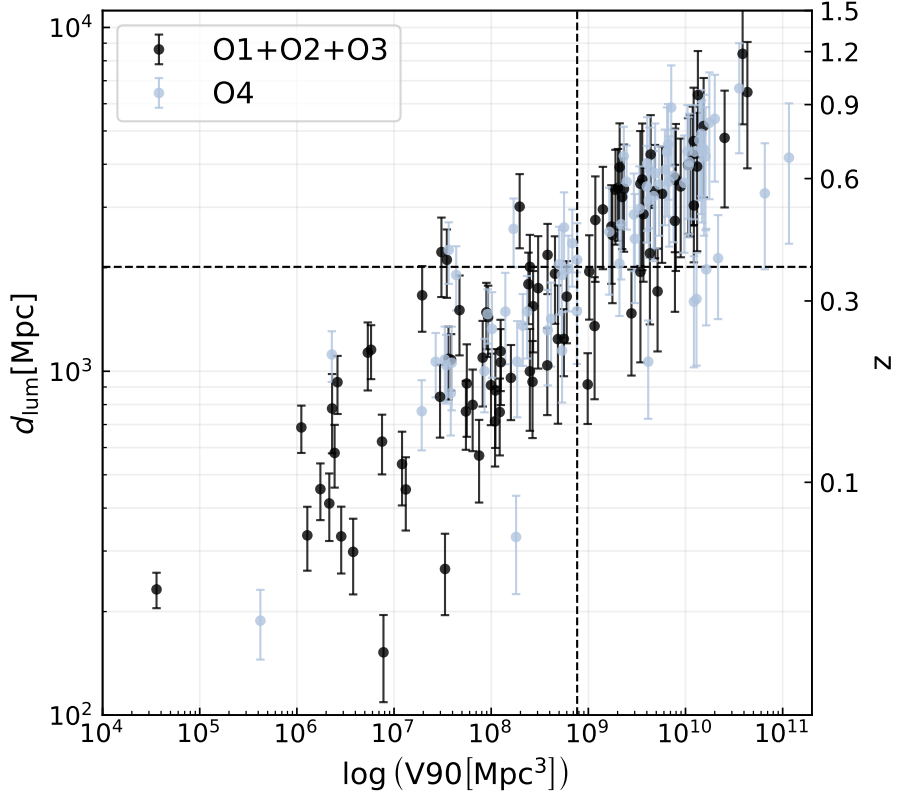


**Figure 5.1:** Luminosity distance as a function of V90 for the 159 GW events used in the analysis presented in this work. The error bars represent an uncertainty of one standard deviation around the mean of the estimated distance. While black markers indicate the mergers detected during the first three observing runs of the LVK collaboration, the light blue ones represent the ones detected during O4, up to June 1st, 2024. The horizontal and the vertical dashed lines mark the median value of the all luminosity distance estimates and of the V90 distribution, respectively. The values reported on the vertical axis on the right-hand side of the panel indicate arbitrarily chosen values of redshift.

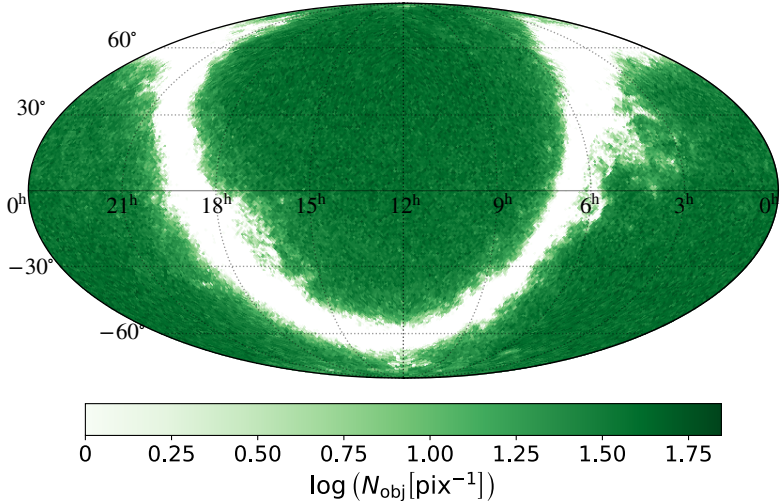


**Figure 5.2:** Mollweide projection of the sky positions of the 1,295,502 objects contained in the Quaia catalogue with a magnitude  $G < 20.5$ . Different shades of green represent different sky-projected number densities. The resolution is the one of an HealPix map with NSIDE=64.

pixel is  $\approx 2.557 \cdot 10^{-4}$  steradians. Its remarkable uniformity outside the region containing the Milky Way galactic plane makes Quaia a valid tool for spatial correlation analyses between AGN and GW events.

The AGN used during the cross-match with the GW sky maps are the 660,031 objects present in Quaia that have a redshift estimate not larger than  $z = 1.5$  and that are in the region of the sky where the galactic latitude  $b$  is either higher than  $10^\circ$  or smaller than  $-10^\circ$ . The redshift selection is performed since all the GW events used in this work are expected to have taken place in the  $0 \leq z \leq 1.5$  range (see Figure 5.1). We choose not to use the objects with a small absolute value of galactic latitude for simplicity. In our analysis in fact we consider the density of objects in the catalogue not to depend on their Right Ascension or Declination, as far as they are outside of the region of the galactic plane. This selection on sky position removes only  $\approx 1.6$  per cent of all the objects within  $z = 1.5$  and is not expected to decrease significantly the constraining power of the analysis presented in this work. We further refer to the catalogue obtained after performing these selections in redshift and in sky

position as Quaia<sub>cut</sub>.

### 5.2.3 Completeness estimation

The likelihood maximisation method presented in this work requires an estimate of the completeness of AGN catalogue that is used. We therefore estimate this property of Quaia<sub>cut</sub> as a function of redshift and luminosity. We do so in three steps:

- Estimation of the bolometric luminosity of each object in Quaia with a redshift estimate not higher than  $z = 1.5$ . This sub-section of Quaia is later referred to as Quaia <sub>$z < 1.5$</sub> . The luminosities are evaluated starting from the Vega magnitudes in the G<sub>RP</sub> band ( $\text{mag}_{\text{G}_{\text{RP}}, \text{VEG}}$ );
- Correction for the host-galaxy contribution to the total luminosity using as reference the AGN with a counterpart in SDSS DR16Q, and the values of their bolometric luminosities presented in [Wu & Shen \(2022\)](#);
- Comparison between the number of objects present in Quaia<sub>cut</sub> in a specific redshift bin and the ones predicted by the AGN luminosity function presented in [Kulkarni et al. \(2019\)](#). This is done five times, considering each time a different threshold in bolometric luminosity.

#### 5.2.3.1 Evaluation of bolometric luminosity from $\text{mag}_{\text{G}_{\text{RP}}, \text{VEG}}$ :

To obtain an estimate of the bolometric luminosity of all the objects contained in Quaia <sub>$z < 1.5$</sub> , we first calculate the flux density in photo-electrons per second using the following standard relation:

$$f_{\nu_{\text{G}_{\text{RP}}}} \left[ \frac{e^-}{s} \right] = 10^{-\frac{m_{\text{G}_{\text{RP}}, \text{VEG}} - \text{ZP}_{\text{RP}, \text{VEG}}}{2.5}} , \quad (5.1)$$

where  $\text{ZP}_{\text{RP}, \text{VEG}} = 24.7479$  is the photometric zero-point in the Vega system for the G<sub>RP</sub> band. The flux density in Jansky is then calculated by multiplying  $f_{\nu} \left[ \frac{e^-}{s} \right]$  by the conversion factor  $c_{\nu} = 3.299 \cdot 10^{-36} \text{Jy} \cdot s/e^-$ . The values of  $\text{ZP}_{\text{RP}, \text{VEG}}$  and of  $c_{\nu}$  are taken from the online documentation regarding the calibration of Gaia data <sup>2</sup>.

---

<sup>2</sup><https://www.cosmos.esa.int/web/gaia-users/archive>

The intrinsic luminosity of each AGN emitted at a rest-frame frequency of  $\nu_{\text{GRP}} = 10^{14.588}\text{Hz}$ <sup>3</sup> is then calculated as follows:

$$\nu_{\text{GRP}} L_{\nu_{\text{GRP}}} = \nu_{\text{GRP}} f_{\nu_{\text{GRP}}} (4\pi d_{\text{lum}}^2) (1+z)^{-0.657} , \quad (5.2)$$

where  $d_{\text{lum}}$  is the luminosity distance correspondent to the redshift  $z$  of each object. The last term of Equation 5.2 is used to take into account the shape of the typical Spectral Energy Distribution (SED) of the objects in Quaia. The value of the exponent is calculated from a linear fit of the mean SED of all SDSS quasars presented in Richards et al. (2006). In particular, in the range between  $\nu_{\text{GRP}}$  and  $(1+z_{\text{max}})\nu_{\text{GRP}}$  (where for Quaia <sub>$z < 1.5$</sub> ,  $z_{\text{max}} = 1.5$ ), we find that:

$$\log(\nu L_{\nu}) \propto \log(\nu) \cdot 0.657 , \quad (5.3)$$

and therefore

$$\nu_{\text{em}} L_{\nu_{\text{em}}} = \nu_{\text{GRP}} L_{\nu_{\text{GRP}}} (1+z)^{0.657} , \quad (5.4)$$

where  $\nu_{\text{em}} L_{\nu_{\text{em}}}$  is the luminosity emitted in the rest-frame frequency that is observed at  $\nu_{\text{GRP}}$ .

The bolometric luminosity is then calculated by multiplying  $\nu_{\text{GRP}} L_{\nu_{\text{GRP}}}$  by the value that the frequency-dependent bolometric correction presented in Richards et al. (2006) has in correspondence of  $\nu_{\text{GRP}}$ . This value is 14.59.

### 5.2.3.2 Comparison with the bolometric luminosity estimates of Wu & Shen (2022)

The bolometric luminosities calculated following the procedure described in Section 5.2.3.1 are not corrected for the contribution of the host galaxies, and they are therefore over-estimated. In order to adjust for this, we correct them through the comparison with the estimates listed in the catalogue presented in Wu & Shen (2022). This catalogue contains continuum and emission-line properties of the 750,414 broad-line Quasars of SDSS DR16Q. Among these properties there is the bolometric luminosity of each AGN, estimated from the continuum luminosity at rest-frame wavelengths of 5100, 3000, and 1350 Å. We perform a cross-match between this catalogue and Quaia <sub>$z < 1.5$</sub> , using two arcsec as the maximum separation on the sky two objects can have in order to be considered as matching. A total of 136,368 matches are found. For each of these AGN is possible to calculate the difference between the logarithm of the bolometric

---

<sup>3</sup>this value has been calculated assuming a fiducial wavelength for the G<sub>RP</sub> band of 7750Å.

**Table 5.1:** Partition of the AGN contained in both Quaia <sub>$z < 1.5$</sub>  and the catalogue presented in Wu & Shen (2022). This partition has been used to compare the estimates of bolometric luminosity. In the Table we list the minimum and the maximum luminosity of each sub-sample. To perform this subdivision we use the luminosity estimates that are obtained starting from mag<sub>G<sub>RP, VEG</sub></sub>. In order to correct these estimates according to the values contained in the catalogue of Wu & Shen (2022), we divide each sub-sample of Quaia <sub>$z < 1.5$</sub>  in linear redshift bins. The number of these bins for each sub-sample and the maximum value of the redshift used in this division, which has been done using the Quaia redshift estimates, are listed in the last two columns of the Table.

$\log(L_{\text{bol},\text{min}} [\text{erg s}^{-1}])$	$\log(L_{\text{bol},\text{max}} [\text{erg s}^{-1}])$	$N_{\text{bins},z}$	$z_{\text{max}}$
46.5	-	4	1.5
46	46.5	5	1.5
45.5	46	8	1.5
45	45.5	9	1.1
-	45	3	0.5

luminosity estimated from mag<sub>G<sub>RP, VEG</sub></sub> and the logarithm of the bolometric luminosity taken from the catalogue of Wu & Shen (2022). The mean value of the distribution of this differences is 0.073, and its standard deviation is 0.213. As expected, the bolometric luminosities obtained from mag<sub>G<sub>RP, VEG</sub></sub> are on average slightly over-estimated. We then proceed to correct this over-estimation.

We divide the AGN that are both in Quaia <sub>$z < 1.5$</sub>  and in the catalogue presented in Wu & Shen (2022) into five bolometric luminosity bins. This partition is performed using the estimates calculated starting from mag<sub>G<sub>RP, VEG</sub></sub>. Each of these sub-samples is then divided in redshift bins, using the Quaia estimate of redshift for each AGN. For each luminosity sub-sample we choose a different number of linear redshift bins and a different value of the maximum redshift to consider, to ensure that in each of these bins there are at least 10 objects. In Table 5.1 we list the minimum and the maximum bolometric luminosity for each of the five sub-samples, the number of redshift bins in which it is divided, and the maximum redshift considered in this division.

For each bin in luminosity and redshift, we perform a linear fit between the logarithm of the bolometric luminosities estimated starting from mag<sub>G<sub>RP, VEG</sub></sub>, and the bolometric luminosities taken from the catalogue of Wu & Shen (2022). We therefore obtain one set of best-fit parameters for each bin in luminosity and redshift. We finally use these best-fit parameters to correct the bolometric luminosity of each object contained in Quaia<sub>cut</sub> that was estimated from

$\text{mag}_{\text{G}_{\text{RP, VEG}}}$ . These adjusted estimates are the ones used in the rest of the analysis presented in this paper.

### 5.2.3.3 Comparison with the AGN luminosity function of [Kulkarni et al. \(2019\)](#)

In order to have an estimate of the completeness of  $\text{Quaia}_{\text{cut}}$  as a function of redshift we compare the number of objects it contains with the expectation value calculated from the AGN luminosity function presented in [Kulkarni et al. \(2019\)](#). In particular we use the best-fit double power law function in which the parameters evolve as a function of redshift according to Model 1 (for the analytical expression see Equations 7, 13, 16, 17, and 18 of [Kulkarni et al. 2019](#), while the best-fit parameters are listed in the first column of Table 3 of the same paper).

We compare the observed number of AGN with the predicted one for five different sub-samples of  $\text{Quaia}_{\text{cut}}$ . Each of these sub-samples is characterised uniquely by a different threshold in bolometric luminosity. We divide each sub-sample into 8 linear redshift bins between  $z = 0$  and  $z = 1.5$ . The expected number of objects in each of these bins is calculated integrating the luminosity function of [Kulkarni et al. \(2019\)](#) in the proper range of redshift for each value of luminosity threshold used also in the subdivision of  $\text{Quaia}_{\text{cut}}$ . During the integration, in order to convert the absolute monochromatic AB magnitudes at a rest frame of 1450Å, in terms of which the luminosity function is expressed, into bolometric luminosities, we use the bolometric correction presented in [Runnoe et al. \(2012\)](#).

The dashed lines in Figure 5.3 show the number of expected AGN in all the different redshift bins, obtained through the integration of the luminosity function. Different colours correspond to different bolometric luminosity thresholds. The round markers correspond to the number of objects brighter than the same threshold luminosities that are contained in  $\text{Quaia}_{\text{cut}}$  in the different redshift bins, divided by  $1 - \sin(10^\circ)$  to take into account that the objects in the catalogue are not distributed over the entirety of the sky area. The crosses show the number of objects in SDSS DR16 for each redshift bin and luminosity threshold, divided by  $A_{\text{SDSS}}/A_{\text{sky}}$ , where  $A_{\text{SDSS}} = 9376 \text{ deg}^2$  is the area of the footprint of SDSS, and  $A_{\text{sky}} = 41,253 \text{ deg}^2$  is the total area of the sky. We take the bolometric luminosities of the AGN in the SDSS DR16Q from the catalogue presented in [Wu & Shen \(2022\)](#).

Finally, the completeness of  $\text{Quaia}_{\text{cut}}$  for each redshift bin and for each different cut in bolometric luminosity is calculated dividing the sky-area-corrected

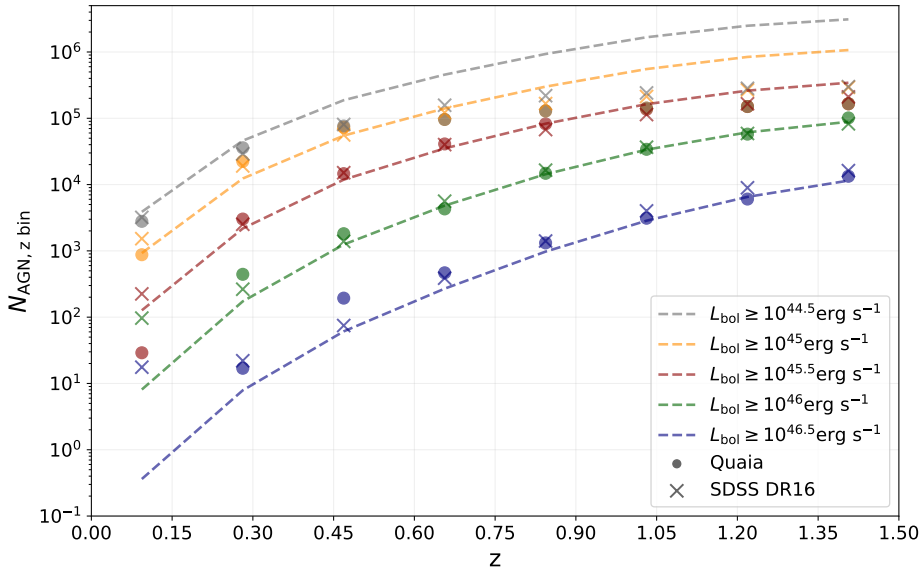


**Figure 5.3:** Comparison between the expected number of AGN in specific redshift bins as a function of different bolometric luminosity thresholds (dashed lines) and the observed number of objects contained in  $\text{Quaia}_{\text{cut}}$  (round markers) and in SDSS DR16 (cross markers). The expected numbers have been calculated integrating the redshift-evolving luminosity function presented in Kulkarni et al. (2019). Only the objects that have an absolute value of galactic latitude greater than  $10^\circ$  are in  $\text{Quaia}_{\text{cut}}$ , and the area of the SDSS footprint is  $\approx 22.7$  per cent of the entire sky area. The plotted numbers of observed AGN have been renormalized according to this.

number of observed AGN by the expected one. Whenever the former is greater than the latter, the completeness is set to one. Because of the selection in galactic latitude Quaia<sub>cut</sub> is obtained from, its completeness in the region where  $|b| < 10^\circ$  is zero. The values of the estimated completeness for all the different redshift bins and the different bolometric luminosity thresholds we consider in our analysis are listed in Table 5.2.

### 5.3 Method

Once the bolometric luminosity has been calculated for each AGN of Quaia<sub>cut</sub> and the completeness of such a catalogue has been estimated as a function of redshift and luminosity, we calculate the posterior on  $f_{\text{AGN}}$ . To do so, we use a likelihood function similar to the ones used in Veronesi et al. (2023) and in Veronesi et al. (2024). The general analytical expression of this function is the following:

$$\begin{aligned} \mathcal{L}(f_{\text{AGN}}) &= \prod_{i=1}^{N_{\text{GW}}} \mathcal{L}_i(f_{\text{AGN}}) \\ &= \prod_{i=1}^{N_{\text{GW}}} [c_i \cdot 0.90 \cdot f_{\text{AGN}} \cdot \mathcal{S}_i + (1 - c_i \cdot 0.90 \cdot f_{\text{AGN}}) \mathcal{B}_i] , \end{aligned} \quad (5.5)$$

where  $N_{\text{GW}} = 159$  is the total number of mergers of binaries of COs we consider in the analysis, and  $c_i$  is the average completeness of Quaia<sub>cut</sub> in the region occupied by  $V90_i$ , the 90 per cent localisation volume of the  $i$ -th GW event. Each value of  $c_i$  has been calculated assuming a null completeness in the region of the sky where  $|b| < 10^\circ$ .

For every GW event we calculate one value of  $c_i$  for each different bolometric luminosity threshold we use in our analysis. Figure 5.4 show the Cumulative Distribution Function (CDF) of  $c_i$  for all these different sub-samples of Quaia<sub>cut</sub>. Different colours indicate different luminosity thresholds. The sub-samples of Quaia<sub>cut</sub> created with a threshold luminosity of  $10^{46} \text{ erg s}^{-1}$  and of  $10^{46.5} \text{ erg s}^{-1}$ , and that therefore contain only the most luminous and rarest AGN, have a null completeness at low redshift. This is the reason why for  $\approx 10$  per cent of the GW events,  $c_i = 0$  when those two catalogues are considered.

In Equation 5.5,  $\mathcal{S}_i$  is the signal probability density and is calculated as

**Table 5.2:** Estimated completeness of Quiaia<sub>cut</sub> in the region of the sky with a galactic latitude greater than  $10^\circ$  or smaller than  $-10^\circ$ . All the values are between 0 and 1, rounded up to the third decimal digit, and are listed for 8 different linear redshift bins as a function of 5 different bolometric luminosity thresholds.

	$\log(L_{\text{bol}} \text{ [erg s}^{-1}\text{]}) \geq 46.5$	$\log(L_{\text{bol}} \text{ [erg s}^{-1}\text{]}) \geq 46.0$	$\log(L_{\text{bol}} \text{ [erg s}^{-1}\text{]}) \geq 45.5$	$\log(L_{\text{bol}} \text{ [erg s}^{-1}\text{]}) \geq 45$	$\log(L_{\text{bol}} \text{ [erg s}^{-1}\text{]}) \geq 44.5$
0.0000 < $z \leq 0.1875$	0	0	0.229	0.945	0.718
0.1875 < $z \leq 0.3750$	1	1	1	1	0.781
0.3750 < $z \leq 0.5625$	1	1	1	1	0.408
0.5625 < $z \leq 0.7500$	1	0.891	1	1	0.681
0.7500 < $z \leq 0.9375$	1	1	0.994	0.429	0.211
0.9375 < $z \leq 1.1250$	1	1	0.837	0.258	0.138
1.1250 < $z \leq 1.3125$	0.927	0.940	0.576	0.179	0.085
1.3125 < $z \leq 1.5000$	1	1	0.482	0.155	0.060
				0.053	

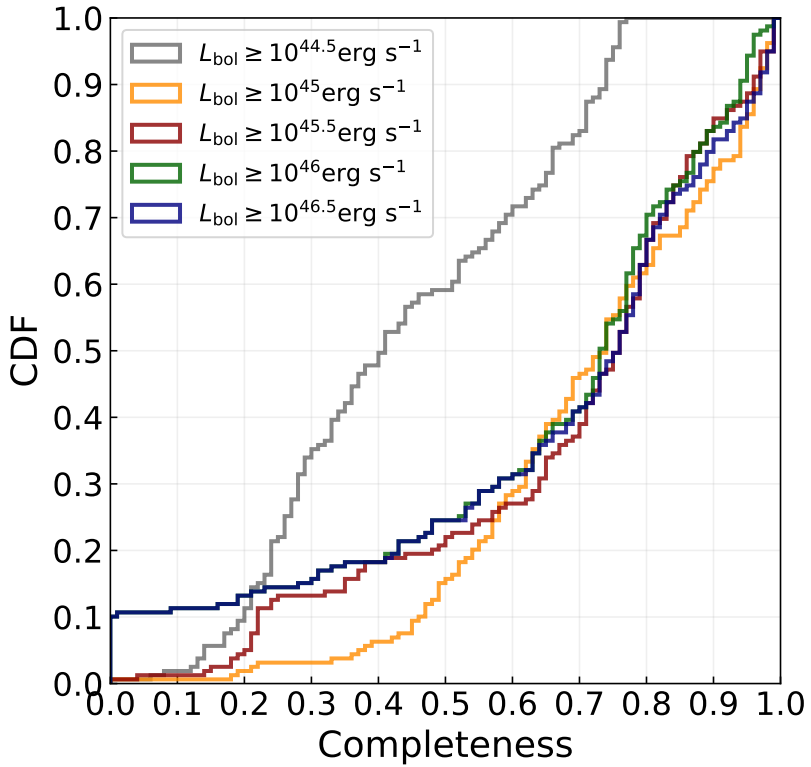


**Figure 5.4:** CDF of the values of average completeness of Quaia<sub>cut</sub> in the region contained within the 90 per cent Credibility Level localisation volume of each of the 159 GW events used in this work. Different colours correspond to different sub-samples of the catalogue. Each of these sub-samples is uniquely characterised by a different value of bolometric luminosity threshold.

follows:

$$\mathcal{S}_i = \frac{1}{V90_i} \sum_{j=1}^{N_{\text{AGN}, V90_i}} \frac{p_j}{n_{\text{AGN}, j}} , \quad (5.6)$$

where  $N_{\text{AGN}, V90_i}$  is the number of AGN located within  $V90_i$ ,  $p_j$  is measured in  $\text{Mpc}^{-3}$  and is the probability density representing how likely it is that the  $i$ -th GW event has happened in the exact position of the  $j$ -th AGN. Finally,  $n_{\text{AGN}, j}$  is the number density of the AGN catalogue in the redshift bin where the  $j$ -th AGN is. The value of this number density for each AGN has been obtained by dividing the total number of objects in the redshift bin it is by the comoving volume enclosed in such a bin, excluding the region in which  $|b| < 10^\circ$ . This has been done for each of the sub-samples of Quaia<sub>cut</sub>, separately.

The background probability density is calculated as follows:

$$\mathcal{B}_i = \frac{0.9}{V90_i} , \quad (5.7)$$

where, in analogy to what has been done in Veronesi et al. (2023) and in Veronesi et al. (2024), the 0.9 factor ensures that  $\mathcal{B}_i$  and  $\mathcal{S}_i$  have the same normalisation.

We cross-match the sky maps of the 159 GW events with the 5 different sub-samples of Quaia<sub>cut</sub> separately, using the `postprocess.crossmatch` function of the package `ligo.skymap`. The results of these cross-matches are used to evaluate  $\mathcal{L}(f_{\text{AGN}})$  using Equation 5.5. We then calculate the posterior probability distribution  $\mathcal{P}_{f_{\text{AGN}}}$ , normalising the likelihood function and assuming a uniform prior on  $f_{\text{AGN}}$  in the  $[0, 1]$  range.

## 5.4 Results

The posterior probability on  $f_{\text{AGN}}$  peaks at  $\hat{f}_{\text{AGN}} = 0$  independently on which sub-set of Quaia<sub>cut</sub> we consider. In Figure 5.5 is shown in blue the region of the parameter space investigated in this work that our analysis rejects with a credibility of 95 per cent. We show the comparison with previous results, obtained in Veronesi et al. (2023) using a more limited dataset.

In Table 5.3 we list, as a function of the threshold on bolometric luminosity, how many objects are considered during the cross-match, what fraction of Quaia<sub>cut</sub> they consist of, and the upper limits we put on  $f_{\text{AGN}}$  at 68, 90, and 95 per cent credibility.

Figure 5.6 shows the logarithm of the ratio between the single-event likelihoods ( $\mathcal{L}_i$ ) calculated at  $f_{\text{AGN}} = 1$  and the ones calculated at  $f_{\text{AGN}} = 0$ , as a

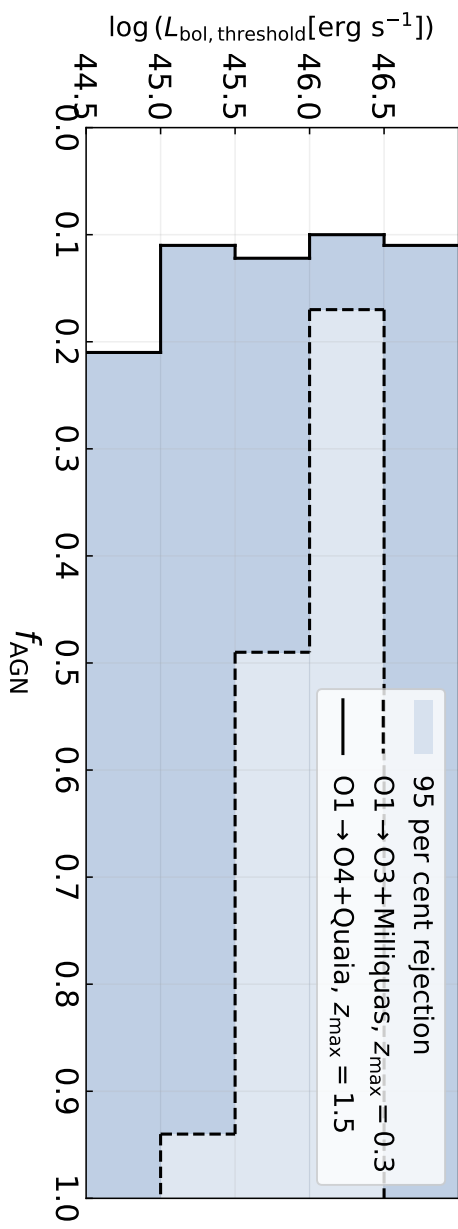


**Figure 5.5:** Observational constraints on  $f_{\text{AGN}}$  based on spatial correlation. The blue region of the plot shows the part of the parameter space we investigated that is rejected by our analysis at a 95 per cent credibility level. The region enclosed in the dashed line shows the results obtained with a more limited dataset in Veronesi et al. (2023). Such previous work used the 30 GW events detected in the first three observing runs of the LVK collaboration that are located within  $z = 0.3$  at a 90 per cent credibility level, and three different catalogues of AGN in the same redshift range. The region enclosed in the solid line shows the results of this work, which explores a wider range of AGN luminosities and uses all the mergers of binaries of COs directly detected up until June 1st, 2024.

**Table 5.3:** Upper limits on  $f_{\text{AGN}}$  we obtain at different levels of credibility, for the three cuts in bolometric luminosity we consider. For each of such cuts we also list the number of AGN used in the analysis ( $N_{\text{AGN, cut}}$ ), and what fraction of the total number of AGN ( $N_{\text{AGN}}$ ,  $\text{Qua}_{\text{cut}}$ ) they consist of. All the values in this table have been rounded up to the second decimal digit.

$\log(L_{\text{bol,threshold}} [\text{erg s}^{-1}])$	$N_{\text{AGN, cut}}$	$N_{\text{AGN, cut}}/N_{\text{AGN}}$ , $\text{Qua}_{\text{cut}}$	68 per cent upper limit	90 per cent upper limit	95 per cent upper limit
46.5	20,236	0.03	0.05	0.09	0.11
46	177,117	0.27	0.04	0.08	0.10
45.5	490,628	0.74	0.05	0.10	0.13
45	644,393	0.98	0.05	0.09	0.11
44.5	659,949	1.00	0.08	0.16	0.21

function of V90;. Different panels correspond to different bolometric luminosity thresholds. In each plot the markers are coloured according to the average completeness inside the localisation volume of the corresponding merger. The dashed horizontal lines indicate where the logarithm has a null value, therefore where  $\mathcal{L}_i(f_{\text{AGN}} = 1) = \mathcal{L}_i(f_{\text{AGN}} = 0)$ . The markers above these lines correspond to GW events according to which the hypothesis of random-chance association between mergers and AGN is disfavoured.

One event in particular, detected during the second half of O4, has a correspondent value of  $\mathcal{L}_i(f_{\text{AGN}} = 1) / \mathcal{L}_i(f_{\text{AGN}} = 0)$  which is greater than one, independently on the luminosity cut of the Quaia sub-sample it is cross-matched with. The ID of such event is S240511i, and the corresponding marker is particularly evident in the first two panels of Figure 5.5. In the case of the cross-match with the sub-sample of Quaia<sub>cut</sub> characterised by AGN brighter than  $10^{46.5} \text{ erg s}^{-1}$  ( $10^{46} \text{ erg s}^{-1}$ ), for this particular GW event  $\log(\mathcal{L}_i(f_{\text{AGN}} = 1) / \mathcal{L}_i(f_{\text{AGN}} = 0)) \approx 1.32$  (0.72), which means that the value of the single-event likelihood calculated at  $f_{\text{AGN}} = 1$  is  $\approx 21$  (5) times larger than the one at  $f_{\text{AGN}} = 0$ . This result based solely on spatial correlation hints towards a possible AGN origin of such event. Further follow-up analyses regarding this merger and its intrinsic binary properties will be needed to be able to draw any definitive conclusion.

## 5.5 Discussion and conclusion

In this work we present new observational constraints on the fractional contribution of the AGN channel to the total observed merger rate of binaries of COs. These constraints are obtained using the same spatial-correlation-based approach used in Veronesi et al. (2023). With respect to our previous work, we make use of a new, larger dataset, which consists of 159 GW events detected by the interferometers of the LVK collaboration not later than June 1st, 2024 and of the all-sky AGN catalogue Quaia. In particular we use all the AGN contained in such a catalogue that have a redshift estimate not larger than  $z = 1.5$  and an absolute value of the galactic latitude  $|b| \geq 10^\circ$ . We call this sub-sample Quaia<sub>cut</sub>.

We estimate the bolometric luminosity of every object in Quaia<sub>cut</sub> using the magnitudes in the Gaia G<sub>RP</sub> band. We also estimate the completeness of such a catalogue as a function of redshift for different values of bolometric luminosity threshold. The average value of the completeness within the 90 per cent Credibility Level localisation volume of each GW event is used during the

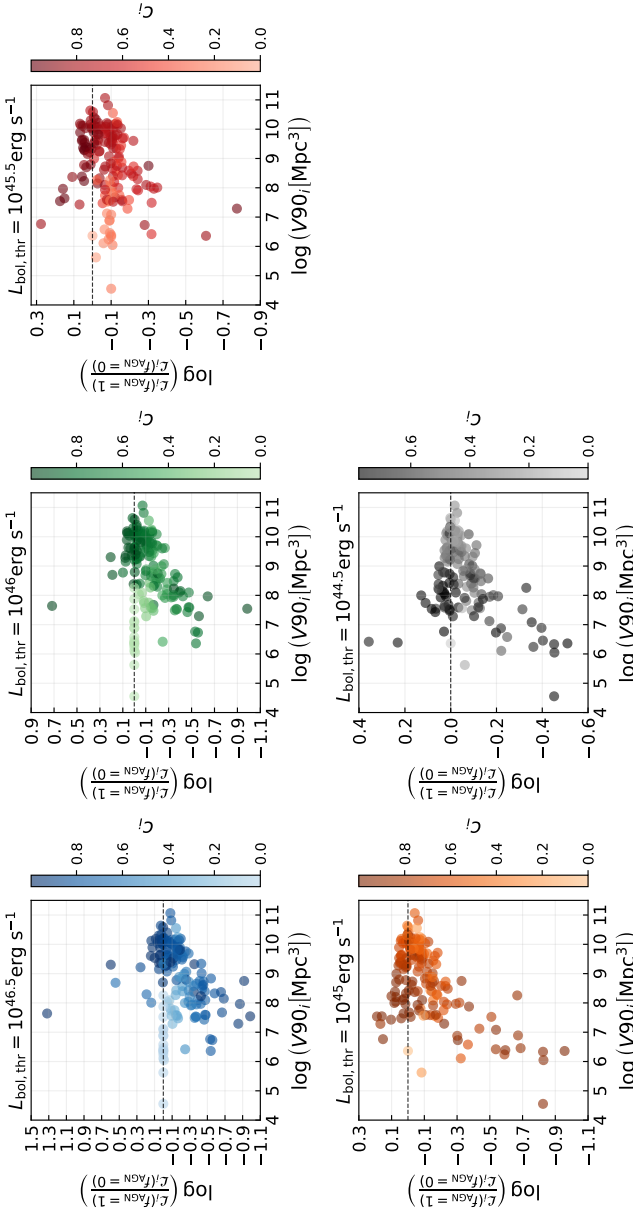


**Figure 5.6:** Logarithm of the ratio between the value of the likelihood at  $f_{\text{AGN}} = 1$  and the one at  $f_{\text{AGN}} = 0$  for each GW event, as a function of the corresponding  $V90$ . Each panel shows the results for a different bolometric luminosity threshold. In each plot, the markers are coloured as a function of the average completeness of Quaiacut in the region occupied by  $V90$ . The dashed horizontal lines mark where  $\mathcal{L}_i(f_{\text{AGN}}=1) = \mathcal{L}_i(f_{\text{AGN}}=0)$ .

likelihood maximisation process.

We calculate the posterior probability function on the fractional contribution of the AGN channel to the total merger rate for all the different luminosity thresholds, obtaining that this function always peaks at  $\hat{f}_{\text{AGN}} = 0$ . We calculate the upper limits of the 68, 90, and 95 per cent Credibility Intervals on  $f_{\text{AGN}}$ . The main results of this work are summarised in Figure 5.5 and in Table 5.3. In particular we estimate that no more than the 21 per cent of the detected GW events used in our analysis originated from an AGN with a bolometric luminosity higher than  $10^{44.5} \text{ erg s}^{-1}$  with 95 per cent credibility. Objects brighter than such threshold consist of almost the entirety of the catalogue we consider. Due to the flux limitations of Quaia, fainter objects are not included in our analysis.

We find a particular GW event for which our analysis suggests a possible AGN origin, especially when objects brighter than  $10^{46} \text{ erg s}^{-1}$  are considered. The ID of such event is S240511i, and it has been detected during O4b. Since the statistical framework used in this work is focused on analysing the entire population of GW events, the results concerning this specific event are to be considered as hints, not as statistically significant conclusions. Follow-up analyses, conducted especially when the full catalogue of mergers detected during O4 will be published, will be necessary to confidently assess whether or not this merger has an AGN origin.

Thanks to the increase of a factor  $\approx 5$  in the number of used GW events with respect to Veronesi et al. (2023) we are able to put much tighter constraints on the efficiency of the AGN channel (see Figure 5.5 for a comparison with our previous work). However, our results have been obtained under some assumptions, which are inevitable when inferring the properties of AGN in large catalogues. First and foremost, in order to calculate the bolometric luminosities of the Objects of Quaia we have to assume a shape of the typical SED and a value for the bolometric correction. We take the values of these AGN properties from Richards et al. (2006) in order to be consistent with what has been done in Wu & Shen (2022), which we use to adjust the bolometric luminosities obtained from Gaia magnitudes. Different assumptions on the SED and on the bolometric correction might lead to different estimates of the bolometric luminosities, even if these differences are not expected to be large enough to be significant for our statistical analysis.

One more assumption is to be made during the calculation of the completeness of Quaia<sub>cut</sub>. This is in fact done comparing the observed number of AGN with the expected one, which is obtained from the integration of a luminosity function. The best fit parameters of these functions depend on the data used during the fit, and different works might assume different analytical expressions

for them. We choose to use the luminosity function presented in [Kulkarni et al. \(2019\)](#) because in the redshift range considered in our analysis it has been fitted on AGN from SDSS, which is a survey that contains un-obsured AGN detectable in the optical band, like the ones contained in Quaia. Moreover, the objects contained in [Wu & Shen \(2022\)](#), used to obtain the final estimate on the bolometric luminosity of the objects in  $\text{Quaia}_{\text{cut}}$ , come from SDSS. Comparing the measured number of objects in our AGN catalogue with a different luminosity function might lead to different estimates of its completeness, and the constraining power presented in this work is expected to scale linearly with such a parameter.

Another important caveat to mention is that our analysis and the constraints we are able to put concern un-obsured AGN, which are visible both in the optical and in the infrared band. In order to extend our conclusions to the entire population of AGN, one should take into account what fraction of them is not visible in the wavelength observed by Gaia and by WISE, which are the two surveys from which Quaia has been created from. This obscuration fraction is in general expected to increase as a function of redshift and to decrease as a function of luminosity ([Merloni et al. 2014](#); [Ueda et al. 2014](#)).

The observational constraints presented in this work consist of a generalisation of the ones obtained in [Veronesi et al. \(2023\)](#). Here we investigate a wider range of AGN luminosities and the entirety of the redshift range reached by the interferometers of the LVK collaboration. For this reason, in order to obtain in the future even more general results one will need an all-sky AGN catalogue with a lower threshold in flux with respect to Quaia, to be able to extend the analysis to the faint-end of the un-obsured AGN population. We estimate that no more than one GW event out of five has originated in an un-obsured AGN with a bolometric luminosity higher than  $10^{44.5} \text{ erg s}^{-1}$ , but a more significant fraction might still come from fainter objects, or from obscured ones.

While the results of this work demonstrate that the efficiency of the AGN channel can already be investigated with spatial-correlation analyses using the currently available data, in the next years it will be possible to put even tighter constraints using all the events that will be detected in the rest of O4 as well as the ones that will be detected during the fifth observing run of the LVK collaboration, O5. Using more data could either reduce the upper limits on  $f_{\text{AGN}}$ , or it could cause a shifting of the value of such parameter that maximised the posterior distribution, moving it away from zero.

Future developments of the statistical method used in this work involve also the introduction of physically-motivate priors on the intrinsic binary properties. Different binary formation channels are indeed expected to produce different

features in the distributions of the masses and the spins of the merging systems, as well as on their eccentricity. The analysis here presented has been kept purposely agnostic as far as the physics of the formation mechanism is concerned. Introducing physically-motivated changes in the likelihood function might result in different constraints on  $f_{\text{AGN}}$  and will inform us on which are the intrinsic binary parameters that are able to add more information to the analysis.

## Acknowledgements

EMR acknowledges support from ERC Grant “VEGA P.”, number 101002511. This research has made use of data or software obtained from the Gravitational Wave Open Science Center ([gwosc.org](http://gwosc.org)), a service of LIGO Laboratory, the LIGO Scientific Collaboration, the Virgo Collaboration, and KAGRA. LIGO Laboratory and Advanced LIGO are funded by the United States National Science Foundation (NSF) as well as the Science and Technology Facilities Council (STFC) of the United Kingdom, the Max-Planck-Society (MPS), and the State of Niedersachsen/Germany for support of the construction of Advanced LIGO and construction and operation of the GEO600 detector. Additional support for Advanced LIGO was provided by the Australian Research Council. Virgo is funded, through the European Gravitational Observatory (EGO), by the French Centre National de Recherche Scientifique (CNRS), the Italian Istituto Nazionale di Fisica Nucleare (INFN) and the Dutch Nikhef, with contributions by institutions from Belgium, Germany, Greece, Hungary, Ireland, Japan, Monaco, Poland, Portugal, Spain. KAGRA is supported by Ministry of Education, Culture, Sports, Science and Technology (MEXT), Japan Society for the Promotion of Science (JSPS) in Japan; National Research Foundation (NRF) and Ministry of Science and ICT (MSIT) in Korea; Academia Sinica (AS) and National Science and Technology Council (NSTC) in Taiwan. *Software:* Numpy ([Harris et al. 2020](#)); Matplotlib ([Hunter 2007](#)); SciPy ([Virtanen et al. 2020](#)); Astropy ([Astropy Collaboration et al. 2013, 2018](#)); Bilby ([Ashton et al. 2019](#)); BAYESTAR ([Singer & Price 2016](#)); Healpy ([Zonca et al. 2019](#)).

## Data Availability

The data underlying this article will be shared on reasonable request to the corresponding author.

# BIBLIOGRAPHY

- Aarseth S. J., Heggie D. C., 1976, A&A, 53, 259
- Abbott B. P., et al., 2016, Phys. Rev. Lett., 116, 061102
- Abbott B. P., et al., 2017, Physical Review Letters, 119, 161101
- Abbott B. P., et al., 2018, Living Reviews in Relativity, 21, 3
- Abbott B. P., et al., 2019, Physical Review X, 9, 031040
- Abbott B. P., et al., 2020, Living Reviews in Relativity, 23, 3
- Abbott R., et al., 2021a, Physical Review X, 11, 021053
- Abbott R., et al., 2021b, SoftwareX, 13, 100658
- Abbott R., et al., 2021c, ApJ, 913, L7
- Abbott R., et al., 2023a, Physical Review X, 13, 041039
- Abbott R., et al., 2023b, ApJS, 267, 29
- Abbott R., et al., 2024, Physical Review D, 109, 022001
- Abdurro'uf et al., 2022, ApJS, 259, 35
- Acernese F., et al., 2015, Classical and Quantum Gravity, 32, 024001
- Ahumada R., et al., 2020, ApJS, 249, 3
- Ajith P., et al., 2011, Phys. Rev. Lett., 106, 241101
- Akutsu T., et al., 2021, Progress of Theoretical and Experimental Physics, 2021, 05A101
- Alfradique V., et al., 2024, MNRAS, 528, 3249
- Amaro-Seoane P., et al., 2017, arXiv e-prints, p. arXiv:1702.00786
- Antoni A., MacLeod M., Ramirez-Ruiz E., 2019, ApJ, 884, 22
- Antonini F., Rasio F. A., 2016, ApJ, 831, 187
- Antonini F., Gieles M., Gualandris A., 2019, MNRAS, 486, 5008
- Armitage P. J., 2007, arXiv e-prints, pp astro-ph/0701485
- Armitage P. J., 2010, Astrophysics of Planet Formation
- Ashton G., et al., 2019, Astrophys. J. Suppl., 241, 27
- Ashton G., Ackley K., Hernandez I. M., Piotrzkowski B., 2021, Classical and Quantum Gravity, 38, 235004
- Aso Y., Michimura Y., Somiya K., Ando M., Miyakawa O., Sekiguchi T., Tatsumi D., Yamamoto H., 2013, Physical Reviews D, 88, 043007
- Assef R. J., et al., 2013, ApJ, 772, 26
- Astropy Collaboration et al., 2013, A&A, 558, A33
- Astropy Collaboration et al., 2018, AJ, 156, 123
- Barrera O., Bartos I., 2022, ApJ, 929, L1
- Bartos I., 2016a, in American Astronomical Society Meeting Abstracts #228. p. 208.03

- Bartos I., 2016b, in American Astronomical Society Meeting Abstracts #228. p. 208.03
- Bartos I., Haiman Z., Marka Z., Metzger B. D., Stone N. C., Marka S., 2017a, *Nature Communications*, **8**, 831
- Bartos I., Kocsis B., Haiman Z., Márka S., 2017b, *ApJ*, **835**, 165
- Bekenstein J. D., 1973, *ApJ*, **183**, 657
- Bekki K., Couch W. J., Shiota Y., Vazdekis A., 2005, *MNRAS*, **359**, 949
- Belczynski K., et al., 2016, *A&A*, **594**, A97
- Belczynski K., Doctor Z., Zevin M., Olejak A., Banerje S., Chattopadhyay D., 2022, *ApJ*, **935**, 126
- Bellm E. C., et al., 2019, *PASP*, **131**, 018002
- Bellovary J. M., Mac Low M.-M., McKernan B., Ford K. E. S., 2016, *ApJ*, **819**, L17
- Binney J., Tremaine S., 2008, Galactic Dynamics: Second Edition
- Blanton M. R., et al., 2017, *AJ*, **154**, 28
- Bonnor W. B., Rotenberg M. A., 1961, *Proceedings of the Royal Society of London Series A*, **265**, 109
- Bowyer S., Byram E. T., Chubb T. A., Friedman H., 1965, *Science*, **147**, 394
- Braun J., Dumm J., De Palma F., Finley C., Karle A., Montaruli T., 2008, *Astroparticle Physics*, **29**, 299
- Calcino J., Dempsey A. M., Dittmann A. J., Li H., 2023, *arXiv e-prints*, p. arXiv:2311.13727
- Callister T. A., Haster C.-J., Ng K. K. Y., Vitale S., Farr W. M., 2021, *ApJ*, **922**, L5
- Campanelli M., Lousto C. O., Zlochower Y., Merritt D., 2007, *Phys. Rev. Lett.*, **98**, 231102
- Chandrasekhar S., 1943, *ApJ*, **97**, 255
- Chattopadhyay D., Stegmann J., Antonini F., Barber J., Romero-Shaw I. M., 2023, *MNRAS*, **526**, 4908
- Chen K., Dai Z.-G., 2024, *ApJ*, **961**, 206
- Colless M., et al., 2001, *MNRAS*, **328**, 1039
- Corley K. R., et al., 2019, *MNRAS*, **488**, 4459
- Costa G., Bressan A., Mapelli M., Marigo P., Iorio G., Spera M., 2021, *MNRAS*, **501**, 4514
- DeLaurentiis S., Epstein-Martin M., Haiman Z., 2023a, in AAS/High Energy Astrophysics Division. p. 100.30
- DeLaurentiis S., Epstein-Martin M., Haiman Z., 2023b, *MNRAS*, **523**, 1126
- Dominik M., Belczynski K., Fryer C., Holz D. E., Berti E., Bulik T., Mandel I., O'Shaughnessy R., 2012, *ApJ*, **759**, 52

- Einstein A., 1915, Sitzungsberichte der Königlich Preußischen Akademie der Wissenschaften, pp 844–847
- El-Badry K., et al., 2023a, *MNRAS*, **518**, 1057
- El-Badry K., et al., 2023b, *MNRAS*, **521**, 4323
- Fabj G., Samsing J., 2024, arXiv e-prints, p. arXiv:2402.16948
- Fabj G., Nasim S. S., Caban F., Ford K. E. S., McKernan B., Bellovary J. M., 2020, *MNRAS*, **499**, 2608
- Farag E., Renzo M., Farmer R., Chidester M. T., Timmes F. X., 2022, *ApJ*, **937**, 112
- Farmer R., Renzo M., de Mink S. E., Marchant P., Justham S., 2019, *ApJ*, **887**, 53
- Ferrarese L., et al., 2006, *ApJ*, **644**, L21
- Fishbach M., Kimball C., Kalogera V., 2022, *ApJ*, **935**, L26
- Flesch E. W., 2021, VizieR Online Data Catalog, p. VII/290
- Flesch E. W., 2023, *The Open Journal of Astrophysics*, **6**, 49
- Ford K. E. S., McKernan B., 2022, *MNRAS*, **517**, 5827
- Ford K. E. S., et al., 2019, *Bulletin of the AAS*, **51**, 247
- Fraley G. S., 1967, PhD thesis, California Institute of Technology
- Fumagalli G., Romero-Shaw I., Gerosa D., De Renzis V., Kritos K., Olejak A., 2024, arXiv e-prints, p. arXiv:2405.14945
- Gaia Collaboration et al., 2016, *A&A*, **595**, A1
- Gaia Collaboration et al., 2023, *A&A*, **674**, A1
- Gaia Collaboration et al., 2024, arXiv e-prints, p. arXiv:2404.10486
- Gair J. R., et al., 2023, *AJ*, **166**, 22
- Gayathri V., Yang Y., Tagawa H., Haiman Z., Bartos I., 2021, arXiv e-prints, p. arXiv:2104.10253
- Gayathri V., Wysocki D., Yang Y., Shaughnessy R. O., Haiman Z., Tagawa H., Bartos I., 2023, arXiv e-prints, p. arXiv:2301.04187
- Gerosa D., Berti E., 2017, *Physical Reviews D*, **95**, 124046
- Gerosa D., Berti E., 2019, *Physical Review D*, **100**, 041301
- Gerosa D., Fishbach M., 2021, *Nature Astronomy*, **5**, 749
- Ghez A. M., et al., 2008, *ApJ*, **689**, 1044
- Goldreich P., Tremaine S., 1979, *ApJ*, **233**, 857
- Gondán L., Kocsis B., 2021, arXiv e-prints, p. arXiv:2110.09540
- Graham M. J., et al., 2019, *PASP*, **131**, 078001
- Graham M. J., et al., 2020, *Phys. Rev. Lett.*, **124**, 251102
- Graham M. J., et al., 2023, *ApJ*, **942**, 99
- Gratton R., Bragaglia A., Carretta E., D’Orazi V., Lucatello S., Sollima A., 2019, *A&A Rev.*, **27**, 8

- Grishin E., Gilbaum S., Stone N. C., 2024, *MNRAS*, **530**, 2114
- Hall E. D., Evans M., 2019, *Classical and Quantum Gravity*, **36**, 225002
- Harris C. R., et al., 2020, *Nature*, **585**, 357
- Heger A., Woosley S. E., 2002, *ApJ*, **567**, 532
- Heger A., Fryer C. L., Woosley S. E., Langer N., Hartmann D. H., 2003, *ApJ*, **591**, 288
- Heggie D. C., 1973, PhD thesis, University of Cambridge, UK
- Hills J. G., Fullerton L. W., 1980, *AJ*, **85**, 1281
- Hopkins P. F., Richards G. T., Hernquist L., 2007, *ApJ*, **654**, 731
- Hunter J. D., 2007, *Computing in Science and Engineering*, **9**, 90
- Husa S., Khan S., Hannam M., Pürrer M., Ohme F., Forteza X. J., Bohé A., 2016, *Physical Reviews D*, **93**, 044006
- Ianova N., Justham S., Ricker P., 2020, Common Envelope Evolution, doi:10.1088/2514-3433/abb6f0.
- Ivezić Ž., et al., 2019, *ApJ*, **873**, 111
- Jiménez M. A., Masset F. S., 2017, *MNRAS*, **471**, 4917
- Kagra Collaboration et al., 2019, *Nature Astronomy*, **3**, 35
- Karathanasis C., Mukherjee S., Mastrogiovanni S., 2022, arXiv e-prints, p. arXiv:2204.13495
- Kerr R. P., 1963, *Phys. Rev. Lett.*, **11**, 237
- Khan S., Husa S., Hannam M., Ohme F., Pürrer M., Forteza X. J., Bohé A., 2016, *Physical Reviews D*, **93**, 044007
- Kocsis B., 2013, *ApJ*, **763**, 122
- Kollmeier J., et al., 2019, in Bulletin of the American Astronomical Society. p. 274
- Krinos K., Berti E., Silk J., 2022, arXiv e-prints, p. arXiv:2212.06845
- Kulkarni G., Worseck G., Hennawi J. F., 2019, *MNRAS*, **488**, 1035
- LIGO Scientific Collaboration et al., 2015, *Classical and Quantum Gravity*, **32**, 074001
- Lada C. J., Lada E. A., 2003, *ARA&A*, **41**, 57
- Lamontagne R., Demers S., Wesemael F., Fontaine G., Irwin M. J., 2000, *AJ*, **119**, 241
- Lang D., 2014, *AJ*, **147**, 108
- Li G.-P., 2022, arXiv e-prints, p. arXiv:2202.09961
- Li R., Lai D., 2022, *MNRAS*, **517**, 1602
- Li R., Lai D., 2023a, arXiv e-prints, p. arXiv:2303.12207
- Li R., Lai D., 2023b, *MNRAS*, **522**, 1881
- Li G.-P., Lin D.-B., Yuan Y., 2022, arXiv e-prints, p. arXiv:2211.11150

- Liu H.-Y., Liu W.-J., Dong X.-B., Zhou H., Wang T., Lu H., Yuan W., 2019, [ApJS, 243, 21](#)
- Loeb A., 2016, [ApJ, 819, L21](#)
- Lyke B. W., et al., 2020, [ApJS, 250, 8](#)
- Lyra W., Paardekooper S.-J., Mac Low M.-M., 2010, [ApJ, 715, L68](#)
- Maggiore M., et al., 2020, [Journal of Cosmology and Astroparticle Physics, 2020, 050](#)
- Mahapatra P., Gupta A., Favata M., Arun K. G., Sathyaprakash B. S., 2022, [arXiv e-prints, p. arXiv:2209.05766](#)
- Mahapatra P., Chattopadhyay D., Gupta A., Favata M., Sathyaprakash B. S., Arun K. G., 2024, in 42nd meeting of the Astronomical Society of India (ASI). p. O42
- Mandel I., de Mink S. E., 2016, [MNRAS, 458, 2634](#)
- Mangiagli A., et al., 2020, [Physical Reviews D, 102, 084056](#)
- Mapelli M., 2021, in , Handbook of Gravitational Wave Astronomy. p. 16, [doi:10.1007/978-981-15-4702-7\\_16-1](#)
- Mapelli M., Santoliquido F., Bouffanais Y., Arca Sedda M. A., Artale M. C., Ballone A., 2021, [Symmetry, 13, 1678](#)
- Marchant P., Langer N., Podsiadlowski P., Tauris T. M., Moriya T. J., 2016, [A&A, 588, A50](#)
- Masci F. J., Cutri R. M., Francis P. J., Nelson B. O., Huchra J. P., Heath Jones D., Colless M., Saunders W., 2010, [PASA, 27, 302](#)
- Masci F. J., et al., 2023, [arXiv e-prints, p. arXiv:2305.16279](#)
- Mauch T., Sadler E. M., 2007, VizieR Online Data Catalog, [p. J/MNRAS/375/931](#)
- McKernan B., Ford K. E. S., Lyra W., Perets H. B., Winter L. M., Yaqoob T., 2011, [MNRAS, 417, L103](#)
- McKernan B., Ford K. E. S., Lyra W., Perets H. B., 2012, [MNRAS, 425, 460](#)
- McKernan B., Ford K. E. S., Bellovary J., Leigh N., Metzger B., Haiman Z., O'Dowd M., Mac Low M., 2018, in American Astronomical Society Meeting Abstracts #231. p. 325.05
- McKernan B., et al., 2019, [ApJ, 884, L50](#)
- McKernan B., Ford K. E. S., O'Shaughnessy R., Wysocki D., 2020, [MNRAS, 494, 1203](#)
- McKernan B., Ford K. E. S., Callister T., Farr W. M., O'Shaughnessy R., Smith R., Thrane E., Vajpeyi A., 2022a, [MNRAS, 514, 3886](#)
- McKernan B., Ford K. E. S., Cantiello M., Graham M., Jermyn A. S., Leigh N. W. C., Ryu T., Stern D., 2022b, [MNRAS, 514, 4102](#)
- Meisner A. M., Lang D., Schlafly E. F., Schlegel D. J., 2019, [PASP, 131, 124504](#)

- Merloni A., et al., 2014, [MNRAS](#), **437**, 3550
- Monaghan J. J., 1976, [MNRAS](#), **177**, 583
- Monroe T. R., Prochaska J. X., Tejos N., Worseck G., Hennawi J. F., Schmidt T., Tumlinson J., Shen Y., 2016, [AJ](#), **152**, 25
- Nasim S. S., et al., 2023, [MNRAS](#), **522**, 5393
- Neumayer N., Seth A., Böker T., 2020, [A&A Rev.](#), **28**, 4
- Newman E. T., Couch E., Chinnapared K., Exton A., Prakash A., Torrence R., 1965, [Journal of Mathematical Physics](#), **6**, 918
- Newton I., 1687, [Philosophiae Naturalis Principia Mathematica.](#), doi:[10.3931/e-rara-440](#).
- Ostriker J. P., 1983, [ApJ](#), **273**, 99
- Ostriker E. C., 1999, [ApJ](#), **513**, 252
- Paardekooper S. J., Mellema G., 2006, [A&A](#), **459**, L17
- Paardekooper S. J., Baruteau C., Crida A., Kley W., 2010, [MNRAS](#), **401**, 1950
- Paczynski B., 1986, [ApJ](#), **304**, 1
- Paczynski B., 1996, [ARA&A](#), **34**, 419
- Palenzuela C., Lehner L., Yoshida S., 2010, [Physical Reviews D](#), **81**, 084007
- Paturel G., Petit C., Prugniel P., Theureau G., Rousseau J., Brouty M., Dubois P., Cambrésy L., 2003, [A&A](#), **412**, 45
- Peng P., Chen X., 2021, [MNRAS](#), **505**, 1324
- Penrose R., 1965, [Phys. Rev. Lett.](#), **14**, 57
- Peters P. C., 1964, [Physical Review](#), **136**, 1224
- Petrov P., et al., 2022, [ApJ](#), **924**, 54
- Pieroni M., Ricciardone A., Barausse E., 2022, [Scientific Reports](#), **12**, 17940
- Planck Collaboration et al., 2016, [A&A](#), **594**, A13
- Planck Collaboration et al., 2020, [A&A](#), **641**, A6
- Portegies Zwart S. F., McMillan S. L. W., Gieles M., 2010, [ARA&A](#), **48**, 431
- Pratten G., et al., 2021, [Physical Reviews D](#), **103**, 104056
- Qian K., Li J., Lai D., 2024, [ApJ](#), **962**, 143
- Qin Y., et al., 2022, [ApJ](#), **941**, 179
- Reitze D., et al., 2019, in [Bulletin of the American Astronomical Society](#). p. 35 ([arXiv:1907.04833](#)), doi:[10.48550/arXiv.1907.04833](#)
- Richards G. T., et al., 2002, [AJ](#), **123**, 2945
- Richards G. T., et al., 2006, [ApJS](#), **166**, 470
- Rizzuto F. P., Naab T., Spurzem R., Arca-Sedda M., Giersz M., Ostriker J. P., Banerjee S., 2021, arXiv e-prints, p. [arXiv:2108.11457](#)
- Robinson I., Schild A., Schucking E., 1965, [Quasi - Stellar Sources and Gravitational Collapse. Including the Proceedings of the 1st Texas Symposium](#)

- on Relativistic Astrophysics. Dallas. 16-18 December, 1963. Chicago, <https://books.google.nl/books?id=CMyWXwAACAAJ>
- Rodriguez C. L., Loeb A., 2018, *ApJ*, **866**, L5
- Rodríguez-Ramírez J. C., Bom C. R., Fraga B., Nemmen R., 2024, *MNRAS*, **527**, 6076
- Rodriguez C. L., Chatterjee S., Rasio F. A., 2016, *Physical Reviews D*, **93**, 084029
- Rodriguez C. L., Kremer K., Chatterjee S., Fragione G., Loeb A., Rasio F. A., Weatherford N. C., Ye C. S., 2021, *Research Notes of the American Astronomical Society*, **5**, 19
- Romero-Shaw I., Lasky P. D., Thrane E., 2021, *ApJ*, **921**, L31
- Romero-Shaw I., Lasky P. D., Thrane E., 2022, *ApJ*, **940**, 171
- Rowan C., Boekholt T., Kocsis B., Haiman Z., 2023, *MNRAS*, **524**, 2770
- Rowan C., Whitehead H., Boekholt T., Kocsis B., Haiman Z., 2024, *MNRAS*, **527**, 10448
- Runnoe J. C., Brotherton M. S., Shang Z., 2012, *MNRAS*, **422**, 478
- Samsing J., 2018, *Physical Review D*, **97**, 103014
- Samsing J., et al., 2020, arXiv e-prints, p. arXiv:2010.09765
- Samsing J., et al., 2022, *Nature*, **603**, 237
- Santini A., Gerosa D., Cotesta R., Berti E., 2023, *Physical Review D*, **108**, 083033
- Schellart P., 2013, K3Match: Point matching in 3D space (ascl:1307.003)
- Schlafly E. F., Meisner A. M., Green G. M., 2019, *ApJS*, **240**, 30
- Schödel R., et al., 2002, *Nature*, **419**, 694
- Schutz B. F., 1986, *Nature*, **323**, 310
- Schwarzschild K., 1916, *Sitzungsberichte der Königlich Preussischen Akademie der Wissenschaften*, pp 189–196
- Secunda A., Bellovary J., Mac Low M.-M., Ford K. E. S., McKernan B., Leigh N. W. C., Lyra W., Sándor Z., 2019, *ApJ*, **878**, 85
- Shipman H. L., 1975, *Astrophysical Letters*, **16**, 9
- Singer L. P., Price L. R., 2016, *Physical Reviews D*, **93**, 024013
- Somiya K., 2012, *Classical and Quantum Gravity*, **29**, 124007
- Spera M., Mapelli M., Giacobbo N., Trani A. A., Bressan A., Costa G., 2019, *MNRAS*, **485**, 889
- Stern D., et al., 2012, *ApJ*, **753**, 30
- Stevenson S., Clarke T. A., 2022, *MNRAS*, **517**, 4034
- Stone N., 2017, in APS April Meeting Abstracts. p. S14.002
- Stone N. C., Leigh N. W. C., 2019, *Nature*, **576**, 406
- Stone N. C., Metzger B. D., Haiman Z., 2017, *MNRAS*, **464**, 946

- Storey-Fisher K., Hogg D. W., Rix H.-W., Eilers A.-C., Fabbian G., Blanton M. R., Alonso D., 2024, [ApJ](#), **964**, 69
- Strauss M. A., et al., 2002, [AJ](#), **124**, 1810
- Syer D., Clarke C. J., Rees M. J., 1991, [MNRAS](#), **250**, 505
- Tagawa H., Haiman Z., Kocsis B., 2020, [ApJ](#), **898**, 25
- Tagawa H., Haiman Z., Bartos I., Kocsis B., Omukai K., 2021, [MNRAS](#), **507**, 3362
- Tagawa H., Kimura S. S., Haiman Z., Perna R., Tanaka H., Bartos I., 2022, [ApJ](#), **927**, 41
- Tagawa H., Kimura S. S., Haiman Z., Perna R., Bartos I., 2023, [ApJ](#), **950**, 13
- Tagawa H., Kimura S. S., Haiman Z., Perna R., Bartos I., 2024, [ApJ](#), **966**, 21
- Tanikawa A., Susa H., Yoshida T., Trani A. A., Kinugawa T., 2021, [ApJ](#), **910**, 30
- Tesch F., Engels D., 2000, [MNRAS](#), **313**, 377
- The LIGO Scientific Collaboration et al., 2021, [arXiv e-prints](#), p. [arXiv:2111.03634](#)
- Trani A. A., Quaini S., Colpi M., 2024, [A&A](#), **683**, A135
- Ueda Y., Akiyama M., Hasinger G., Miyaji T., Watson M. G., 2014, [ApJ](#), **786**, 104
- Vajpeyi A., Thrane E., Smith R., McKernan B., Saavik Ford K. E., 2022, [ApJ](#), **931**, 82
- Veronesi N., Rossi E. M., van Velzen S., Buscicchio R., 2022, [MNRAS](#), **514**, 2092
- Veronesi N., Rossi E. M., van Velzen S., 2023, [MNRAS](#), **526**, 6031
- Veronesi N., van Velzen S., Rossi E. M., 2024, [arXiv e-prints](#), p. [arXiv:2405.05318](#)
- Virtanen P., et al., 2020, [Nature Methods](#), **17**, 261
- Vitale S., Evans M., 2017, [Physical Reviews D](#), **95**, 064052
- Wang J.-M., Liu J.-R., Ho L. C., Li Y.-R., Du P., 2021a, [arXiv e-prints](#), p. [arXiv:2106.07334](#)
- Wang Y.-Z., Fan Y.-Z., Tang S.-P., Qin Y., Wei D.-M., 2021b, [arXiv e-prints](#), p. [arXiv:2110.10838](#)
- Wang J.-M., Liu J.-R., Ho L. C., Li Y.-R., Du P., 2021c, [ApJ](#), **916**, L17
- Wang Y., McKernan B., Ford K. E. S., Perna R., Leigh N., Mac Low M.-M., 2022, in AAS/Division of Dynamical Astronomy Meeting. p. 300.01
- Wei J. Y., Xu D. W., Dong X. Y., Hu J. Y., 1999, [A&AS](#), **139**, 575
- Woosley S. E., 2019, [ApJ](#), **878**, 49
- Woosley S. E., Heger A., 2021, [ApJ](#), **912**, L31
- Wright E. L., et al., 2010, [AJ](#), **140**, 1868

- Wu Q., Shen Y., 2022, [ApJS](#), **263**, 42
- Yang Y., et al., 2019, [Phys. Rev. Lett.](#), **123**, 181101
- Yang Y., Bartos I., Haiman Z., Kocsis B., Márka S., Tagawa H., 2020, [ApJ](#), **896**, 138
- York D. G., et al., 2000, [AJ](#), **120**, 1579
- Zevin M., Bavera S. S., 2022, [ApJ](#), **933**, 86
- Ziosi B. M., Mapelli M., Branchesi M., Tormen G., 2014, [MNRAS](#), **441**, 3703
- Zonca A., Singer L., Lenz D., Reinecke M., Rosset C., Hivon E., Gorski K., 2019, [Journal of Open Source Software](#), **4**, 1298
- de Mink S. E., Mandel I., 2016, [MNRAS](#), **460**, 3545
- van Velzen S., et al., 2024, [MNRAS](#), **529**, 2559



# NEDERLANDSE SAMENVATTING



## SUMMARY



# PUBLICATIONS



# CURRICULUM VITAE



## ACKNOWLEDGEMENTS

Another nice quote

– *Reference of the quote*, Author of the quote (year of the quote)